

Research paper

Spectral method for numerical solution of the electric field envelope propagation equation



Dušan Arsenović*, Jelena Dimitrijević, Branislav Jelenković

Institute of Physics, University of Belgrade, Pregrevica 118, Belgrade 11080, Serbia

ARTICLE INFO

Article history:

Received 21 May 2018

Revised 9 July 2018

Accepted 13 July 2018

Available online 17 July 2018

Keywords:

Numerical method

Maxwell–Bloch equations

Spectral method

ABSTRACT

We report new method for solving propagation equation for the electric field envelope, obtained from the Maxwell equations under the slowly varying envelope approximation and the paraxial approximation. This propagation equation usually represents part of Maxwell–Bloch system of equations. Method is semi-analytical and semi-numerical. We use analytical solution of the Fourier transform of the envelope equation, for a given initial condition, to find numerical solutions on grid nodes in 3+1 dimensions. We have tested our numerical results by comparing them with exact particular solutions of the envelope equation. We show that results of our method are in good agreement with the exact solutions for sufficient density of grid nodes. Solving the propagation equations by using this method is important for modelling many phenomena in areas of quantum and nonlinear optics dealing with the propagation of light through an active optical medium.

© 2018 Elsevier B.V. All rights reserved.

1. Introduction

The coherent field-matter interaction lies at the heart of many phenomena in quantum and nonlinear optics. Propagation of light through active optical medium is usually modelled with Maxwell–Bloch equations (MBE) [1–3], which have been proven adequate as a theoretical background for description of many phenomena regarding interaction between light and matter. MBE have been used to describe and simulate various effects like electromagnetically induced transparency [4,5], soliton propagation [6,7], self-induced transparency [8–10], propagation of rogue waves [11,12], photon-echo [13,14] etc.

The system of MBE represent system of partial differential equations. They are equations of semi-classical models of resonant interactions between light and an active optical medium consisting of discrete internal states, like atoms, quantum dots [15], impurity atoms or ions doped in host crystals [16], etc. With MBE one assumes that one or more electromagnetic (EM) fields are treated classically and quantum system with discrete internal states is treated quantum mechanically, by using the density matrix formalism. In this context, the evolution of EM field is given with the Maxwell equations, coupled to the set of optical Bloch equations (OBE) [17], via an expression for the macroscopic polarization, which mathematically represents non-homogenous part of EM field propagation equation and physically the source term of Maxwell equations.

There are variations of MBE in the literature like generalized MBE [18,19] or reduced MBE [11,20,21]. MBE are often solved for ultrashort pulses (shorter than 1ps) [22–28], by using spectral [24] and pseudo-spectral [22,25] methods. Other techniques to solve MBE, for ultrafast dynamics of electric field, have been proposed with the help of various finite difference schemes [26,27], where Yee scheme [29] or its modifications are often cited in literature.

* Corresponding author.

E-mail address: arsenovic@ipb.ac.rs (D. Arsenović).

For applications when the dynamics of electric field is slower, one can employ slowly varying envelope approximation (SVEA) [3]. MBE with SVEA are usually solved by approximating electric field with plane wave, which yields 1+1 D partial equations with first derivatives, over both time and propagation direction. If transverse effects cannot be neglected, one has to solve 3+1 D MBE, where “3” refers to three spatial dimensions, two transverse x and y and longitudinal, along the propagation z direction, and “1” refers to time t . This set of equations is significantly different by the form and therefore difficulty to solve than 1+1 D case, due to second derivatives over transverse coordinates, in the EM field propagation equation. To our knowledge, there are only few proposals for solving 3+1 D MBE with the SVEA applied. Hang and Huang [30] recently employed the method of multiple scales [31] to analyse the propagation of Airy wave packet in a resonant Λ -type three-level atomic gas.

In this work, we present novel method for solving 3+1 D electric field envelope scalar propagation equation obtained from the Maxwell equations under the paraxial and the slowly varying envelope approximations [3]. In the following text, we will refer to this equation as envelope equation. The method can easily be implemented for solution of decoupled MBE [32]. Since OBE represents system of ordinary partial equations, the solution of which can be obtained by standard methods, we assume that right-hand-side (RHS) of the envelope equation is known function and do not deal further with solutions of OBE. Our semi analytical and semi-numerical method takes double Fourier transform (FT) of the envelope equation over transverse coordinates and we obtain analytical solutions of envelope equation in the frequency domain for two initial conditions, for $t = t_0$ or $z = z_0$. By implementing analytical solutions and discrete FT, we applied the method to discrete points separated by increments of time and space, or to nodes of grids. Finally, we compared results of this method with the exact particular solutions of the envelope equation for two examples, and discuss differences when we vary values of density for nodes on grids.

2. Spectral method for solving envelope equation

With transverse component of the electric field in the form:

$$E(t, \vec{r}) = \mathcal{E}(t, \vec{r})e^{i\omega(t-z/c)} + c.c., \quad (1)$$

the envelope equation obtained by using the Maxwell equations, under the slowly varying envelope approximation and the paraxial approximation is:

$$\frac{ic}{2\omega} \nabla_{\perp}^2 \mathcal{E}(t, \vec{r}) + \frac{\partial \mathcal{E}(t, \vec{r})}{\partial z} + \frac{1}{c} \frac{\partial \mathcal{E}(t, \vec{r})}{\partial t} = R(t, \vec{r}), \quad (2)$$

where $\mathcal{E}(t, \vec{r})$ is the scalar electric field envelope, $R(t, \vec{r})$ is the source term of the envelope equation, ω is the electric field angular frequency and c is the speed of light. Here we assumed absence of free electric charges, free electric currents and magnetization, and the mean magnetic field has been eliminated. By using:

$$\nabla_{\perp}^2 = \frac{\partial^2}{\partial x^2} + \frac{\partial^2}{\partial y^2}, \quad (3)$$

Eq. (2) can be explicitly written as:

$$\frac{\partial \mathcal{E}(t, x, y, z)}{\partial z} + c_t \frac{\partial \mathcal{E}(t, x, y, z)}{\partial t} + c_x \frac{\partial^2 \mathcal{E}(t, x, y, z)}{\partial x^2} + c_y \frac{\partial^2 \mathcal{E}(t, x, y, z)}{\partial y^2} = R(t, x, y, z), \quad (4)$$

where $c_t = \frac{1}{c}$ and $c_x = c_y = \frac{ic}{2\omega}$.

Eq. (4) presents second order non-homogeneous partial differential equation with 4 independent variables. With given $R(t, x, y, z)$ and two initial conditions (given functions depending on 3 variables $\mathcal{E}(t, x, y, z_0)$ with $z = z_0$ fixed and $\mathcal{E}(t_0, x, y, z)$ with $t = t_0$ fixed), we solve Eq. (4) at the finite space domain $[x_{min}, x_{max}] \times [y_{min}, y_{max}] \times [z_0, z_{max}]$ and the time interval $[t_0, t_{max}]$, and obtain solution on $N_x \times N_y \times N_z \times N_t$ grid nodes, where each node is defined by its x, y, z , and t values.

2.1. Analytical solution of the envelope equation in the frequency domain

We next show that Eq. (4) can be solved analytically in the frequency domain. We used the following definition and notation for the double FT of the $\mathcal{E}(t, x, y, z)$, over transverse coordinates x and y :

$$\tilde{\mathcal{E}}_{xy}(t, k_x, k_y, z) \equiv \mathcal{F}[\mathcal{E}(t, x, y, z)](t, k_x, k_y, z) = \frac{1}{2\pi} \int_{-\infty}^{+\infty} dx \int_{-\infty}^{+\infty} dy \mathcal{E}(t, x, y, z) e^{i(k_x x + k_y y)} \quad (5)$$

and for double FT of $R(t, x, y, z)$, which we note as $\tilde{R}_{xy}(t, k_x, k_y, z)$. FT of the second derivative over x - (and analogously over y -) coordinate in Eq. (4) is in the form:

$$\mathcal{F}\left[\frac{\partial^2 \mathcal{E}(t, x, y, z)}{\partial x^2}\right] = -k_x^2 \tilde{\mathcal{E}}_{xy}(t, k_x, k_y, z). \quad (6)$$

By using Eqs. (5) and (6), we obtain equation for double FT of Eq. (4), over two coordinates x and y , as:

$$\frac{\partial \tilde{\mathcal{E}}_{xy}(t, k_x, k_y, z)}{\partial z} + \frac{1}{c} \frac{\partial \tilde{\mathcal{E}}_{xy}(t, k_x, k_y, z)}{\partial t} - f(k_x, k_y) \tilde{\mathcal{E}}_{xy}(t, k_x, k_y, z) = \tilde{R}_{xy}(t, k_x, k_y, z), \quad (7)$$

where $f(k_x, k_y) = (c_x k_x^2 + c_y k_y^2)$.

Eq. (7) can be solved analytically with given either one of the two initial conditions, $\mathcal{E}(t, x, y, z_0)$ or $\mathcal{E}(t_0, x, y, z)$. With given initial condition for $z = z_0$, $\mathcal{E}(t, x, y, z_0)$, the solution of Eq. (7) stands:

$$\begin{aligned} \tilde{\mathcal{E}}_{xy}(t, k_x, k_y, z) &= e^{-f(k_x, k_y)(z-z_0)} \tilde{\mathcal{E}}_{xy}(t - c_t(z - z_0), k_x, k_y, z_0) \\ &+ \int_{t-c_t(z-z_0)}^t \frac{1}{c_t} e^{\frac{f(k_x, k_y)(t'-t)}{c_t}} \tilde{R}_{xy}\left(t', k_x, k_y, \frac{-t + c_t z + t'}{c_t}\right) dt'. \end{aligned} \quad (8)$$

For given initial condition for $t = t_0$, $\mathcal{E}(t_0, x, y, z)$, the solution of Eq. (7) is:

$$\begin{aligned} \tilde{\mathcal{E}}_{xy}(t, k_x, k_y, z) &= e^{\frac{f(k_x, k_y)(t_0-t)}{c_t}} \tilde{\mathcal{E}}_{xy}\left(t_0, k_x, k_y, \frac{-t + t_0 + c_t z}{c_t}\right) \\ &+ \int_{t_0}^t \frac{1}{c_t} e^{\frac{f(k_x, k_y)(t'-t)}{c_t}} \tilde{R}_{xy}\left(t', k_x, k_y, \frac{-t + c_t z + t'}{c_t}\right) dt'. \end{aligned} \quad (9)$$

In Eqs. (8) and (9), first terms correspond to the solution of the homogenous Eq. (7), while second terms are particular solutions, for the corresponding initial conditions. Both Eqs. (8) and (9) can be used to solve Eq. (7) and consequently Eq. (4), by finding FT of the solution of Eq. (7), as long as t - and z -arguments obey $t \geq t_0$ and $z \geq z_0$. Eq. (8) is applicable when the condition:

$$t - c_t(z - z_0) \geq t_0 \quad (10)$$

is satisfied, while Eq. (9) requires the condition:

$$\frac{-t + t_0 + c_t z}{c_t} \geq z_0 \quad (11)$$

to be fulfilled.

Usually solutions to physical problems modelled with MBE require both initial conditions, and our method is suitable for solving these problems. In the following, we start with initial condition for $t = t_0$. Evolution over time is performed by using Eq. (9) and we implement initial condition for $z = z_0$ at each time-step. This ensures applications to realistic physical problems when EM fields (with given initial conditions $t = t_0$ and $z = z_0$) propagate through media, with response from media at each time-step, as given with solutions of decoupled MBE [32]. Eq. (8), where one would use evolution of electric field envelope over the propagation distance, can also be used for solving Eq. (7), but we here use Eq. (9).

2.2. Implementing the spectral method on grid nodes

We next explain how Eq. (9) is implemented at nodes of a grid. The solution given with Eq. (9) is applied at successive moments separated with the time interval Δt which we choose as:

$$\Delta t = c_t \Delta z = \frac{\Delta z}{c}. \quad (12)$$

By choosing this time-step, calculated values of the electric field envelope at the previous moment $\mathcal{E}(t - \Delta t, x, y, z - c\Delta t)$ are at grid nodes, time interval between them being Δt . Also, with this time-step, we don't have constraint on using Eq. (9). By setting $t = t_0 + \Delta t$ and $z = z_0 + n_z \Delta z$, $n_z = 0, 1, \dots, N_z - 1$, constraint given by Eq. (11) indicates that Eq. (9) can be applied at all z -steps besides $n_z = 0$, when we use initial condition for $z = z_0$.

Eq. (9) is calculated at nodes by setting $t_0 = t_n$ and $t = t_{n+1} = t_n + c_t \Delta z$, and by making substitution in the integral (see Eq. (9)) such that $t' = t_n + \tau c_t \Delta z$, which changes integration limits to $0 \leq \tau \leq 1$. Solution as given in (9) can then be written as:

$$\tilde{\mathcal{E}}_{xy}(t_{n+1}, k_x, k_y, z) = e^{-f(k_x, k_y)\Delta z} \left(\tilde{\mathcal{E}}_{xy}(t_n, k_x, k_y, z - \Delta z) + \Delta z I_R \right), \quad (13)$$

where I_R stands for:

$$I_R = \int_0^1 e^{f(k_x, k_y)\tau \Delta z} \tilde{R}_{xy}(t_n + \tau c_t \Delta z, k_x, k_y, z + (\tau - 1)\Delta z) d\tau. \quad (14)$$

The first term in parentheses in Eq. (13) is the numerical solution of Eq. (9) from the previous moment t_n . Since values of the integrand function in Eq. (14) are known only on grid nodes, that is for $\tau \in \mathbb{Z}$, we approximate $\tilde{R}_{xy}(t_n, k_x, k_y, z + (\tau - 1)\Delta z)$ with the linear function through two points, for values $\tau = 0$ and $\tau = 1$:

$$\begin{aligned} \tilde{R}_{xy}(t_n + \tau c_t \Delta z, k_x, k_y, z + (\tau - 1)\Delta z) &\approx \\ \tau [\tilde{R}_{xy}(t_n + c_t \Delta z, k_x, k_y, z) - \tilde{R}_{xy}(t_n, k_x, k_y, z - \Delta z)] &+ \tilde{R}_{xy}(t_n, k_x, k_y, z - \Delta z). \end{aligned} \quad (15)$$

If steps given in Eq. (12) are small enough, it is justifiable to assume that $\tilde{R}_{xy}(t_n + \tau c_t \Delta z, k_x, k_y, z + (\tau - 1)\Delta z)$ does not depend on time during Δt :

$$\tilde{R}_{xy}(t_n + \tau c_t \Delta z, k_x, k_y, z + (\tau - 1)\Delta z) \approx \tilde{R}_{xy}(t_n, k_x, k_y, z + (\tau - 1)\Delta z), \quad (16)$$

which yields to the following expression for Eq. (14):

$$I_R \approx \int_0^1 e^{f(k_x, k_y)\tau \Delta z} [\tau (\tilde{R}_{xy}(t_n, k_x, k_y, z) - \tilde{R}_{xy}(t_n, k_x, k_y, z - \Delta z)) + \tilde{R}_{xy}(t_n, k_x, k_y, z - \Delta z)] d\tau. \quad (17)$$

We calculate integral in Eq. (17) by using partial integration as:

$$\begin{aligned} I_R &\approx (\tilde{R}_{xy}(t_n, k_x, k_y, z) - \tilde{R}_{xy}(t_n, k_x, k_y, z - \Delta z)) \left[\frac{1}{f(k_x, k_y) \Delta z} e^{f(k_x, k_y) \Delta z} - \frac{1}{(f(k_x, k_y) \Delta z)^2} e^{f(k_x, k_y) \tau \Delta z} \right]_0^1 \\ &\quad + \tilde{R}_{xy}(t_n, k_x, k_y, z - \Delta z) \frac{1}{f(k_x, k_y) \Delta z} e^{f(k_x, k_y) \tau \Delta z} \Big|_0^1 \\ &= \frac{1}{(f(k_x, k_y) \Delta z)^2} \{ (\tilde{R}_{xy}(t_n, k_x, k_y, z) - \tilde{R}_{xy}(t_n, k_x, k_y, z - \Delta z)) [f(k_x, k_y) \Delta z e^{f(k_x, k_y) \Delta z} - e^{f(k_x, k_y) \Delta z} + 1] \\ &\quad + \tilde{R}_{xy}(t_n, k_x, k_y, z - \Delta z) f(k_x, k_y) \Delta z (e^{f(k_x, k_y) \Delta z} - 1) \}. \end{aligned} \quad (18)$$

Finally, the expression that we use to calculate I_R in Eq. (13) stands:

$$\begin{aligned} I_R &\approx \frac{1}{f^2(k_x, k_y) \Delta z^2} \left[(1 + e^{f(k_x, k_y) \Delta z} (f(k_x, k_y) \Delta z - 1)) \tilde{R}_{xy}(t_n, k_x, k_y, z) \right. \\ &\quad \left. + (e^{f(k_x, k_y) \Delta z} - f(k_x, k_y) \Delta z - 1) \tilde{R}_{xy}(t_n, k_x, k_y, z - \Delta z) \right], \end{aligned} \quad (19)$$

while for $f(k_x, k_y) = 0$ we use the trapezoidal rule:

$$\begin{aligned} I_R &\approx \int_0^1 \tilde{R}_{xy}(t_n, k_x, k_y, z + (\tau - 1) \Delta z) d\tau \\ &\approx \frac{1}{2} (\tilde{R}_{xy}(t_n, k_x, k_y, z) + \tilde{R}_{xy}(t_n, k_x, k_y, z - \Delta z)). \end{aligned} \quad (20)$$

In short, procedure described above gives formula that we use to propagate numerical solution of the electric field envelope $\mathcal{E}^N(t_{n+1}, x, y, z)$ in the frequency domain, from t_n to t_{n+1} , as:

$$\tilde{\mathcal{E}}_{xy}^N(t_{n+1}, k_x, k_y, z) = e^{-f(k_x, k_y) \Delta z} \left(\tilde{\mathcal{E}}_{xy}^N(t_n, k_x, k_y, z - \Delta z) + \Delta z I_R \right), \quad (21)$$

where one has to use either Eq. (19) or Eq. (20) for calculating I_R , depending on the value of $f(k_x, k_y)$.

2.3. Numerical procedure

We give here brief summary of steps used in the calculations. Discrete FT at grid nodes in our method are achieved by using the fast-Fourier-transform algorithm according to Press [33]. The definition of FT and grid discretization, used for the results presented in the next Section, are given in Appendix A.

Each step of the procedure is performed for $\forall k_x, k_y$ as follows:

At the initial moment t_0 :

- For each z value on the grid calculate $\tilde{\mathcal{E}}_{xy}^N(t_0, k_x, k_y, z)$ (from the initial condition for $t = t_0$) and $\tilde{R}_{xy}(t_0, k_x, k_y, z)$.

Evolution of the envelope between t_n and $t_{n+1} = t_n + \Delta t$, $n = 0, 1, 2, \dots$ is then successively calculated through the following steps:

- For $z = z_0$ calculate $\tilde{\mathcal{E}}_{xy}^N(t_{n+1}, k_x, k_y, z_0)$ from the initial condition.
- For each z calculate $\tilde{R}_{xy}(t_n, k_x, k_y, z)$.
- For each $z > z_0$ obtain $\tilde{\mathcal{E}}_{xy}^N(t_{n+1}, k_x, k_y, z)$ from Eq. (21).

Inverse FT of $\tilde{\mathcal{E}}_{xy}^N(t_{n+1}, k_x, k_y, z)$ is calculated only for the times when we collect results for $\mathcal{E}^N(t_{n+1}, x, y, z)$, since Eq. (21) is calculated in the frequency domain.

3. Results and discussion

In this section we test validity of our method by comparing results of the method with the exact solutions of Eq. (2). We discuss behaviour of numerical errors for different grid densities and also behaviour of numerical solutions at the boundaries of the interaction region.

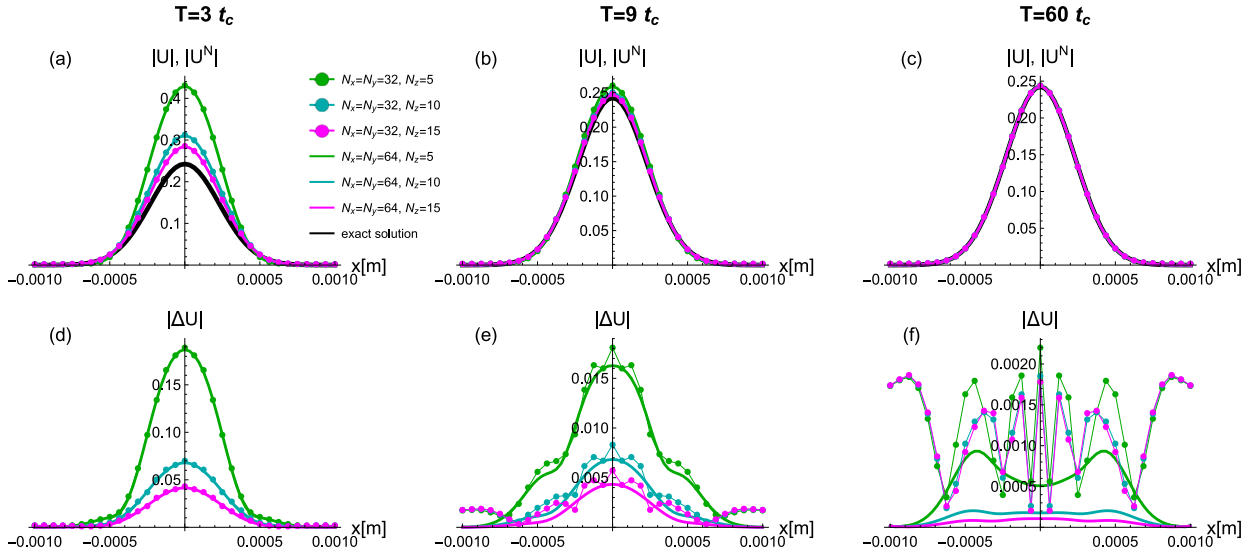


Fig. 1. (a)–(c): Dependence of absolute values of exact solution of Eq. (4) given with Eq. (22), $|U(t, x, y, z)|$, (black line), and of numerical solution $|U^N(t, x, y, z)|$ on the x -coordinate. (d)–(f): Dependence of absolute values of the difference between the exact solution and the numerical solution, $|\Delta U(t, x, y, z)| = |U(t, x, y, z) - U^N(t, x, y, z)|$, on the x -coordinate. Results are presented for three values of the period of oscillations, (a) and (d) $T = 3 t_c$, (b) and (e) $T = 9 t_c$ and (c) and (f) $T = 60 t_c$, where $t_c = z_{\max}/c$. Results in all figures are given for 6 values of grid densities, for $N_x = N_y = 32, 64$ and $N_z = 5, 10, 15$, as indicated in the legend. Initial coordinates are $t_0 = z_0 = 0$ and results are presented for the position $z = z_{\max} = 0.1$ m, $y = 0$ and for $t = 30 \cdot t_c = 1.00069 \cdot 10^{-8}$ s. Other parameters are $a = 3.10448 \cdot 10^{-9}$ m² and $\omega = 2\pi \cdot 384.23$ THz.

3.1. Example I

The first example is the following particular solution of the envelope equation:

$$U(t, x, y, z) = e^{i\Omega t} U_0(x, y, z), \quad (22)$$

where $U_0(x, y, z)$:

$$U_0(x, y, z) = \frac{a}{\sqrt{a - 2c_x z} \sqrt{a - 2c_y z}} e^{-\frac{x^2}{2(a - 2c_x z)}} e^{-\frac{y^2}{2(a - 2c_y z)}}. \quad (23)$$

Eq. (4) then has the form:

$$\frac{\partial U(t, x, y, z)}{\partial z} + c_t \frac{\partial U(t, x, y, z)}{\partial t} + c_x \frac{\partial^2 U(t, x, y, z)}{\partial x^2} + c_y \frac{\partial^2 U(t, x, y, z)}{\partial y^2} = i\Omega c_t U(t, x, y, z), \quad (24)$$

which shows that RHS is proportional to the unknown function $U(t, x, y, z)$ with complex constant $i\Omega c_t$. This example corresponds to the case when the polarization is proportional to the electric field, the case in the MBE with nonlinearities excluded. The evolution of $U(t, x, y, z)$ is given with the phase factor $e^{i\Omega t}$, where Ω represents angular frequency of evolution, with the period of oscillations $T = 2\pi/\Omega$.

Results in Fig. 1 show comparison of numerical solutions of Eq. (24) obtained by the method described in the previous section with the exact solution given with Eq. (22). The difference between the two results, or numerical errors are presented in the bottom row. Fig. 1(a)–(c) show dependence of absolute values of the exact solution $|U(t, x, y, z)|$ and of numerical solutions $|U^N(t, x, y, z)|$ on the x -coordinate. Fig. 1(d)–(f) show dependence of absolute values of the difference between the exact and the numerical solution, $|\Delta U(t, x, y, z)| = |U(t, x, y, z) - U^N(t, x, y, z)|$, on the x -coordinate. Results are presented for three values of the period of oscillations $T = 3 t_c$ (Fig. 1(a) and (d)), $T = 9 t_c$ (Fig. 1(b) and (e)) and $T = 60 t_c$ (Fig. 1(c) and (f)). These periods correspond to angular frequencies $\Omega = 6.279, 2.093$ and 0.314 GHz respectively. $t_c = z_{\max}/c$ stands for the time required for wave to pass the integration distance $z_{\max} = 0.1$ m. Initial coordinates are $t_0 = z_0 = 0$ and results are presented at $z = z_{\max}$, $y = 0$ and for $t = 30 \cdot t_c = 1.00069 \cdot 10^{-8}$ s. Values of other parameters are $a = 3.10448 \cdot 10^{-9}$ m² and $\omega = 2\pi \cdot 384.23$ THz, which is the Rb D2 line frequency. Results are given for 6 choices of grid densities, which is for two $N_x = N_y = 32, 64$, combined with three values $N_z = 5, 10, 15$, as indicated in the figure legend.

Fig. 1 demonstrates how sensitive the method is to different choices of N_x, N_y and N_z (and consequently N_t). We note that we intentionally made grid densities to be rather sparse, in order to demonstrate the source of numerical errors. Since T represents period of time-evolution of the function given with Eq. (22), three different values of the period T correspond to the “speed” of evolution. Results show that shorter period and therefore faster oscillations require smaller steps between nodes, while for the longest period ($T = 60 t_c$), even with the smallest density of nodes, we achieved very high precision, with relative error less than 1% in the central regions of x - and y - intervals. Results in Fig. 1(a) and (d), for the shortest

Table 1

Values for Δz and Δt for different N_z , used in calculations for results in Fig. 1. Last three column show ratios of different values of periods T ($3t_c$, $9t_c$ and $60t_c$), to different time-steps for the corresponding N_z .

N_z	$\Delta z[m]$	$\Delta t[ns]$	$\Delta t[t_c]$	$3t_c/\Delta t$	$9t_c/\Delta t$	$60t_c/\Delta t$
5	0.025	0.0834	0.25	12	36	240
10	0.0111	0.0371	0.1111	27	81	540
15	0.0071	0.0238	0.0714	42	126	840

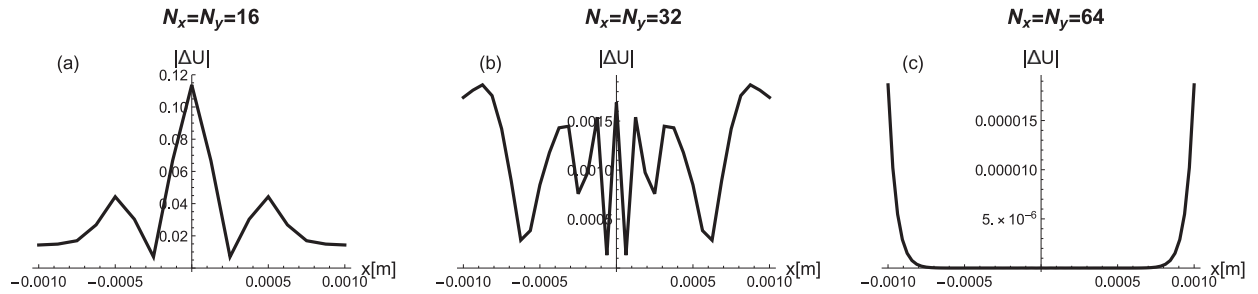


Fig. 2. Dependence of absolute values of the difference between the exact solution and the numerical solution, $|\Delta U(t, x, y, z)| = |U(t, x, y, z) - U^N(t, x, y, z)|$, on the x -coordinate, for the case when the exact solution is given in Eq. (23). We vary grid densities: $N_x = 16$ (a), $N_x = 32$ (b) and $N_x = 64$ (c). $N_z = 15$, while other parameters are the same as for results in Fig. 1.

period $T = 3t_c$, also indicate that increase of N_x and N_y from 32 to 64 does not further improve precision, since Δt and Δz are not sufficiently small.

In Table 1, we give ratios of different values of periods to different values of Δt (for corresponding N_z), used in calculations for results presented in Fig. 1. Values in the Table 1 reflect tendency of results in Fig. 1, that Δt have to be sufficiently small, $\Delta t \ll T$; in the case of fast oscillating functions with t , this steps have to be smaller, while for slowly varying functions the bigger steps are allowed. With Δt and Δz related by Eq. (12), we find the condition for the size of z -step as $\Delta z = \frac{\Delta t}{cT} \ll cT$.

3.2. Example II

In this example we use function $U_0(x, y, z)$, given in Eq. (23), which is the exact solution of Eq. (2), when $R(t, x, y, z)$ is zero. In this way we analyze effects of different node densities, N_x and N_y , for the case that is independent of t . In Fig. 2 we present dependence of absolute values of the differences between exact and numerical solutions, $|\Delta U(t, x, y, z)|$ on x -coordinate, for values of grid densities: $N_x = N_y = 16$ (a), $N_x = N_y = 32$ (a) and $N_x = N_y = 64$ (c). Results are for $N_z = 15$, while other parameters are the same as for results in Fig. 1. As Fig. 2 shows, absolute value of numerical error is reduced for about two-orders of magnitude when number of grid nodes, N_x and N_y , are doubled. With increasing N_x and N_y , differences between exact and numerical solutions become negligible except at edges of the interval.

In reality, domain over transverse coordinates is not finite i.e. light disperse. This lack of boundary conditions often presents problems in numerical methods. Due to the fact that we use discrete FT over x and y coordinate, the domain of integration is periodic in these two directions, meaning that effectively periodic boundary conditions are applied. The solution which physically would leave the domain, reenters the computational domain at the opposite side. This well-known numerical difficulty in numerical methods when using the discrete FT, known as wraparound effect, can be rectified by using method like perfectly matched layers [34]. Another possibility to escape wraparound effect is to zero-pad all around the boundaries, which can be realized by multiplying solutions obtained in the interaction region with super-Gaussian of higher order or with some other appropriate function.

4. Conclusions

We presented novel method for solving the electric field envelope propagation equation. The method is based upon using the analytical solution of the envelope equation in the frequency domain for the given initial time condition. Numerical procedure is developed to implement this solution on the equally spaced nodes of the numerical grid, where each node is defined by the set of four coordinates, x , y , z and t . Validity of the method is tested by comparing numerical solutions to the particular analytical solutions of the envelope equation for different values of grid densities. The tests were done for the exact solutions of the envelope equation with different time behaviour, therefore yielding importance of properly choosing time-step, and consequently the step over the propagation direction. As the second example, we compared our method with time-independent function, which enabled analysis of numerical errors at transverse boundaries of the interaction region due to applying discrete FT over the transverse coordinates. This method shows excellent agreement with exact solutions

of the envelope equation when grid density is properly chosen. Method presented here can be applied to simulate various phenomena of light-matter interactions when transverse effects of EM field are of interest. It can also be adjusted for the case of multiple fields components in the decoupled MBE or in the class of self-induced transparency equations, and as well be employed to solve simpler equations, which comprise distinct terms of the envelope equation, like the paraxial wave equation or paraxial Helmholtz equation, etc.

Acknowledgements

This work was supported by the Ministry of Education, Science and Technological Development of the Republic of Serbia, under grants III 45016 and OI 171038.

Appendix A. Spatial grid and two-dimensional Fourier transform

Integration intervals (over x and y coordinate) are first divided into N_x and N_y nodes. We further shift and normalize both intervals such that:

$$\begin{aligned} \Delta x = \Delta y = 1, \quad x_a = a\Delta x, \quad y_b = b\Delta y, \\ a = 0, 1, \dots, N_x - 1, \quad b = 0, 1, \dots, N_y - 1 \end{aligned} \quad (\text{A.1})$$

With this choice of x_a and y_b , we next choose k_{xi} and k_{yj} as:

$$k_{xi} = \frac{2\pi}{N_x\Delta x}i, \quad k_{yj} = \frac{2\pi}{N_y\Delta y}j, \quad (\text{A.2})$$

where indices i and j take values:

$$\begin{aligned} i = -\frac{N_x}{2}, -\frac{N_x}{2} + 1, \dots, 0, \dots, \frac{N_x}{2} - 2, \frac{N_x}{2} - 1, \\ j = -\frac{N_y}{2}, -\frac{N_y}{2} + 1, \dots, 0, \dots, \frac{N_y}{2} - 2, \frac{N_y}{2} - 1. \end{aligned} \quad (\text{A.3})$$

Here we have assumed that N_x and N_y are even numbers, that is integer powers of number 2 [33]. Next, set of k_x (and equivalently k_y) has to be rearranged such that zero k_{xi} corresponds to $i = 0$, positive k_{xi} correspond to values $1 \leq i \leq \frac{N_x}{2} - 1$, while negative k_{xi} correspond to $\frac{N_x}{2} + 1 \leq i \leq N - 1$. The value $i = -\frac{N_x}{2}$ can be associated with both $k_{x, N/2}$ and $k_{x, -N/2}$.

With this choice of k_x and k_y , we use following definition of two-dimensional discrete FT: Given a complex function $h(k_x, k_y)$ defined over the two-dimensional grid, its two-dimensional discrete Fourier transform as a complex function $H(n_x, n_y)$, is defined over the same grid as:

$$H(n_x, n_y) = \sum_{k_y=0}^{N_y-1} \sum_{k_x=0}^{N_x-1} e^{2\pi i \frac{k_y}{N_y} n_y} e^{2\pi i \frac{k_x}{N_x} n_x} h(k_x, k_y), \quad (\text{A.4})$$

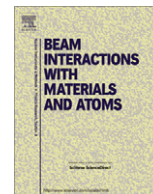
and accordingly inverse Fourier transform is given with:

$$h(k_x, k_y) = \frac{1}{N_x N_y} \sum_{k_y=0}^{N_y-1} \sum_{k_x=0}^{N_x-1} e^{-2\pi i \frac{k_y}{N_y} n_y} e^{-2\pi i \frac{k_x}{N_x} n_x} H(n_x, n_y). \quad (\text{A.5})$$

References

- [1] McNeil B. Due credit for Maxwell-Bloch equations. *Nat Photonics* 2015;9: 207–207.
- [2] Arecchi F, Bonifacio R. Theory of optical maser amplifiers. *IEEE J Quantum Electron* 1965;1:169–78.
- [3] Lugiato LA. Nonlinear optical systems. Cambridge, United Kingdom: Cambridge University Press; 2015.
- [4] Fleischhauer M, Imamoglu A, Marangos JP. Electromagnetically induced transparency: optics in coherent media. *Rev Mod Phys* 2005;77:633–73.
- [5] Kiffner M, Dey TN. Dynamical control of pulse propagation in electromagnetically induced transparency. *Phys Rev A* 2009;79:023829.
- [6] Chen Y, Bai Z, Huang G. Ultraslow optical solitons and their storage and retrieval in an ultracold ladder-type atomic system. *Phys Rev A* 2014;89:023835.
- [7] Hang C, Huang G. Stern-gerlach effect of weak-light ultraslow vector solitons. *Phys Rev A* 2012;86:043809.
- [8] McCall SL, Hahn EL. Self-induced transparency by pulsed coherent light. *Phys Rev Lett* 1967;18:908–11.
- [9] Bullough RK, Caudrey PJ, Eilbeck JC, Gibbon JD. A general theory of self-induced transparency. *Opto-electronics* 1974;6:121–40.
- [10] Slusher RE, Gibbs HM. Self-induced transparency in atomic rubidium. *Phys Rev A* 1972;5:1634–59.
- [11] Xu S, Porsezian K, He J, Cheng Y. Circularly polarized few-cycle optical rogue waves: rotating reduced Maxwell-Bloch equations. *Phys Rev E* 2013;88:062925.
- [12] Li C, He J, Porsezian K. Rogue waves of the Hirota and the Maxwell-Bloch equations. *Phys Rev E* 2013;87:012913.
- [13] Tsang L, Cornish CS, Babbitt WR. Analytic solutions of the Maxwell-Bloch equations for high photon-echo efficiency of multiple pulse sequences. *J Opt Soc Am B* 2003;20:379–90.
- [14] Blake A, Sukharev M. Photon echo in exciton-plasmon nanomaterials: a time-dependent signature of strong coupling. *J Chem Phys* 2017;146:084704.
- [15] Takeda H, John S. Self-consistent Maxwell-Bloch theory of quantum-dot-population switching in photonic crystals. *Phys Rev A* 2011;83:053811.
- [16] Xiong J, Colice M, Schlottau F, Wagner K, Fornberg B. Numerical solutions to 2d Maxwell-Bloch equations. *Opt Quant Electron* 2008;40:447–53.
- [17] Bloch F, Hansen WW, Packard M. The nuclear induction experiment. *Phys Rev* 1946;70:474–85.
- [18] Saksida P. On the generalized Maxwell-Bloch equations, symmetry, integrability and geometry. *Methods Appl* 2006;2:038.

- [19] Sczaniecki L. Effective Hamiltonians, two-level systems, and generalized Maxwell-Bloch equations. *Phys Rev A* 1983;28:3493–514.
- [20] Agrotis M, Ercolani N, Glasgow S, Moloney J. Complete integrability of the reduced Maxwell-Bloch equations with permanent dipole. *Physica D* 2000;138:134–62.
- [21] Steudel H, Zabolotskii AA. Solitons of the reduced Maxwell-Bloch equations for circularly polarized light. *J Phys A Math Gen* 2004;37:5047.
- [22] Marskar R, Österberg U. Multilevel Maxwell-Bloch simulations in inhomogeneously broadened media. *Opt Express* 2011;19:16784.
- [23] Niu Y, Xia K, Cui N, Gong S, Li R. Spatiotemporal evolution and multiple self-focusing of ultrashort pulses in a resonant two-level medium. *Phys Rev A* 2008;78:063835.
- [24] Saut O. Une méthode spectrale pour les équations de Maxwell-Bloch bidimensionnelles dans les cristaux nonlinéaires. *CR Math* 2005;340:927–32.
- [25] Bourgade A, Saut O. Numerical methods for the bidimensional Maxwell-Bloch equations in nonlinear crystals. *J Comput Phys* 2006;213:823–43.
- [26] Saut O. Computational modeling of ultrashort powerful laser pulses in a nonlinear crystal. *J Comput Phys* 2004;197:624–46.
- [27] Ziolkowski RW, Arnold JM, Gogny DM. Ultrafast pulse interactions with two-level atoms. *Phys Rev A* 1995;52:3082–94.
- [28] Van CL, Viet HN, Trippenbach M, Xuan KD. Propagation technique for ultrashort pulses II: numerical methods to solve the pulse propagation equation. *Comput Methods Sci Technol* 2008;14:13–19.
- [29] Yee K. Numerical solution of initial boundary value problems involving Maxwell's equations in isotropic media. *IEEE Trans Antennas Propag* 1966;14:302–7.
- [30] Hang C, Huang G. Slow-light airy wave packets and their active control via electromagnetically induced transparency. *Phys Rev A* 2013;88:013825.
- [31] Jeffrey A. Asymptotic methods in nonlinear wave theory. Boston: Pitman Advanced Pub. Program; 1982.
- [32] Bidégaray B. Time discretizations for Maxwell-Bloch equations. *Numer Methods Partial Differ Equ* 2003;19:284–300.
- [33] Press W. Numerical recipes in C: the art of scientific computing. Cambridge Cambridgeshire New York: Cambridge University Press; 1992.
- [34] Berenger. Perfectly matched layer (PML) for computational electromagnetics. San Rafael, Calif: Morgan & Claypool Publishers; 2007.



Perturbative solution for analysis of coherent processes in a double- Λ atomic scheme

Jelena Dimitrijević*, Dušan Arsenović, Branislav M. Jelenković

Institute of Physics, University of Belgrade, Pregrevica 118, 11080 Belgrade, Serbia

ARTICLE INFO

Article history:

Received 22 July 2011

Received in revised form 12 September 2011

Available online 23 November 2011

Keywords:

Interaction of light and matter

Electromagnetically induced transparency

ABSTRACT

We solve optical Bloch equations (OBEs) for the atomic scheme that consists of four atomic levels which constitute double-lambda (Λ) configuration i.e. two Λ systems sharing the same two ground levels. Λ atomic scheme has been used as a basis for many interesting applications in atomic physics and nonlinear optics. It was studied in the context of electromagnetically induced transparency (EIT) Shpalsman et al. (2005) [1], four-wave mixing Baolong et al. (1998) [2], lasers without inversion Kocharovskaya et al. (1990) [3], etc. More recently, efficient application of Λ scheme led to the development of phenomena like slow and stored light Eilam et al. (2008) [4], quantum mechanical entanglement of two beams of light Boyer et al. (2008) [5] and squeezed light Imad et al. (2011) [6].

Typically, a numerical solution of OBEs is used in the theoretical treatment of atomic system of two Λ schemes. In this work, interactions of four laser fields driving a Λ level scheme were analyzed by using perturbative method to solve OBEs Dimitrijević et al. (2011) [7]. Perturbative method produces simpler solutions such that analytical expressions can be obtained. The comparison of results obtained using lower-order corrections of perturbative method, and the exact calculations using optical Bloch equations is presented. Analytical expressions provide valuable information about processes that occur in the Λ atomic system. These informations cannot be deduced from the numerical solutions of the OBEs for the same atomic scheme.

© 2011 Elsevier B.V. All rights reserved.

1. Introduction

Interference of different excitation channels during atom–laser excitations allows development of variety of interesting phenomena. One can control and modify properties of coherently prepared media by using different excitation channels in atomic schemes. These include various multilevel atomic schemes like three-level V , Λ and ladder systems. Four-level atomic systems have recently attracted great attention. One of the most studied four-level atomic scheme is a Λ configuration. Of particular interest are Λ systems in which four atomic or molecular states are coupled with four near-resonant laser beams such that a closed loop is formed. It has been indicated already that Λ atomic systems have variety of interesting applications [1–6].

In this paper, we obtain analytical expressions for the density matrix elements by using the perturbative method [7] to solve OBEs written for a Λ system. This method was recently applied to a different atomic system, one which allows electromagnetically induced absorption [8] to be developed. The analytical expressions for the lower-order corrections are often a source of valuable

information about processes that occur in a Λ atomic scheme. Such additional knowledge cannot be deduced from the numerical solutions of the OBEs. We apply the perturbative method to the Λ atomic system when the conditions for observing electromagnetically induced transparency [9] are present. We investigate the role of narrow Lorentzian peak, found in the analytical expression of ground-state coherences, for the development of EIT. The method allows us to follow transfer of the narrow Lorentzian from the second correction to higher order corrections of different density matrix elements, optical coherences, populations.

2. Model for calculations of interaction of Λ with lasers

2.1. Optical Bloch equations

We calculate elements of density matrix ρ for the Λ interaction scheme i.e. four continuous-wave lasers coupling four atomic levels (see Fig. 1). We solve steady-state OBEs given by:

$$\frac{i}{\hbar} [\hat{H}_0, \hat{\rho}] + \frac{i}{\hbar} [\hat{H}_I, \hat{\rho}] + \hat{S}\hat{E} + \gamma\hat{\rho} = \gamma\hat{\rho}_0. \quad (1)$$

In Eq. (1) Hamiltonian \hat{H}_I describes the interaction of lasers with atoms in a Λ configuration, \hat{H}_0 represents the internal energy of Λ atomic levels, $\hat{S}\hat{E}$ is abbreviated spontaneous emission operator

* Corresponding author.

E-mail address: jelena.dimitrijevic@ipb.ac.rs (J. Dimitrijević).

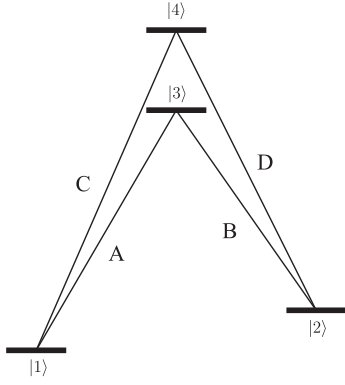


Fig. 1. Interaction scheme – DA configuration of levels that interacts with four laser light fields A, B, C and D.

with the rate Γ for both excited-state levels, 3 and 4. Term $\gamma\hat{\rho}$ describes the relaxation of all density matrix elements due to the finite time that atom needs to cross the laser beam, typically much shorter than the life time of investigated coherences. Term $\gamma\hat{\rho}_0$ describes the continuous flux of atoms to the laser beam, with equal population of two ground-state levels. The detailed system of OBEs for the 4-level atom is given in A.

The system of equations given by Eq. (1) introduces implicitly several new quantities that will be used in the following text. Rabi frequencies of lasers A, B, C and D in Fig. 1 are $\Omega_{A,B,C,D}$. Laser light detunings from the corresponding atomic frequencies are $\Delta_{A,B,C,D}$. Detuning between ground levels 1 and 2 is $\Delta_R \equiv \Delta_A - \Delta_B = \Delta_C - \Delta_D$, and between excited levels is $\Delta_E = \Delta_C - \Delta_A = \Delta_D - \Delta_B$. Relative phase between lasers is $\Phi = (\varphi_A - \varphi_B) - (\varphi_C - \varphi_D)$, where $\varphi_{A,B,C,D}$ are lasers phases.

2.2. Perturbative method

Here we describe perturbative method [7] used to solve OBEs for the four-level system. We start from OBEs in the matrix form, $Ax = y$, where x represents the column of density matrix elements $\{\rho_{11}, \rho_{12}, \dots, \rho_{44}\}$, A is the system's matrix and y is a non-homogeneous part. In order to apply perturbative method, elements of matrix A are separated into unperturbed and perturbed part, $A = A_0 + A_{\text{pert}}$. The elements of matrix A_{pert} are taken as perturbation and are much smaller than elements of A_0 . Unperturbed part and corrections of density matrix are solved in the iterative manner as:

$$\begin{aligned} x_0 &= -A_0^{-1}y, \\ x_{n+1} &= -A_0^{-1}A_{\text{pert}}x_n. \end{aligned} \quad (2)$$

Density matrix element obtained by perturbative method consist of unperturbed part x_0 , and series of successive corrections x_n , where n is the iteration number. As it turns out, a density-matrix element does not have to be corrected by every-order correction. Instead, depending on the choice of perturbation, only its certain-order corrections can be non-zero.

3. Results and discussion

3.1. Choice for perturbation

When elements of the matrix A_{pert} are much smaller than those of A_0 , the sum of corrections converge, after several iterations, to the exact solution. By the exact solution we mean the numerical solution of the system of equations, Eq. (1), written for the atomic system given in Fig. 1. There are also other limitations of the

perturbative method [7]. First, the system of equations (Eq. (1)) has to be non-homogenous. This is ensured for OBEs given by Eq. (1) because the relaxation with rate γ is included. Also, as seen from Eq. (2), the matrix A_0 has to be invertible. Therefore, not all choices of perturbation are possible.

We do not consider spontaneous emission as perturbation, because this would require that Rabi frequencies, as part of matrix A_0 , satisfy $\Omega_{A,B,C,D} \gg \Gamma$. For very strong laser light fields system of equations given by Eq. (1) needs to be modified to include other effects into OBEs. Relaxation with γ is also not possible as the perturbation, because γ ensures non-homogeneity of the system of equations. For the large enough Rabi frequencies $\Omega_{A,B,C,D} \gg \Delta_{A,B,C,D}$, the choice of taking detunings $\Delta_{A,B,C,D}$ as perturbation is possible.

Our analysis shows that interaction of DA with either one, two, three or four lasers is also possible choice for perturbation for the small enough magnitudes of Rabi frequencies $\Omega_{A,B,C,D}$. Besides numerical solution of Eq. (2), we also calculate analytical expressions of the lower-order corrections of density matrix elements. Considering the interaction of DA atomic scheme with all four lasers as perturbation yields the simplest analytical expressions for the lower-order corrections. If the interaction with a laser is not taken as perturbation, it is then a part of the unperturbed part, matrix A_0 . Perturbation method requires calculation of the inverse matrix of A_0 and increase of terms in A_0 leads to too complex expression for A_0^{-1} which is not favorable for analytical calculations.

3.2. Example for EIT

We present results of the perturbation method applied to the system of four lasers interacting with a four-level atom, considering all laser interactions as perturbations. We choose parameters so that EIT can be observed. Mathematically, this requires the condition $\hat{H}_I|DS\rangle = 0$ (where $|DS\rangle$ is a dark state), which in turn yields the specific relations to field phases, frequencies and amplitudes: $\Phi = 0, \Delta_R = 0, \Omega_B\Omega_C = \Omega_A\Omega_D$ [10].

Results are obtained for Rabi frequencies $\Omega_A = 0.001 \Gamma, \Omega_B = 0.0001 \Gamma, \Omega_C = 0.002 \Gamma$ and $\Omega_D = 0.0002 \Gamma$, detunings Δ_A, Δ_C are equal to zero. We vary $\Delta_R = -\Delta_B = -\Delta_D$ around zero. Phases of all four lasers are equal to zero $\varphi_{A,B,C,D} = 0$ and their relative phase too. We calculate steady-state OBEs by normalizing equations i.e. parameters to Γ , where we take $\Gamma = 1$, while for the relaxation rate we take $\gamma = 0.01 \Gamma$. With these parameters, we have that lasers A and C are strong (pump lasers), while B and D are probe lasers whose frequencies are varied around the corresponding atomic resonance. Solutions of perturbative method, with the choice of perturbation discussed here, are such that odd corrections contribute only to optical coherences, while even corrections affect other elements of density matrix.

Fig. 2 shows results for the corrections (a) and sums of low-order corrections (b) of the imaginary part of density matrix element ρ_{23} as a function of the detuning Δ_R . This quantity is proportional to the imaginary part of complex susceptibility i.e. the absorption coefficient of laser B. The absorption of other lasers i.e. optical coherences, which we do not present here, show similar dependencies on Δ_R . From Fig. 2 (b), where we also presented ρ_{23} obtained from the exact numerical solution of the OBEs, it is obvious that the sum of corrections (plus unperturbed part) converges after several iterations to the exact solution of OBEs and that the behavior of density-matrix element is dominantly determined by its first non-zero corrections.

Results in Fig. 2 show that narrow EIT resonance appears after including higher order ($n \geq 3$) corrections of ρ_{23} . The perturbation method reveals that the narrow resonances first appear in the second correction of the ground-state coherences, $\rho_{12}^{x_2}$ and $\rho_{21}^{x_2}$. Also,

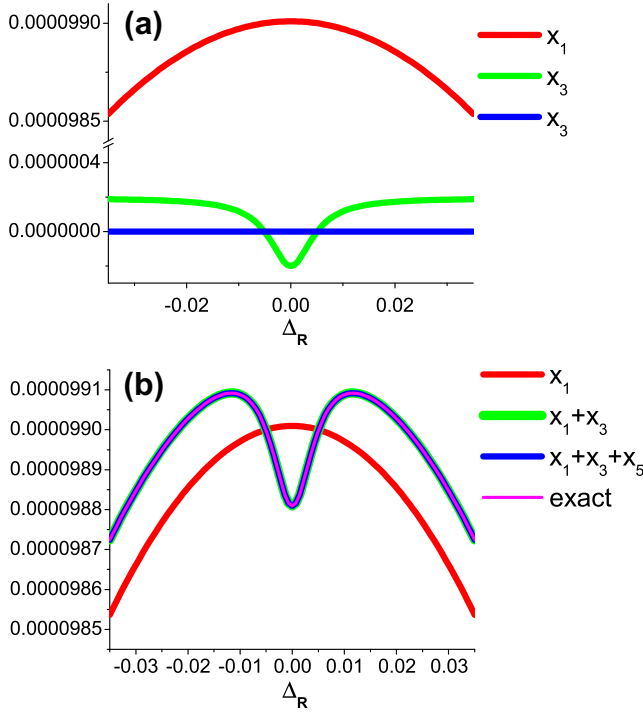


Fig. 2. Successive non-zero corrections (a) and sums of non-zero corrections (b) for density matrix element ρ_{23} . In (b) exact solution is given by magenta curve.

these are the only density-matrix elements showing such narrow resonance in the second correction. These two narrow resonances found in $\rho_{12}^{x_2}$ and $\rho_{21}^{x_2}$ are transferred, by the iterative procedure, to higher-order corrections and lead to the development of EIT.

The analytical expression for the second correction of ground-state coherence, $\rho_{12}^{x_2}$, is:

$$\rho_{12}^{x_2} = -\frac{2(2\gamma + \Gamma + i\Delta_R)}{\gamma + i\Delta_R} \times \left[\frac{e^{i(\varphi_A - \varphi_B)} \Omega_A \Omega_B}{(2\gamma + \Gamma + 2i\Delta_A)(2\gamma + \Gamma - 2i\Delta_A + 2i\Delta_R)} + \frac{e^{i(\varphi_C - \varphi_D)} \Omega_C \Omega_D}{(2\gamma + \Gamma + 2i\Delta_C)(2\gamma + \Gamma - 2i\Delta_C + 2i\Delta_R)} \right], \quad (3)$$

while $\rho_{21}^{x_2}$ is the complex conjugate. Analytical expression for $\rho_{12}^{x_2}$ represents the sum of products of complex Lorentzians (CL). For values of parameters we used here, terms within square bracket in Eq. (3) contain very wide CLs, since $\Gamma \gg \gamma$ and $\Gamma \gg \Delta_{A,B,C,D}$. Next, we approximate wide CLs with $\frac{1}{\Gamma}$ and obtain simple analytical expression in the form of a single narrow complex Lorentzian (nCL):

$$\rho_{12}^{x_2} \cong nCL(\Delta_R) = -\frac{2(e^{i(\varphi_A - \varphi_B)} \Omega_A \Omega_B + e^{i(\varphi_C - \varphi_D)} \Omega_C \Omega_D)}{\Gamma(\gamma + i\Delta_R)} \quad (4)$$

Real part of $nCL(\Delta_R)$ is the analytical expression of the narrow resonance which, as mentioned above, appears when ρ_{23} is plotted against detuning Δ_R .

In Fig. 3 we compare dependence of the optical coherence ρ_{23} and of the second correction of the ground-state coherence $\rho_{12}^{x_2}$, on the relaxation rate γ . Linewidths and amplitudes of two resonances were obtained from fitting numerical results to the sum of very wide and one narrow Lorentzian. Results given in Fig. 3 show that these two resonances have very similar dependence with respect to γ . From analytical expression given in Eq. (4) it can be seen that, for DA system, dependence of EIT's amplitude on γ can be approximated with $\sim \frac{1}{\gamma}$. Linewidths of EIT can be approximated by $\sim \gamma$.

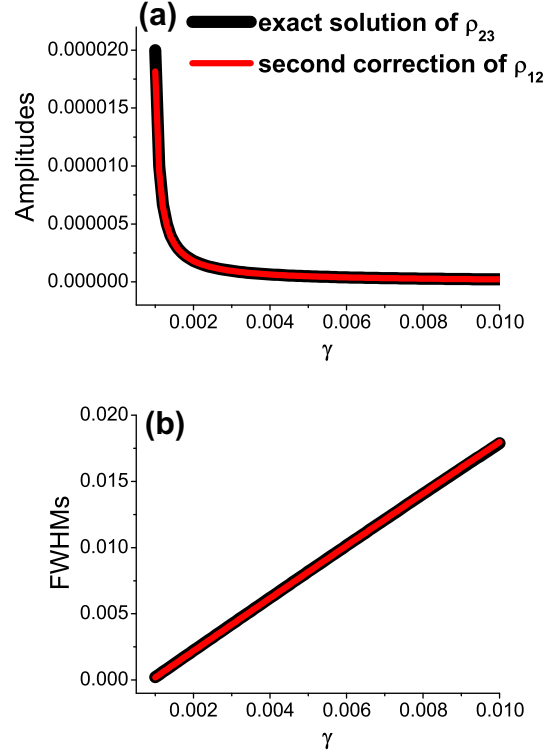


Fig. 3. Comparison of amplitudes (a) and widths (b) on the relaxation rate γ obtained from profiles of the imaginary part of exact solution of ρ_{23} (black curves) and the second correction of ground-state coherence $\rho_{12}^{x_2}$ (red curves). Red curves in figure (a) were normalized with constant number for the easier comparison with black curves. (For interpretation of the references to colour in this figure legend, the reader is referred to the web version of this article.)

For the comparison between the second correction of ground-state coherences and the exact solution for EIT, given in Fig. 3, we have fitted EIT to the sum of very wide and one narrow Lorentzian. Results from Fig. 2 show that the narrow peak developed in the third correction of ρ_{23} is numerically nearly equal to the EIT obtained from the exact solution of the OBEs. We do not present analytical expression of $\rho_{23}^{x_3}$ here since it is just too long. Its form also represents sum of product of CLs, such that some products are only products of wide CLs, and only one is product of wide and one narrow CL. It turns out that the only term showing narrow resonance is the term $\frac{2ie^{i\varphi_A} \Omega_A}{2\gamma + \Gamma + 2i\Delta_A - 2i\Delta_R} \rho_{21}^{x_2}$. All other terms (products) in analytical expression of $\rho_{23}^{x_3}$ are responsible for the broad pedestal around EIT resonance which can be seen in Fig. 2.

4. Conclusion

In conclusion, we have demonstrated how the interaction of a DA atomic scheme with four laser light fields can be treated in a perturbative manner. We presented the example for DA under the conditions when EIT can be observed. Results show that the narrow Lorentzian found in the second correction of ground-state coherences represents an onset of the EIT in all latter corrections and the final solution. We present simple analytical expression for the second correction of ground-state coherences and discuss in which way it affects the final solution for the EIT.

Acknowledgment

This work was supported by the Ministry of Education and Science of the Republic of Serbia, under Grant No. III 45016.

Appendix A. Optical Bloch equations

Optical Bloch equation for the four-level atom are:

$$\dot{\rho}_{ij} = i \sum_k (\rho_{ik} R_{kj} - R_{ik} \rho_{kj}) + i D_{ij} \rho_{ij} + G_{ij} - \gamma \rho_{ij} + \frac{\gamma}{2} \delta_{ij} (\delta_{i1} + \delta_{i2}), \quad i, j = 1, 2, 3, 4, \quad (\text{A.1})$$

where matrices describing certain terms from Eq. (1) are introduced. G is matrix with elements describing spontaneous emission:

$$G = \Gamma \begin{pmatrix} \frac{1}{2}(\rho_{33} + \rho_{44}) & 0 & -\frac{1}{2}\rho_{1,3} & -\frac{1}{2}\rho_{1,4} \\ 0 & \frac{1}{2}(\rho_{33} + \rho_{44}) & -\frac{1}{2}\rho_{2,3} & -\frac{1}{2}\rho_{2,4} \\ -\frac{1}{2}\rho_{3,1} & -\frac{1}{2}\rho_{3,2} & -\rho_{3,3} & -\rho_{3,4} \\ -\frac{1}{2}\rho_{4,1} & -\frac{1}{2}\rho_{4,2} & -\rho_{4,3} & -\rho_{4,4} \end{pmatrix},$$

elements of matrix D are detunings of lasers from the corresponding atomic frequencies:

$$D = \begin{pmatrix} 0 & -\Delta_R & -\Delta_A & -\Delta_C \\ \Delta_R & 0 & -\Delta_B & -\Delta_D \\ \Delta_A & \Delta_B & 0 & -\Delta_E \\ \Delta_C & \Delta_D & \Delta_E & 0 \end{pmatrix},$$

R is matrix with Rabi frequencies describing the interaction part of the Liouville equation:

$$R = \begin{pmatrix} 0 & 0 & e^{i\varphi_A} \Omega_A & e^{i\varphi_C} \Omega_C \\ 0 & 0 & e^{i\varphi_B} \Omega_B & e^{i\varphi_D} \Omega_D \\ e^{-i\varphi_A} \Omega_A & e^{-i\varphi_B} \Omega_B & 0 & 0 \\ e^{-i\varphi_C} \Omega_C & e^{-i\varphi_D} \Omega_D & 0 & 0 \end{pmatrix}$$

and ρ is density matrix.

References

- [1] H. Shpaisman, A.D. Wilson-Gordon, H. Friedmann, Electromagnetically induced waveguiding in double- Λ systems, *Phys. Rev. A* 71 (2005) 043812.
- [2] Baolong Lü, W.H. Burkett, Min Xiao, Nondegenerate four-wave mixing in a double-Lambda system under the influence of coherent population trapping, *Opt. Lett.* 23 (1998) 804–806.
- [3] Olga Kocharovskaya, Li Ruo-Ding, Paul Mandel, Lasing without inversion: the double Λ scheme, *Opt. Commun.* 77 (1990) 215–220.
- [4] A. Eilam, A.D. Wilson-Gordon, H. Friedmann, Slow and stored light in an amplifying double- Λ system, *Opt. Lett.* 33 (2008) 1605–1607.
- [5] Vincent Boyer, Alberto M. Marino, Raphael C. Pooser, Paul D. Lett, Entangled Images from Four-Wave Mixing, *Science* 321 (2008) 544–547.
- [6] Imad H. Agha, Christina Giarmatzis, Quentin Glorieux, Thomas Coudreau, Philippe Grangier, Gaétan Messin, Time-resolved detection of relative-intensity squeezed nanosecond pulses in an 87Rb vapor, *New J. Phys.* 13 (2011) 043030.
- [7] J. Dimitrijević, D. Arsenović, B.M. Jelenković, Coherent processes in electromagnetically induced absorption: a steady and transient study, *New J. Phys.* 13 (2011) 033010.
- [8] A.M. Akulshin, S. Barreiro, A. Lezama, Electromagnetically induced absorption and transparency due to resonant two-field excitation of quasidegenerate levels in Rb vapor, *Phys. Rev. A* 57 (1998) 2996–3002.
- [9] Stephen E. Harris, Electromagnetically induced transparency, *Phys. Today* 50 (1997) 36.
- [10] E.A. Korsunsky, D.V. Kosachiov, Phase-dependent nonlinear optics with double- Λ atoms, *Phys. Rev. A* 60 (1999) 4996–5009.

Continuous reversal of Hanle resonances of a counter-propagating pulse and continuous-wave field

This content has been downloaded from IOPscience. Please scroll down to see the full text.

2014 Laser Phys. 24 015201

(<http://iopscience.iop.org/1555-6611/24/1/015201>)

View [the table of contents for this issue](#), or go to the [journal homepage](#) for more

Download details:

IP Address: 147.91.1.42

This content was downloaded on 08/07/2014 at 12:09

Please note that [terms and conditions apply](#).

Continuous reversal of Hanle resonances of a counter-propagating pulse and continuous-wave field

Jelena Dimitrijević, Dušan Arsenović and Branislav M Jelenković

Institute of Physics, University of Belgrade, Pregrevica 118, 10080 Belgrade, Serbia

E-mail: jelena.dimitrijevic@ipb.ac.rs

Received 17 June 2013

Accepted for publication 6 November 2013

Published 10 December 2013

Abstract

In this work we study propagation dynamics of two counter-propagating lasers, a continuous-wave (CW) laser and the pulse of another laser, when both lasers are tuned to the $F_g = 2 \rightarrow F_e = 1$ transition in ^{87}Rb , and can therefore develop Hanle electromagnetically induced transparency (EIT) in Rb vapor. We calculate the transmission of both lasers as a function of applied magnetic field, and investigate how the propagation of the pulse affects the transmission of the CW laser. Vice versa, we have found conditions when the Gaussian pulse can either pass unchanged, or be significantly absorbed in the vacuum Rb cell. This configuration is therefore suitable for convenient control of the pulse propagation and the system is of interest for optically switching the laser pulses. In terms of the corresponding shapes of the coherent Hanle resonances, this is equivalent to turning the coherent resonance from Hanle EIT into an electromagnetically induced absorption (EIA) peak. There is a range of intensities of both the CW laser and the laser pulse when strong drives of atomic coherences allow the two lasers to interact with each other through atomic coherence and can simultaneously reverse the signs of the Hanle resonances of both.

Keywords: electromagnetically induced transparency, electromagnetically induced absorption, pulse propagation

(Some figures may appear in colour only in the online journal)

1. Introduction

The interaction of atoms with lasers has been one of the most studied subjects during the past few decades. Coherent phenomena in atoms such as coherent population trapping [1], the Hanle effect [2] and related phenomena, electromagnetically induced transparency (EIT) [3] and electromagnetically induced absorption (EIA) [4] have been widely studied under various conditions. EIT and EIA can be induced in different atomic schemes. This can be a pump–probe configuration where two lasers couple two or more hyperfine (or Zeeman) levels. The other way to probe the distribution of atomic coherences is to apply a single optical field, while the transmission of the field is measured as a

function of the magnetic field that varies the energy of Zeeman sublevels, so called Hanle configuration.

EIT and EIA narrow resonances and steep dispersion in the narrow spectral bandwidth of their resonances represent the unique properties of atomic systems. The ability to switch from EIT to EIA could provide a new technique to manipulate the properties of a medium. Yu *et al* [5] demonstrated transformation from the EIT to the EIA in the Hanle configuration when the polarization of a traveling wave changed gradually from linear to circular. This sign reversal was connected with the weak residual transverse magnetic field perpendicular to laser propagation. Bae *et al* [6] recently presented continuous control of the light group velocity from subluminal to superluminal propagation by using the standing-wave coupling field in the transition of the Λ -type

system of ^{87}Rb atoms. When the coupling field changed from a traveling wave to a standing wave by changing the power of the counter-propagating laser field, the speed of the probe pulse changed from subluminal to superluminal propagation.

The counter-propagating geometry and the resulting variations of transmission and refractive index have also been explored. Chanu *et al* [7] recently showed that it is possible to reverse the sign of subnatural resonances in a (degenerate) three-level system. They observed the D2 line of Rb, in a room temperature vapor cell, and change was obtained by turning on a second control beam counter-propagating with respect to the first beam. The role of the different possible subsystems created in this configuration was analyzed [8], together with the possibility of tuning the strength of individual subsystems by changing the polarization of the control lasers.

Counter-propagation dynamics for the Hanle configuration has also been investigated [9–12]. Brazhnikov *et al* [11, 12] recently analyzed the counter-propagating geometry of two CW laser fields in the Hanle configuration. They used the polarization method to reverse the sign of the Hanle resonance of the CW field, and numerical and analytical calculations were performed for simple three-level schemes [11, 12].

In this paper, we present the development of Hanle resonances of two counter-propagating lasers, the CW and the Gaussian pulsed laser. Lasers having orthogonal linear polarizations both couple the $F_g = 2 \rightarrow F_e = 1$ transition in the ^{87}Rb D1 line. Analysis is performed by numerically solving the set of Maxwell–Bloch equations for the same transition including all the magnetic sublevels and for the cold atoms. We have found a range of intensities for both lasers such that they can influence transmission of each other, that is, they can continuously reverse the sign of their resonances from EIT to EIA and *vice versa*, while the pulse is passing through the Rb cell. We are interested for dynamics in two special cases: when the pulse of one laser reverses the sign of the second, CW laser, and when both lasers can simultaneously switch each other's resonance signs.

2. Theoretical model

Here we describe the model that calculates the transmissions of two lasers which act simultaneously on Rb atoms. Namely, there is constant interaction with one laser, CW, and, at the same time, also with the pulse of the second laser. The set of Maxwell–Bloch equations (MBEs) is solved for all magnetic sublevels of the $F_g = 2 \rightarrow F_e = 1$ transition (see figure 1). From the optical Bloch equations (OBEs):

$$\frac{d\hat{\rho}(t)}{dt} = -\frac{i}{\hbar}[\hat{H}_0, \hat{\rho}(t)] - \frac{i}{\hbar}[\hat{H}_I, \hat{\rho}(t)] - \hat{S}\hat{E}\hat{\rho}(t) - \gamma\hat{\rho}(t) + \gamma\hat{\rho}_0 \quad (1)$$

we calculate the evolution of density matrix $\hat{\rho}$. The diagonal elements of the density matrix, ρ_{g_i, g_i} and ρ_{e_i, e_i} , are the populations, ρ_{g_i, g_j} and ρ_{e_i, e_j} are the Zeeman coherences, and ρ_{g_i, e_j} and ρ_{e_i, g_j} are the optical coherences. Here, indices g and e are for the ground and the excited levels, respectively.

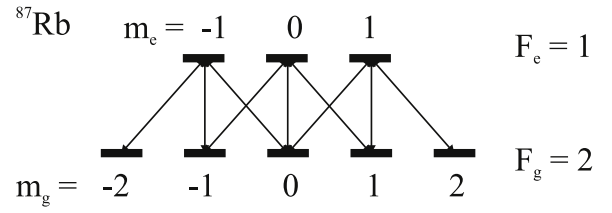


Figure 1. $F_g = 2$ and $F_e = 1$ hyperfine levels with the notation of magnetic sublevels.

MBEs are solved for the Hanle configuration, i.e. when the external magnetic field B is varied around the zero value, as described by the Hamiltonian part \hat{H}_0 . The direction of \vec{B} is the direction of laser propagation and it is also the quantization axis. The Zeeman splitting of the magnetic sublevels is $E_{g(e)} = \mu_B l_{F_{g(e)}} m_{g(e)} B$, where $m_{g(e)}$ are the magnetic quantum numbers of the ground and excited levels, μ_B is the Bohr magneton and $l_{F_{g,e}}$ is the Landé gyromagnetic factor for the hyperfine levels. In equation (1), $\hat{S}\hat{E}$ is the spontaneous emission operator, the rate of which is Γ , and in our calculations we have taken into account that the transition $F_g = 2 \rightarrow F_e = 1$ is open. The term $\gamma\hat{\rho}$ describes the relaxation of all density matrix elements, due to the finite time that an atom spends in the laser beam. The continuous flux of atoms entering the laser beams is described with the term $\gamma\hat{\rho}_0$. We assume equal populations of the ground Zeeman sublevels for these atoms. The role of the laser detuning (and Doppler broadening) is not discussed.

Atoms are interacting with the CW laser, and, for a limited time, they simultaneously also interact with another, pulsed laser. These interactions are described with Hamiltonian \hat{H}_I . The electric field vector represents the sum of two fields:

$$\vec{E}(t, z) = \sum_l [E_x^l \cos(\omega^l t - k^l z + \varphi_x^l) \vec{e}_x + E_y^l \cos(\omega^l t - k^l z + \varphi_y^l) \vec{e}_y]. \quad (2)$$

In equation (2), $\omega^l > 0$ are the laser's (l) angular frequencies $\omega^l = \pm ck^l$, k^l are wavevectors, where we take $k^l < 0$ when the propagation is in the negative direction of the z -axis, and c is the speed of light. E_x^l, E_y^l are the real Descartes components of amplitudes of the electric field while φ_x^l, φ_y^l are associated phases and also real quantities.

We introduce the following substitution:

$$\begin{aligned} E_{++}^l &= \frac{-E_x^l e^{+i\varphi_x^l} + iE_y^l e^{+i\varphi_y^l}}{2\sqrt{2}}, \\ E_{+-}^l &= \frac{-E_x^l e^{-i\varphi_x^l} + iE_y^l e^{-i\varphi_y^l}}{2\sqrt{2}}, \\ E_{-+}^l &= \frac{E_x^l e^{+i\varphi_x^l} + iE_y^l e^{+i\varphi_y^l}}{2\sqrt{2}}, \\ E_{--}^l &= \frac{E_x^l e^{-i\varphi_x^l} + iE_y^l e^{-i\varphi_y^l}}{2\sqrt{2}}. \end{aligned} \quad (3)$$

With this substitution, the electric field vector stands:

$$\vec{E}(t, z) = \sum_1 \vec{E}^1(t, z) \sum_1 [e^{i(\omega^1 t - k^1 z)} \vec{u}_{+1} E_{++}^1 + e^{i(\omega^1 t - k^1 z)} \vec{u}_{-1} E_{-+}^1 + e^{-i(\omega^1 t - k^1 z)} \vec{u}_{+1} E_{+-}^1 + e^{-i(\omega^1 t - k^1 z)} \vec{u}_{-1} E_{--}^1], \quad (4)$$

where \vec{u}_{+1} , \vec{u}_{-1} and \vec{u}_0 are spherical unit vectors [13].

For the case of the two counter-propagating lasers that couple the same transition, we apply the multi-mode Floquet theory [14]. We use the approximation with the zeroth-order harmonics for the ground-state and excited-state density matrices, and up to the first-order harmonics for the optical coherences:

$$\begin{aligned} \rho_{g_i, e_j} &= \sum_1 e^{i(\omega^1 t - k^1 z)} \tilde{\rho}_{g_i, e_j}^1, \\ \rho_{e_i, g_j} &= \sum_1 e^{-i(\omega^1 t - k^1 z)} \tilde{\rho}_{e_i, g_j}^1, \end{aligned} \quad (5)$$

where the sum is taken over lasers that couple states g_i and e_j .

The macroscopic polarization of the atomic medium $\vec{P}(t, z) = N_c \text{Tr}[\hat{\rho} \hat{r}]$ is calculated as

$$\begin{aligned} \vec{P}(t, z) &= N_c \sum_1 [e^{i(\omega^1 t - k^1 z)} (\vec{u}_{+1} P_{++}^1 + \vec{u}_{-1} P_{-+}^1) \\ &\quad + e^{-i(\omega^1 t - k^1 z)} (\vec{u}_{+1} P_{+-}^1 + \vec{u}_{-1} P_{--}^1)], \end{aligned} \quad (6)$$

where we introduced new quantities:

$$\begin{aligned} P_{++}^1 &= - \sum_{g_i \leftrightarrow e_j} \tilde{\rho}_{g_i, e_j}^1 \mu_{e_j, g_i, -1}, \\ P_{+-}^1 &= - \sum_{e_i \leftrightarrow g_j} \tilde{\rho}_{e_i, g_j}^1 \mu_{g_i, e_j, -1}, \\ P_{-+}^1 &= - \sum_{g_i \leftrightarrow e_j} \tilde{\rho}_{g_i, e_j}^1 \mu_{e_j, g_i, +1}, \\ P_{--}^1 &= - \sum_{e_i \leftrightarrow g_j} \tilde{\rho}_{e_i, g_j}^1 \mu_{g_i, e_j, +1}. \end{aligned} \quad (7)$$

The sum is taken over the dipole-allowed transitions induced by lasers (1s).

MBEs are solved for $E_{++}^1, E_{+-}^1, E_{-+}^1, E_{--}^1$ (given by equation (3)) which are complex amplitudes of the fields taking into account the relations $(E_{++}^1)^* = -E_{--}^1$, $(E_{+-}^1)^* = -E_{-+}^1$. MBEs for the propagation along the positive direction of the z -axis are

$$\begin{aligned} \left(-\frac{\partial}{\partial z} + \frac{1}{c} \frac{\partial}{\partial t} \right) E_{++}^1 &= -i \frac{k^1 N_c}{2\epsilon_0} P_{++}^1, \\ \left(-\frac{\partial}{\partial z} + \frac{1}{c} \frac{\partial}{\partial t} \right) E_{-+}^1 &= -i \frac{k^1 N_c}{2\epsilon_0} P_{-+}^1, \\ \left(-\frac{\partial}{\partial z} + \frac{1}{c} \frac{\partial}{\partial t} \right) E_{+-}^1 &= +i \frac{k^1 N_c}{2\epsilon_0} P_{+-}^1, \\ \left(-\frac{\partial}{\partial z} + \frac{1}{c} \frac{\partial}{\partial t} \right) E_{--}^1 &= +i \frac{k^1 N_c}{2\epsilon_0} P_{--}^1, \end{aligned} \quad (8)$$

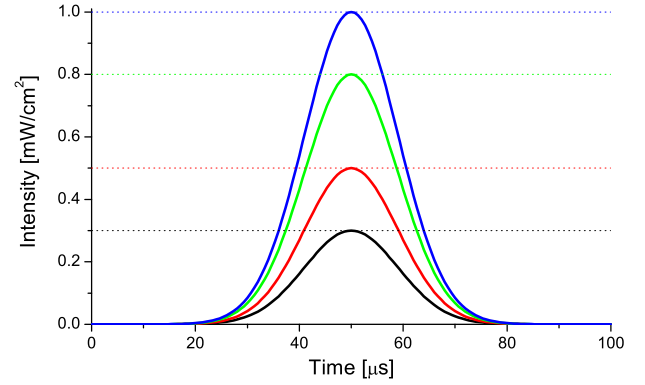


Figure 2. Figure shows the temporal waveforms of the laser amplitudes that we used in our calculations. The dashed lines indicate the amplitudes of the CW laser I_{CW}^0 and the solid lines are temporal waveforms of pulses I_{pulse} .

while those for the propagation along the negative direction of the z -axis are

$$\begin{aligned} \left(-\frac{\partial}{\partial z} + \frac{1}{c} \frac{\partial}{\partial t} \right) E_{++}^1 &= -i \frac{k^1 N_c}{2\epsilon_0} P_{++}^1, \\ \left(-\frac{\partial}{\partial z} + \frac{1}{c} \frac{\partial}{\partial t} \right) E_{-+}^1 &= -i \frac{k^1 N_c}{2\epsilon_0} P_{-+}^1, \\ \left(-\frac{\partial}{\partial z} + \frac{1}{c} \frac{\partial}{\partial t} \right) E_{+-}^1 &= +i \frac{k^1 N_c}{2\epsilon_0} P_{+-}^1, \\ \left(-\frac{\partial}{\partial z} + \frac{1}{c} \frac{\partial}{\partial t} \right) E_{--}^1 &= +i \frac{k^1 N_c}{2\epsilon_0} P_{--}^1. \end{aligned} \quad (9)$$

In the following text, we present results for the transmission of lasers, that is for the averaged power of the laser (I) electromagnetic fields:

$$I^1 = c\epsilon_0 \langle \vec{E}^1 \cdot \vec{E}^1 \rangle. \quad (10)$$

From equation (4) we have

$$\begin{aligned} I^1 &= c\epsilon_0 \langle \{ \vec{u}_{+1} [E_{++}^1 e^{i(\omega^1 t - k^1 z)} + E_{-+}^1 e^{-i(\omega^1 t - k^1 z)}] \\ &\quad + \vec{u}_{-1} [E_{-+}^1 e^{i(\omega^1 t - k^1 z)} + E_{--}^1 e^{-i(\omega^1 t - k^1 z)}] \}^2 \rangle \\ &= -2c\epsilon_0 \{ E_{++}^1 E_{--}^1 + E_{-+}^1 E_{+-}^1 \}. \end{aligned} \quad (11)$$

3. Results and discussion

In this section we present effects on the Hanle EIT of the CW laser when the counter-propagating laser pulse, tuned to the same $F_g = 2 \rightarrow F_e = 1$ transition, passes the Rb cell, overlapping the CW laser. Conversely, we present results when the CW laser controls the transmission and the Hanle EIT of the laser pulse.

Transmissions of lasers are calculated for the values of the external magnetic field near zero, i.e. around the EIT resonance. Polarizations of both lasers are linear and orthogonal. We take the atom concentration in the cell $N_c = 10^{14} \text{ m}^{-3}$, the length of the cell is 10 cm, $\gamma = 0.001 \Gamma$ and the spontaneous emission rate is $\Gamma = 2\pi \cdot 5.75 \text{ MHz}$. The temporal shape of the laser pulse is Gaussian $I_{pulse}^0 e^{-\frac{(t-t_0)^2}{\sigma^2}}$ (see figure 2), where $\sigma = 10 \mu\text{s}/\sqrt{2 \ln 2}$ and I_{pulse}^0 is the

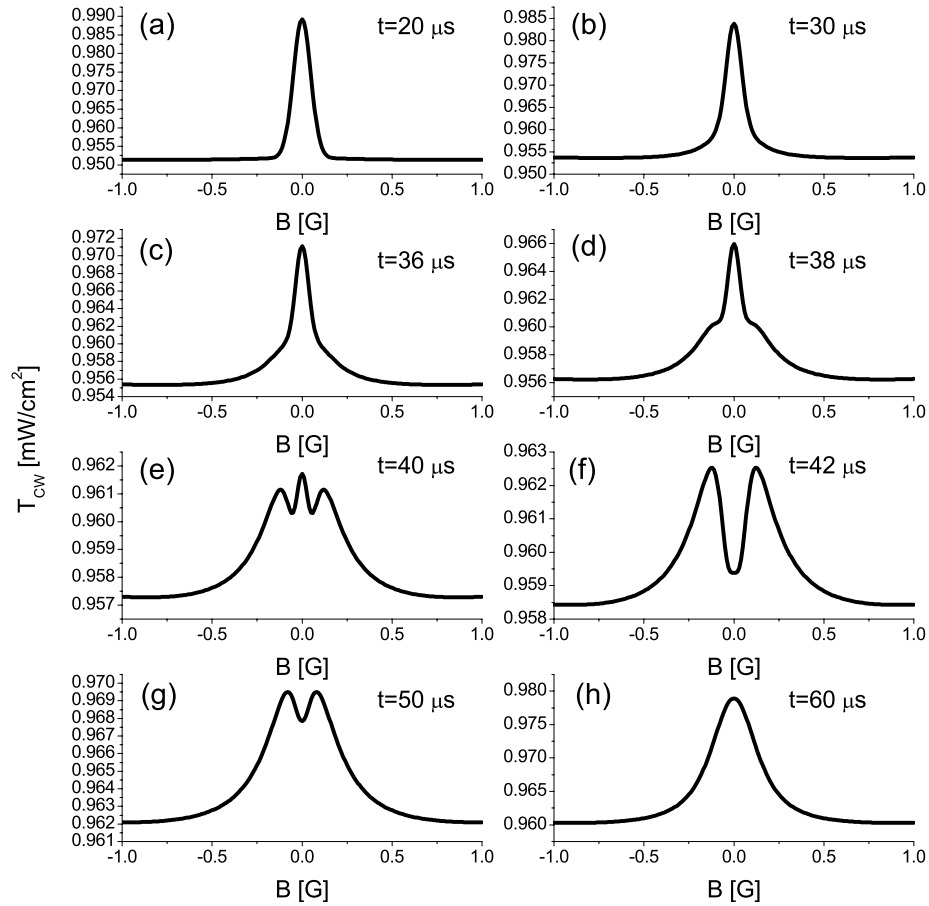


Figure 3. Transmission of the CW laser as a function of the magnetic field B at different times regarding the position of the pulse of the second laser with respect to the Rb cell: $t = 20 \mu\text{s}$ (a), $t = 30 \mu\text{s}$ (b), $t = 36 \mu\text{s}$ (c), $t = 38 \mu\text{s}$ (d), $t = 40 \mu\text{s}$ (e), $t = 42 \mu\text{s}$ (f), $t = 50 \mu\text{s}$ (g) and $t = 60 \mu\text{s}$ (h). The CW laser's intensity is $I_{\text{CW}}^0 = 1 \text{ mW cm}^{-2}$ and the intensity of the pulse at the maximum is $I_{\text{pulse}}^0 = 0.3 \text{ mW cm}^{-2}$ (solid black and dashed blue curves in figure 2). Note that the first curve is before the pulse even enters the cell, while curve (g) is at the time when the pulse is at the highest intensity, as can be seen from figure 2.

intensity of the laser pulse, at the peak of the amplitude at $t_0 = 50 \mu\text{s}$.

Since both lasers are resonant with the $F_g = 2 \rightarrow F_e = 1$ transition in ^{87}Rb , each can independently induce EIT in the atomic vapor. As the pulse enters the cell, its intensity increases, reaches its maximal value I_{pulse}^0 and then decreases. At the very beginning of the pulse, atoms are interacting with the CW laser only, and the transmission of the CW field shows Hanle EIT. As the intensity of the pulse increases, atoms begin to interact with both superimposed fields. The resultant polarization, which is the sum of two orthogonal linear polarizations, can yield very different shapes of transmission resonances of both lasers.

As we see below, complete switching of the sign of the transmission resonance, from transmission gain to absorption gain, can happen depending on the ratio of the pulse's peak intensity I_{pulse}^0 and the intensity of the CW field I_{CW}^0 . We will next discuss two possible cases, $I_{\text{pulse}}^0 < I_{\text{CW}}^0$ and $I_{\text{pulse}}^0 > I_{\text{CW}}^0$.

3.1. Hanle EIT resonances of the CW laser field in the presence of the weak laser pulse

In figure 3 we show changes of the CW laser Hanle EIT as the counter-propagating and spatially overlapping laser pulse

changes its intensity in the Rb cell. Results are for laser intensities $I_{\text{CW}}^0 = 1 \text{ mW cm}^{-2}$ and $I_{\text{pulse}}^0 = 0.3 \text{ mW cm}^{-2}$ (solid black and dashed blue lines in figure 2). As the laser pulse enters the cell the transmission of the CW laser still shows the Hanle EIT. Such is the case with the front of the pulse in the cell, that is for results presented in figures 3(a)–(c). As the pulse intensity increases, this EIT widens and structure begins to form at the resonance center. During the transient period, when the pulse intensity is increasing, there are instances when the CW transmission at the zero value of the external magnetic field totally switches its transmission behavior. Instead of the maximum transmission, when the laser pulse is off, it is maximally absorbed in the cell. It changes sign from EIT to EIA. With the back side of the pulse left in the cell, at time $t = 60 \mu\text{s}$, the transmission of the CW laser again shows EIT, and the resonance stays like this until there is no pulse laser in the cell.

For the choice of laser intensities considered here, $I \leq 1 \text{ mW cm}^{-2}$, and with the condition $I_{\text{pulse}}^0 \leq I_{\text{CW}}^0$, the transmission of the pulse laser shows EIT at all times. Besides intensity broadening, the transmission of the pulse, as a function of the magnetic field, does not change significantly

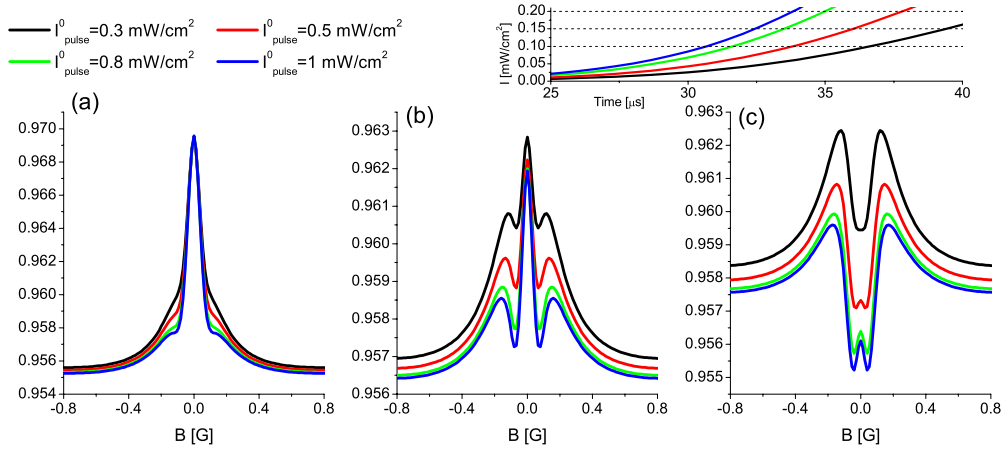


Figure 4. Transmissions of the CW laser for times when the pulse is entering the cell with three different intensities: $I_{\text{pulse}} = 0.1 \text{ mW cm}^{-2}$ (a), $I_{\text{pulse}} = 0.15 \text{ mW cm}^{-2}$ (b) and $I_{\text{pulse}} = 0.2 \text{ mW cm}^{-2}$ (c). For each I_{pulse} we present results for four different rise times of the intensity, i.e., when the pulse has maximum intensities $I_{\text{pulse}}^0 = 0.3 \text{ mW cm}^{-2}$ (black curves), $I_{\text{pulse}}^0 = 0.5 \text{ mW cm}^{-2}$ (red curves), $I_{\text{pulse}}^0 = 0.8 \text{ mW cm}^{-2}$ (green curves) and $I_{\text{pulse}}^0 = 1 \text{ mW cm}^{-2}$ (blue curves). The intensity of the CW laser is $I_{\text{CW}}^0 = 1 \text{ mW cm}^{-2}$. The inset graph shows these three chosen intensities from four pulses as horizontal black dashed lines.

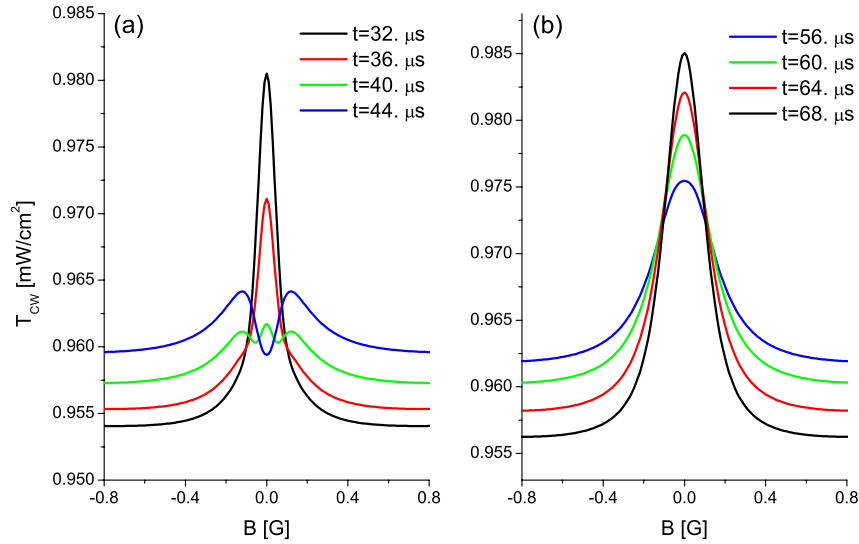


Figure 5. The transmissions of the CW laser, when the pulse laser takes four intensities from the rising (a) and falling (b) edges of the pulse. A certain intensity is chosen from the symmetrical moments of the pulse: $t = 32$ and $68 \mu\text{s}$ (black curves), $t = 36$ and $64 \mu\text{s}$ (red curves), $t = 40$ and $60 \mu\text{s}$ (green curves) and $t = 44$ and $56 \mu\text{s}$ (blue curves). The intensity of the CW laser is $I_{\text{CW}}^0 = 1 \text{ mW cm}^{-2}$ and that of the pulse laser is $I_{\text{pulse}}^0 = 0.3 \text{ mW cm}^{-2}$ (solid black and dashed blue curves in figure 2).

as the pulse passes. Results for the pulse's sign reversal are presented in section 3.2.

In figure 4 we compare the transmissions of the CW laser when four pulses, with different maximum values, have the same intensity in the cell: that is, when pulses whose maxima are $I_{\text{pulse}}^0 = 0.3 \text{ mW cm}^{-2}$ (black curves), $I_{\text{pulse}}^0 = 0.5 \text{ mW cm}^{-2}$ (red curves), $I_{\text{pulse}}^0 = 0.8 \text{ mW cm}^{-2}$ (green curves) and $I_{\text{pulse}}^0 = 1 \text{ mW cm}^{-2}$ (blue curves) (see figure 2), have the same values of $I_{\text{pulse}} = 0.1 \text{ mW cm}^{-2}$ (a), $I_{\text{pulse}} = 0.15 \text{ mW cm}^{-2}$ (b) and $I_{\text{pulse}} = 0.2 \text{ mW cm}^{-2}$ (c).

Results in figure 4 show that, besides the intensity, the slope of the rising front of the pulse also determines the transmissions of the CW laser. Though atoms are affected by the same pulse intensity, as given in separate figures, the transmission of the CW field does not show identical

results when curves are compared. From figure 4 we see that evolution of the EIT/EIA passes through similar stages as the pulse rises, but the speed of the evolution of the EIT/EIA depends on the pulse's slope i.e. its first derivative. This also means that sign reversal of the CW laser, for different Gaussian pulses (different maximal intensities), does not happen simultaneously.

In figure 5 we show that the rising and falling edges of the laser pulses, with the same intensity, have different effects on the CW laser transmission. For the CW laser intensity of $I_{\text{CW}}^0 = 1 \text{ mW cm}^{-2}$ and for the pulse laser maximum intensity of $I_{\text{pulse}}^0 = 0.3 \text{ mW cm}^{-2}$, we present the CW laser transmission for four pairs of equal pulse laser intensity; each pair has the same intensity on both sides of the laser pulse. We choose the following pairs of intensities of the laser pulse,

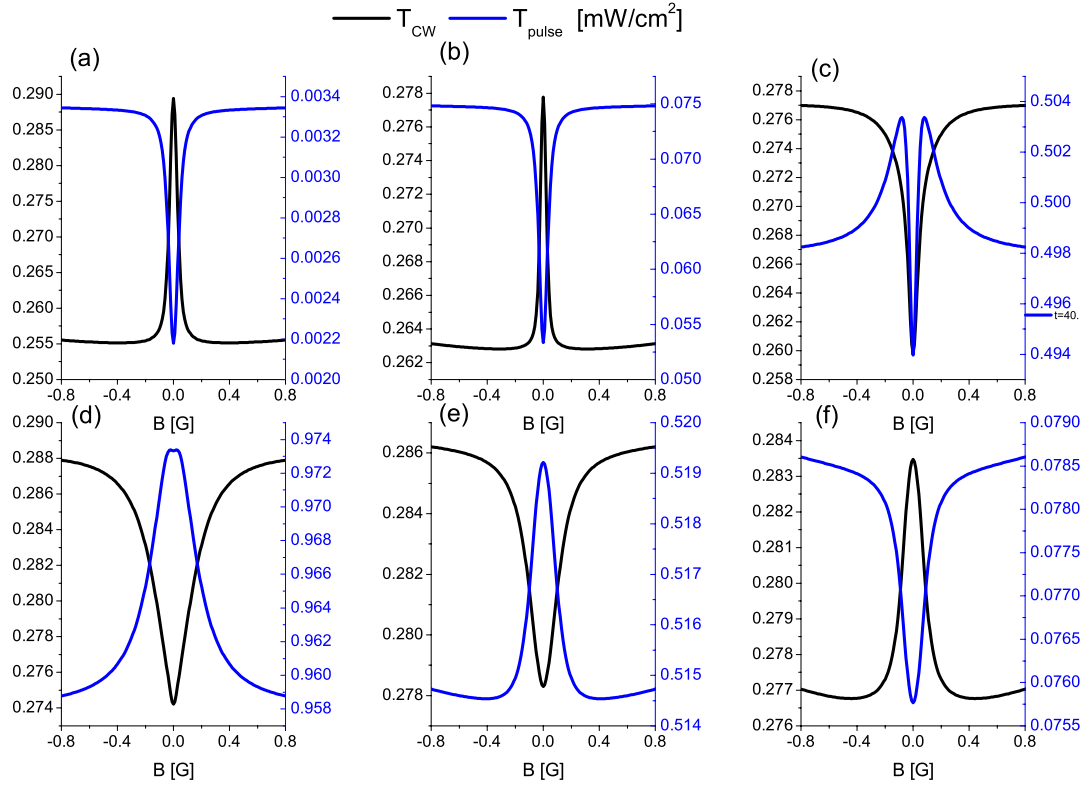


Figure 6. Transmissions of both the CW laser and the pulse as a function of the magnetic field: CW laser (black curves and black y-axis) and pulse laser (blue curves and blue y-axis). The amplitude of the CW laser's electric field is $I_{\text{CW}}^0 = 0.3 \text{ mW cm}^{-2}$ and the pulse's maximum value is $I_{\text{pulse}}^0 = 1 \text{ mW cm}^{-2}$ (solid blue and dashed black curves in figure 2). Results are presented for six values of the intensity of the Gaussian laser pulse as it passes through the cell, from $t = 20$ to $70 \mu\text{s}$ in steps of $10 \mu\text{s}$: $t = 20 \mu\text{s}$ (a), $t = 30 \mu\text{s}$ (b), $t = 40 \mu\text{s}$ (c), $t = 50 \mu\text{s}$ (d), $t = 60 \mu\text{s}$ (e) and $t = 70 \mu\text{s}$ (f).

i.e., for the pulse instants $t = 32$ and $68 \mu\text{s}$ (black curves), $t = 36$ and $64 \mu\text{s}$ (red curves), $t = 40$ and $60 \mu\text{s}$ (green curves) and $t = 44$ and $56 \mu\text{s}$ (blue curves).

The results given in figure 5 indicate that the transmissions of the CW field are not symmetrical with respect to the pulse maximum intensity. Depending on whether the CW laser is overlapped with the rising (figure 5(a)) or the falling (figure 5(b)) edge of the pulse, the profiles have different waveforms, although the intensities are the same. A similar result of this 'memory effect' has also been discussed by Ignesti *et al* [15]. It was theoretically predicted that spectral enlargement or compression process occurs when the probe pulse is overlapped by a coupling pulse field with a positive or negative temporal slope, and experimental confirmation was obtained for a scheme in sodium atomic vapor [15]. At the rising edge of the pulse, while the dark-state is being formed, there are rapid changes in the transmission of the CW laser. The profiles at the falling edge of the pulse are due to long-lived ground-state coherences, created at the earlier time of the pulse propagation. After a certain time the dark-state is established and further decrease of the pulse's intensity does not affect the formed dark-state.

3.2. Switching signs of both laser transmissions

Our analysis indicates that the simultaneous switching of signs of transmission resonances of both CW and pulse laser

fields is when the intensity of the CW field is comparable to the pulse laser intensity, that is $I_{\text{CW}}^0 \leq I_{\text{pulse}}^0$. For this ratio of intensities, when the pulse laser intensity after a certain time reaches the intensity of the CW laser, the intensities of the two lasers are comparable (see figure 2) and reversals of the signs of both are possible.

In figure 6 we present the transmissions of both lasers on the corresponding sides of the cell. For the case $I_{\text{pulse}}^0 > I_{\text{CW}}^0$ (we analyzed range of intensities $I \leq 1 \text{ mW cm}^{-2}$) both lasers are switching each other's resonance signs. The switching happens only at the time when the pulse intensity varies near its maximum; therefore, it is a very fast and short optical switch. Results in figures 6(d) and (e) show that both lasers have completely changed the sign of resonance from EIT/EIA to EIA/EIT. Results also show that there is a mirror symmetry between the transmission of the CW and pulse lasers. Both lasers change the sign of resonance simultaneously. The only exception to this is around $t = 40 \mu\text{s}$, when both lasers show EIA, when there are also most drastic changes in the evolution of the atomic ensemble.

We also calculated the transmission of the laser pulse for four values of the CW laser intensities. Results are given in figure 7 for $I_{\text{CW}}^0 = 0.3 \text{ mW cm}^{-2}$ (black curves), $I_{\text{CW}}^0 = 0.5 \text{ mW cm}^{-2}$ (red curves), $I_{\text{CW}}^0 = 0.8 \text{ mW cm}^{-2}$ (green curves) and $I_{\text{CW}}^0 = 1 \text{ mW cm}^{-2}$ (blue curves). The intensity of the pulse laser is $I_{\text{pulse}}^0 = 1 \text{ mW cm}^{-2}$. We observe the pulse's Hanle resonance in transmissions for three different

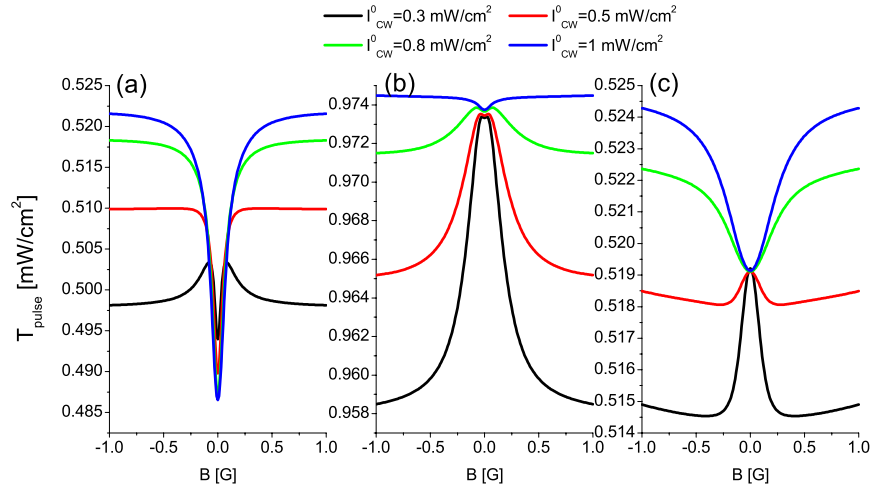


Figure 7. Transmissions of the pulse fields, when the CW laser takes different intensities: $I_{CW}^0 = 0.3 \text{ mW cm}^{-2}$ (black curves), $I_{CW}^0 = 0.5 \text{ mW cm}^{-2}$ (red curves), $I_{CW}^0 = 0.8 \text{ mW cm}^{-2}$ (green curves) and $I_{CW}^0 = 1 \text{ mW cm}^{-2}$ (blue curves). We observe transmissions at three different moments in time: $t = 40 \mu\text{s}$ (a), $t = 50 \mu\text{s}$ (b) and $t = 60 \mu\text{s}$ (c). The maximum intensity of the pulse laser is kept constant, $I_{\text{pulse}}^0 = 1 \text{ mW cm}^{-2}$.

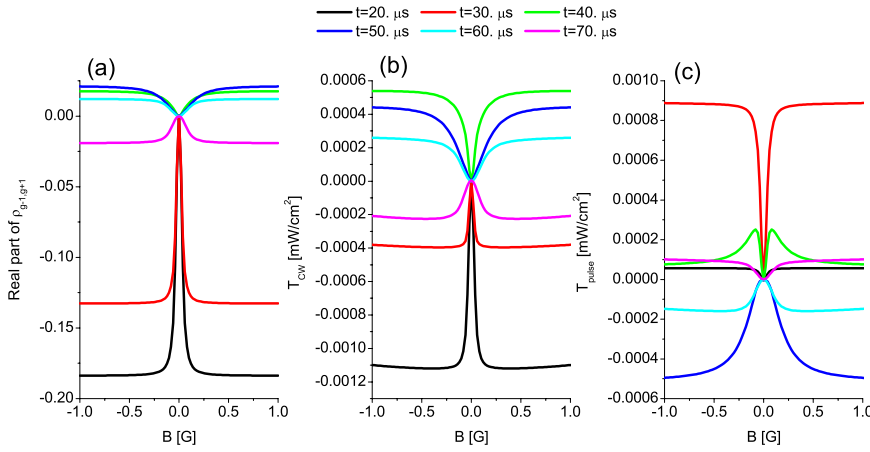


Figure 8. Real part of the ground-state coherences $\rho_{g-1,g+1}$ (a) and transmissions of the CW laser (b) and pulse laser (c) for six times during the time development of the pulse, from $t = 20$ to $70 \mu\text{s}$ in steps of $10 \mu\text{s}$. Results for the coherences are calculated in the middle of the cell, $z = 0.05 \text{ m}$. The curves in all three graphs are y-shifted such that they coincide in $B = 0$.

times: $t = 40 \mu\text{s}$ (a), $t = 50 \mu\text{s}$ (b) and $t = 60 \mu\text{s}$ (c). Results show that when the intensity of the CW field is varied, the transmission of the pulse laser at the zero magnetic field, for $B = 0$, remains constant at all times. The condition for CPT in the Hanle configuration is fulfilled at zero magnetic field, and is, in this case, well established by the pulse's stronger laser. As can be seen in figures 7(b) and (c), the rest of the pulse transmission profile, which violates the exact condition for the dark-state fulfilled at zero magnetic field, can show either EIT or EIA depending on the strength of the CW field intensity.

In figure 8 we present the real part of the ground-state coherences $\rho_{g-1,g+1}$ (a) and compare them with the transmissions of the CW laser (b) and pulse laser (c). Different colors indicate different intensities applied, i.e. different moments of the pulse propagation, from $t = 20$ to $70 \mu\text{s}$ in steps of $10 \mu\text{s}$, whereas the intensity of the CW laser is constant, $I_{CW}^0 = 0.3 \text{ mW cm}^{-2}$. Curves in all three graphs are shifted along the y-axis for easier comparison. We present

results in the middle of the cell, since changes along the cell are negligible. In this configuration, the transmission of the CW laser matches the sign of the ground-state coherences, while that of the pulse laser is of the opposite sign. Results presented in figure 8 confirm that the behavior of the transmissions of both lasers closely follows the behavior of the ground-state coherences.

4. Conclusion

We have analyzed the propagation dynamics of two counter-propagating laser fields with Rb atoms in the Hanle configuration, one of which is a Gaussian pulse and the other is CW. We demonstrated continuous sign reversal of both lasers in the Hanle configuration. Sign reversal was obtained in two ways, of only the CW laser field and of both lasers. The choice lies in the ratio of the lasers' intensities. We have also analyzed peculiarities of these two cases, different slopes of pulses, the effect of different intensities and the behavior

of the ground-state coherences. The results obtained in this work may provide a useful reference for further research and interesting applications of EIT and EIA ultranarrow resonances.

Acknowledgment

This work was supported by the Ministry of Education and Science of the Republic of Serbia, under grant number III 45016.

References

- [1] Aspect A, Arimondo E, Kaiser R, Vansteenkiste N and Cohen-Tannoudji C 1988 *Phys. Rev. Lett.* **61** 826
- [2] Moruzzi G and Strumia F (ed) 1991 *The Hanle Effect and Level-Crossing Spectroscopy* (New York: Plenum) (Engl. transl.)
- [3] Arimondo E 1996 *Prog. Opt.* **35** 257
- [4] Akulshin A M, Barreiro S and Lezama A 1998 *Phys. Rev. A* **57** 2996
- [5] Yu Y J, Lee H J, Bae I H, Noh H R and Moon H S 2010 *Phys. Rev. A* **81** 023416
- [6] Bae I H and Moon H S 2011 *Phys. Rev. A* **83** 053806
- [7] Chanu S R, Pandey K and Natarajan V 2012 *Europhys. Lett.* **98** 44009
- [8] Pandey K 2013 *Phys. Rev. A* **87** 043838
- [9] Zibrov S A, Dudin Y O, Radnaev A G, Vassiliev V V, Velichansky V L, Brazhnikov D V, Taichenachev A V and Yudin V I 2007 *JETP Lett.* **85** 417
- [10] Zhukov A, Zibrov S A, Romanov G V, Dudin Y O, Vassiliev V V, Velichansky V L and Yakovlev V P 2009 *Phys. Rev. A* **80** 033830
- [11] Brazhnikov D V, Taichenachev A V, Tumaikin A M, Yudin V I, Ryabtsev I I and Entin V M 2010 *JETP Lett.* **91** 625
- [12] Brazhnikov D V, Taichenachev A V and Yudin V I 2011 *Eur. Phys. J. D* **63** 315
- [13] Edmonds A R 1974 *Angular Momentum in Quantum Mechanics* (Princeton, NJ: Princeton University Press)
- [14] Chu S I and Telnov D A 2004 *Phys. Rep.* **390** 1
- [15] Ignesti E, Buffa R, Fini L, Sali E, Tognetti M V and Cavalieri S 2011 *Phys. Rev. A* **83** 053411

Nonlinear polarization rotation of a Gaussian pulse propagating through an EIT medium

This content has been downloaded from IOPscience. Please scroll down to see the full text.

2014 J. Phys. B: At. Mol. Opt. Phys. 47 045503

(<http://iopscience.iop.org/0953-4075/47/4/045503>)

View [the table of contents for this issue](#), or go to the [journal homepage](#) for more

Download details:

IP Address: 147.91.1.42

This content was downloaded on 08/07/2014 at 12:11

Please note that [terms and conditions apply](#).

Nonlinear polarization rotation of a Gaussian pulse propagating through an EIT medium

J Dimitrijević, D Arsenović and B M Jelenković

Institute of Physics, University of Belgrade, Pregrevica 118, 10080 Belgrade, Serbia

E-mail: jelena.dimitrijevic@ipb.ac.rs

Received 26 September 2013, revised 19 December 2013

Accepted for publication 30 December 2013

Published 4 February 2014

Abstract

We study numerically the nonlinear magneto-optical rotation of polarization (NMOR) of the laser pulse during its propagation through a cold Rb cloud with induced Zeeman coherences and electromagnetically induced transparency. Evolution of NMOR is calculated by solving the Maxwell–Bloch equations. We consider a linearly polarized Gaussian pulse with different pulse peak amplitudes and widths. For an intensity peak of 5 mW cm^{-2} and full-width at half-maximum of $10 \mu\text{s}$, transient behaviour of NMOR does not follow the pulse intensity variation: NMOR begins to decrease as the pulse's intensity nears its peak value. When the pulse has a smaller peak intensity, NMOR behaves qualitatively differently: the angle of rotation constantly increases during the pulse propagation. Observed differences are explained by the optical pumping into the dark state and the behaviour of the ground-state coherences subjected to coherent population trapping. The same pulse intensity, from different sides of the pulse, during rising and falling sides, produces qualitatively different NMOR shapes, its amplitudes and widths which result can be explained by the successive excitation of atoms during the pulse propagation. It was shown that increasing the relaxation rates of the ground-state coherences, shifts the maximum of the NMOR to higher magnetic field, while the atomic density strongly influences the magnitude of the NMOR.

Keywords: magneto-optical effects, electromagnetically induced transparency, electromagnetic pulses, light propagation

(Some figures may appear in colour only in the online journal)

1. Introduction

Rotation of the polarization plane of light travelling through an atomic vapour, subjected to magnetic field, has been studied for more than a century. The main characteristic of the linear resonant Faraday effect is that, for Larmor frequencies smaller than the resonance line width, the magnitude of the rotation is proportional to a magnetic field. For nonlinear magneto-optical rotation (NMOR) [1, 2], nonlinear contributions appear in characteristic, dispersively shaped dependence on the magnetic field.

The origin of magneto-optical rotation lies in the fact that the medium behaves differently for the two components of the field, displaying what is known as circular birefringence

or linear dichroism. The magnetic field, when applied to an initially isotropic medium, creates asymmetry between medium susceptibilities, corresponding to two circularly polarized components of the field. Asymmetry can happen when the magnetic field is longitudinal with respect to light propagation (Faraday effect, causing circular birefringence) or is transverse to \vec{k} (Voigt effect, causing linear dichroism). Resultant circular birefringence and linear dichroism induce magneto-optical rotation, i.e. the polarization plane of the light emerging out of the medium is rotated with respect to that of the incident.

It is however interesting to relate NMOR to the combined effects of the laser field and the magnetic field in the context of coherent control of the polarization rotation [3–5]. Namely,

NMOR is associated with the light-generated redistribution of populations by optical pumping, and also by the creation of coherences between magnetic sublevels of atomic or molecular ground and/or excited states. This makes NMOR closely related to other coherence effects, like electromagnetically induced transparency (EIT) [6, 7], coherence population trapping (CPT) [8, 9] and the slow propagation of light [10, 11].

NMOR is typically studied as a function of light detuning from atomic resonance, in the presence of the constant magnetic field or as a function of the magnetic field for the light tuned to the resonance. When both laser field and the external magnetic field are present, transmission line shapes show interplay between two fields resulting with suppressed and enhanced rotation signals. Also, NMOR is typically studied for the continuous-wave fields when it is of interest to know the amount of rotation in the steady state. However, in the case of amplitude modulated electromagnetic field propagating through the resonant gaseous media, the presence of magnetic field leads to time-dependent magneto-optical rotation.

Interest in laser pulse NMOR is focused on achieving a better understanding of the relation between polarization of the medium during the pulse propagation, and the subsequent effects on the polarization of the light pulse. Investigation of pulse NMOR behaviour is then directly related to studies of pulse propagation through atomic medium [11], slow and stored light [12, 13] and optical switching [14]. The NMOR of pulsed light has been analysed in the context of slow light [15–17]. Budker *et al* [15] demonstrated the relation between the reduced light group velocity and nonlinear magneto-optics. It was shown that the time-dependent optical rotation can mask the storage of light signal [16]. Ruseckas *et al* [17] have shown that the orbital angular momentum of slow light manifests in a rotation of the polarization plane of linearly polarized light.

In this paper we study theoretically the transient NMOR behaviour of the light pulse propagating through the atomic medium in the presence of longitudinal magnetic field. Frequency of the linearly polarized light is tuned to the $F_g = 2 \rightarrow F_e = 1$ hyperfine transition in the Rb, D1 line. Therefore, the pulse is inducing EIT in the atomic medium as it propagates. The properties of NMOR are obtained by solving density matrix equations for the atomic coherences and populations along with the Maxwell equations describing pulse propagation of the electromagnetic field through the cold gas. We assume the Gaussian shape for the light pulse and perform calculations for different pulse amplitudes and widths. Transient behaviour of NMOR is compared to that of ground-state coherences subjected to CPT, and their relation is discussed. Influence of ground-states relaxation and atomic density on the magnetic field dependence of rotation angle, as the pulse propagates through the atomic medium, is presented.

2. Theoretical model

We solve the Maxwell–Bloch equations for the $F_g = 2 \rightarrow F_e = 1$ transition (see figure 1) in the ^{87}Rb , D1 line, for different longitudinal magnetic fields. Evolution of the density matrix $\hat{\rho}(t, z)$ is obtained from the optical-Bloch equations:

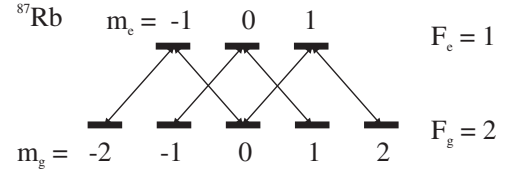


Figure 1. $F_g = 2$ and $F_e = 1$ hyperfine levels with the notation of magnetic sublevels.

$$\frac{d\hat{\rho}(t, z)}{dt} = -\frac{i}{\hbar}[\hat{H}_0, \hat{\rho}(t, z)] - \frac{i}{\hbar}[\hat{H}_I, \hat{\rho}(t, z)] - \hat{S}\hat{E}\hat{\rho}(t, z) - \gamma\hat{\rho}(t, z) + \gamma\hat{\rho}_0. \quad (1)$$

From equation (1) we calculate the evolution of the density matrix $\hat{\rho}$. Indexes g and e stand for the ground and excited levels, respectively. The diagonal elements of the density matrix, ρ_{g_i, g_i} and ρ_{e_i, e_i} are the populations, while elements ρ_{g_i, g_j} and ρ_{e_i, e_j} are Zeeman coherences, and ρ_{g_i, e_j} and ρ_{e_i, g_j} are optical coherences. The usual substitution for optical coherences has been introduced:

$$\begin{aligned} \rho_{g_i, e_j} &= e^{i\omega t - ikz} \tilde{\rho}_{g_i, e_j}, \\ \rho_{e_i, g_j} &= e^{-i\omega t + ikz} \tilde{\rho}_{e_i, g_j}. \end{aligned} \quad (2)$$

In equation (1), \hat{H}_0 describes the interaction of Rb atoms with magnetic field \vec{B} . The direction of the magnetic field is also the direction of the pulse propagation and is taken to be the quantization axis. Magnetic sublevels are split due to the Zeeman effect by $E_{g(e)} = \mu_B l_{F_{g(e)}} m_{g(e)} B$, where $m_{g(e)}$ are magnetic quantum numbers of the ground and excited levels, μ_B is the Bohr magneton and $l_{F_{g,e}}$ is the Landé gyromagnetic factor for the hyperfine level. The interaction of atoms with electromagnetic pulse, with electric field vector $\vec{E}(t, z)$, is given with Hamiltonian \hat{H}_I . $\hat{S}\hat{E}$ is the spontaneous emission operator with the rate Γ . Due to a finite time that an atom spends in the laser beam, all density matrix elements are relaxing with the same rate γ . The term $\gamma\hat{\rho}_0$ describes the continuous flux of atoms entering the laser beam, where we take equal population of the ground Zeeman sublevels for these atoms. The role of the laser detuning is not discussed.

The electric field vector is

$$\begin{aligned} \vec{E}(t, z) &= \vec{e}_x E_x(t, z) \cos(\omega t - kz + \varphi_x(t, z)) \\ &+ \vec{e}_y E_y(t, z) \cos(\omega t - kz + \varphi_y(t, z)), \end{aligned} \quad (3)$$

where $\omega > 0$ is the laser angular frequency, $\omega = \pm ck$, \vec{k} is the wave vector (we take $k > 0$ for the propagation towards the positive direction of the z -axis) and c is the speed of light. $E_x(t, z)$ and $E_y(t, z)$ are real Cartesian components of the electric field amplitude, while real quantities $\varphi_x(t, z)$ and $\varphi_y(t, z)$ are associated phases. In the following text we omit dependence of all quantities on t and z .

The angle of rotation ϕ is introduced here, when Cartesian unit vectors are rotated like

$$\vec{e}_x \rightarrow \vec{e}_x \cos \phi + \vec{e}_y \sin \phi, \quad \vec{e}_y \rightarrow \vec{e}_y \cos \phi - \vec{e}_x \sin \phi. \quad (4)$$

The electric field vector \vec{E} , when cosine functions in equation (3) are written in exponential form, is

$$\begin{aligned}\vec{E} = & \frac{1}{2}E_x(\vec{e}_x \cos \phi + \vec{e}_y \sin \phi)e^{i\omega t - ikz + i\varphi_x} \\ & + \frac{1}{2}E_x(\vec{e}_x \cos \phi + \vec{e}_y \sin \phi)e^{-i\omega t + ikz - i\varphi_x} \\ & + \frac{1}{2}E_y(\vec{e}_y \cos \phi - \vec{e}_x \sin \phi)e^{i\omega t - ikz + i\varphi_y} \\ & + \frac{1}{2}E_y(\vec{e}_y \cos \phi - \vec{e}_x \sin \phi)e^{-i\omega t + ikz - i\varphi_y}.\end{aligned}\quad (5)$$

After we make transformation to the complex spherical unit vectors basis:

$$\vec{e}_x = \frac{\vec{\sigma}^- - \vec{\sigma}^+}{\sqrt{2}}, \quad \vec{e}_y = \frac{i(\vec{\sigma}^- + \vec{\sigma}^+)}{\sqrt{2}}, \quad \vec{e}_z = \vec{\sigma}^0, \quad (6)$$

the electric field vector is given in terms of complex amplitudes, E_{++} , E_{+-} , E_{-+} and E_{--} as

$$\begin{aligned}\vec{E} = & e^{i\omega t - ikz}(\vec{\sigma}^- E_{-+} + \vec{\sigma}^+ E_{++}) \\ & + e^{-i\omega t + ikz}(\vec{\sigma}^- E_{--} + \vec{\sigma}^+ E_{+-}).\end{aligned}\quad (7)$$

In equation (7) the following substitution has been made:

$$\begin{aligned}E_{+-} = & \frac{e^{-i\phi}}{2\sqrt{2}}(-E_x e^{-i\varphi_x} + iE_y e^{-i\varphi_y}), \\ E_{--} = & \frac{e^{i\phi}}{2\sqrt{2}}(E_x e^{-i\varphi_x} + iE_y e^{-i\varphi_y}), \\ E_{++} = & \frac{e^{-i\phi}}{2\sqrt{2}}(-E_x e^{i\varphi_x} + iE_y e^{i\varphi_y}), \\ E_{-+} = & \frac{e^{i\phi}}{2\sqrt{2}}(E_x e^{i\varphi_x} + iE_y e^{i\varphi_y}).\end{aligned}\quad (8)$$

From equation (8) we see that complex amplitudes of electric field are not mutually independent i.e. $(E_{++})^* = -E_{--}$ and $(E_{+-})^* = -E_{-+}$.

Maxwell-Bloch equations representing equations of motion for the complex amplitudes E_{++} , E_{+-} , E_{-+} and E_{--} (given in equation (8)) are solved for the propagation along the z -axis:

$$\begin{aligned}\left(\frac{\partial}{\partial z} + \frac{1}{c}\frac{\partial}{\partial t}\right)E_{+-} = & +i\frac{kN_c}{2\varepsilon_0}P_{+-}, \\ \left(\frac{\partial}{\partial z} + \frac{1}{c}\frac{\partial}{\partial t}\right)E_{--} = & +i\frac{kN_c}{2\varepsilon_0}P_{--}, \\ \left(\frac{\partial}{\partial z} + \frac{1}{c}\frac{\partial}{\partial t}\right)E_{++} = & -i\frac{kN_c}{2\varepsilon_0}P_{++}, \\ \left(\frac{\partial}{\partial z} + \frac{1}{c}\frac{\partial}{\partial t}\right)E_{-+} = & -i\frac{kN_c}{2\varepsilon_0}P_{-+}.\end{aligned}\quad (9)$$

In equation (9) we introduced the following quantities:

$$\begin{aligned}P_{+-} = & -\sum_{e_i \leftrightarrow g_j} \tilde{\rho}_{e_i, g_j} \mu_{g_j, e_i, -1}, \\ P_{--} = & -\sum_{e_i \leftrightarrow g_j} \tilde{\rho}_{e_i, g_j} \mu_{g_j, e_i, +1}, \\ P_{++} = & -\sum_{g_i \leftrightarrow e_j} \tilde{\rho}_{g_i, e_j} \mu_{e_j, g_i, -1}, \\ P_{-+} = & -\sum_{g_i \leftrightarrow e_j} \tilde{\rho}_{g_i, e_j} \mu_{e_j, g_i, +1},\end{aligned}\quad (10)$$

where summation is taken over dipole-allowed transitions induced by the laser. These four variables represent components of the macroscopic polarization of the atomic medium:

$$\begin{aligned}\vec{P}(t, z) = & N_c e \text{Tr}[\hat{\rho} \hat{r}] \\ = & N_c [e^{i\omega t - ikz}(\vec{\sigma}^- P_{-+} + \vec{\sigma}^+ P_{++}) \\ & + e^{-i\omega t + ikz}(\vec{\sigma}^- P_{--} + \vec{\sigma}^+ P_{+-})],\end{aligned}\quad (11)$$

where N_c is the concentration of Rb atoms.

To obtain the angle of rotation ϕ we take the third and fourth lines of equation (8) and set $\varphi_y = \varphi_x + \frac{\pi}{2}$:

$$\begin{aligned}E_{++} = & -\frac{(E_x + E_y)}{2\sqrt{2}}e^{i\varphi_x - i\phi}, \\ E_{-+} = & \frac{(E_x - E_y)}{2\sqrt{2}}e^{i\varphi_x + i\phi},\end{aligned}\quad (12)$$

i.e.,

$$\begin{aligned}|E_{++}| = & \frac{(E_x + E_y)}{2\sqrt{2}}, \quad \arg(E_{++}) = \varphi_x - \phi + \pi + 2\pi n_1, \\ |E_{-+}| = & \frac{(E_x - E_y)}{2\sqrt{2}}, \quad \arg(E_{-+}) = \varphi_x + \phi + 2\pi n_2.\end{aligned}\quad (13)$$

From equation (13) we obtain

$$\phi = \frac{1}{2}(\arg(E_{-+}) - \arg(E_{++}) - 2\pi(n_2 - n_1) + \pi). \quad (14)$$

For the results presented in the next section we have $\phi(0, 0) = 0$ and from equation (14) we calculate the polarization rotation along the atomic medium and for different times during the pulse propagation $\phi(t, z)$.

Results for the transmission of the laser will also be presented in the next section. They represent the power average of the laser electromagnetic field, $I = c\varepsilon_0 \langle \vec{E} \cdot \vec{E} \rangle$. From equation (7) we have

$$\begin{aligned}I = & c\varepsilon_0 \langle \{ \vec{\sigma}^- (E_{-+} e^{i\omega t - ikz} + E_{--} e^{-i\omega t + ikz}) \\ & + \vec{\sigma}^+ (E_{++} e^{i\omega t - ikz} + E_{+-} e^{-i\omega t + ikz}) \}^2 \rangle \\ = & -2c\varepsilon_0 (E_{++}E_{--} + E_{-+}E_{+-}).\end{aligned}\quad (15)$$

3. Results and discussion

In this section we present results for the evolution of the NMOR for the linearly polarized light pulse as the pulse propagates through the $L = 0.1$ m long Rb atomic cloud. The pulse laser frequency is tuned to the $F_g = 2 \rightarrow F_e = 1$ transition of the ^{87}Rb , D1 line. Results are calculated for magnetic fields corresponding to the EIT resonance. The spontaneous emission rate is $\Gamma = 2\pi \cdot 5.75006$ MHz and the concentration of Rb atoms, if not emphasized differently, is $N_c = 10^{14} \times 1 \text{ m}^{-3}$. The rate of relaxation due to time of flight $\gamma = 0.001 \Gamma$. Temporal wave-form of the propagating laser pulse is Gaussian (see figure 2):

$$I(t) = I^0 \exp\left(-\frac{(t - t_c)^2}{\frac{\Delta_w^2}{4 \log(2)}}\right), \quad (16)$$

where I^0 is the pulse peak intensity at the centre of the pulse t_c and Δ_w is the full-width at half-maximum. We point out that transmission and NMOR signals can readily be obtained experimentally from transient wave-forms of a transmitted laser pulse, at large number of magnetic field values within the EIT spectral bandwidth.

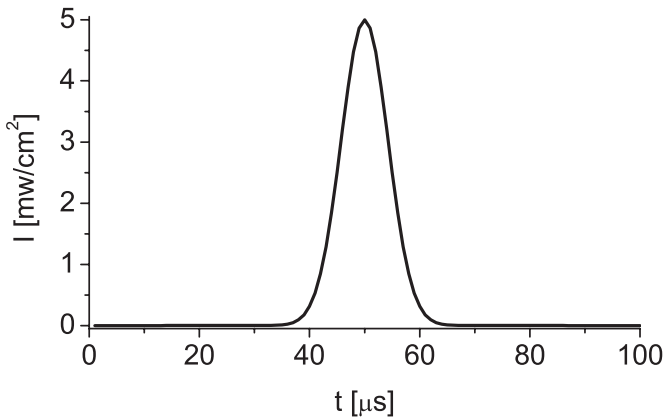


Figure 2. Gaussian wave-form of the light pulse used in the calculations. The pulse peak intensity is $I^0 = 5 \text{ mW cm}^{-2}$, centred at $t_c = 50 \text{ μs}$ and $\Delta_W = 10 \text{ μs}$.

The origin of EIT lies in the CPT i.e. the existence of a so-called dark state which represents coherent superposition among the ground-state Zeeman sublevels. Mathematically, the dark state is given with the condition $\hat{H}_I |\text{dark state}\rangle = 0$. For the scheme $F_g = 2 \rightarrow F_e = 1$ (see figure 1) there are two dark states, one among $|m_g = -1\rangle$ and $|m_g = +1\rangle$ Zeeman sublevels, thus induced by the Λ interacting scheme. The other dark state represents linear combination of other ground-state sublevels, being part of the M scheme. Due to the existence of these dark states, EIT resonances are closely related to the ground-state Zeeman sublevels and the coherences created between them. Formation of coherences, dark states and optical pumping processes for different CPT schemes among the Zeeman sublevels was analysed by Renzoni *et al* [18] for the sodium D1 line. The role of ground-state coherences in the NMOR effect was also discussed [19, 20]. Matsko *et al* [19] analysed ellipticity-dependent nonlinear magneto-optic rotation of elliptically polarized light propagating in a medium with atomic coherence. It was shown that this rotation can be described by means of Λ , M and higher-chain Λ schemes. Drampyan *et al* [20] presented a theoretical description based on the inverted Y model (combination of the Λ and ladder systems).

In figure 3 we compare behaviour of the pulse transmission and the rotation angle ϕ versus the magnetic field B with the behaviour of the ground-state coherence $\rho_{g-1,g1}$. We present results for three moments of the pulse propagation corresponding to different intensities of the pulse in the medium: during rising of the pulse intensity ((a) and (d)), when the pulse is at the maximum intensity ((b) and (e)) and during falling of the pulse intensity ((c) and (f)). More precisely, these three instances correspond to times $t = 40 \text{ μs}$, $t = 50 \text{ μs}$ and $t = 64 \text{ μs}$ of the linearly polarized Gaussian pulse presented in figure 2. Results presented in figures 3(a)–(c) show that evolution of both EIT and NMOR show various dependences on B while the pulse intensity varies. Both magnitude of the polarization rotation angle and the shape of its dependence on B is very sensitive on the pulse intensity in the medium. There are also significant differences of both EIT and NMOR depending on whether the pulse intensity is rising or falling. Results for the dependence of the NMOR on B in figure 3(c),

calculated for the time when the pulse is ‘leaving’ the medium, $t = 64 \text{ μs}$, show oscillatory behaviour of rotation angle ϕ , that can be related to the Ramsey effect. Polarization of atoms created at the peak of the pulse is probed during the weaker pulse intensity at the time when the pulse exits the medium [21, 22]. For the same moments of the pulse propagation, results for the behaviour of the ground-state coherence $\rho_{g-1,g1}$, presented in figures 3(d)–(f) reveal a close relation between transmission of the pulse and the real part of $\rho_{g-1,g1}$, and between the dispersive shape of the rotation angle and the imaginary part of $\rho_{g-1,g1}$.

To further confirm the relation between NMOR and ground-state coherences, in figure 4 we compare amplitudes (a) and widths (b) of the angle of rotation ϕ (green curves) and of the imaginary part of $\rho_{g-1,g1}$ (blue curves) as a function of the magnetic field B , for different times during the pulse propagates through the medium. Amplitudes and widths were obtained from dispersively shaped dependence on B (green and blue curves in figure 3) i.e. from their minimum ($B < 0$) and maximum ($B > 0$) values. The NMOR amplitude represents the difference between these two extreme values of the rotation angle, while the NMOR width is the difference between the corresponding values of the magnetic field. Widths and amplitudes of the magnetic field dependence of $\rho_{g-1,g1}$ are calculated in an analogous way. Results show that the transient behaviour of the amplitudes and widths of NMOR and the imaginary part of coherence $\rho_{g-1,g1}$ closely follow each other. Discrepancy between widths at the time when the pulse begins to enter the medium is due to the fact that formation of NMOR signal is slower than the coherence buildup.

Results presented in figure 4 reflect diversity of the magnetic field dependence of rotation angle $\phi(B)$ during pulse propagation through the medium of Rb atoms. During the rising of the pulse intensity, when the pulse starts to enter the medium, there is a linear-like dependence of the NMOR amplitude with increasing intensity. With rising of the pulse intensity, atoms are exposed to larger energy per unit surface area, as given with the integral of the pulse intensity over time i.e. the area of the pulse. Results presented in figure 4(a) show the effect of saturation at around $t = 43 \text{ μs}$, that is before the pulse peak intensity enters the medium. Further increase of the intensity leads to smaller amplitudes of $\phi(B)$ at the pulse peak intensity. Results in figure 4 show that, for times when pulse intensity is falling, the resonances are becoming steeper i.e. the width of $\phi(B)$ is decreasing and amplitude is becoming larger.

Next, we analyse the effect of the pulse peak intensity and width on the behaviour of NMOR. In figure 5(a) we present the amplitude of $\phi(B)$ versus time for three light pulses of the same width $\Delta_W = 10 \text{ μs}$, centred at $t_c = 50 \text{ μs}$ and with different peak intensities $I^0 = 0.1 \text{ mW cm}^{-2}$ (magenta curve), $I^0 = 0.5 \text{ mW cm}^{-2}$ (green curve) and $I^0 = 1 \text{ mW cm}^{-2}$ (black curve). In figure 5(b) the NMOR amplitude is presented for three pulses with peak intensity $I^0 = 0.3 \text{ mW cm}^{-2}$ and different widths, $\Delta_W = 10 \text{ μs}$ (magenta curve), $\Delta_W = 20 \text{ μs}$ (green curve) and $\Delta_W = 40 \text{ μs}$ (black curve). For results presented in figure 5(b), the pulses were centred at $t_c = 100 \text{ μs}$ to ensure that for $t = 0$ pulse intensity represents numerical zero.

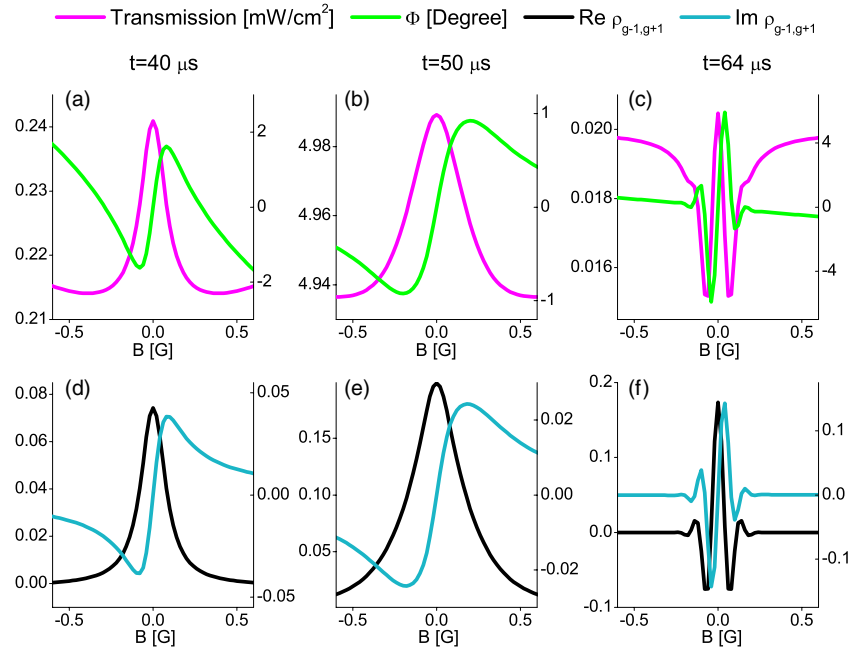


Figure 3. Results for the magnetic field dependence of transmission (magenta curves), rotation angle ϕ (green curves), real (black curves) and imaginary (blue curves) parts of the ground-state coherence $\rho_{g-1,g+1}$ for three different moments of the pulse propagation: $t = 40 \mu\text{s}$ ((a) and (d)), $t = 50 \mu\text{s}$ ((b) and (e)) and $t = 64 \mu\text{s}$ ((c) and (f)). Results are presented for the linearly polarized pulse with the peak intensity $I^0 = 5 \text{ mW cm}^{-2}$, $t_c = 50 \mu\text{s}$ and $\Delta_W = 10 \mu\text{s}$ shown in figure 2. y-scales for the rotation angle and the imaginary part of $\rho_{g-1,g+1}$ are given on the right sides.

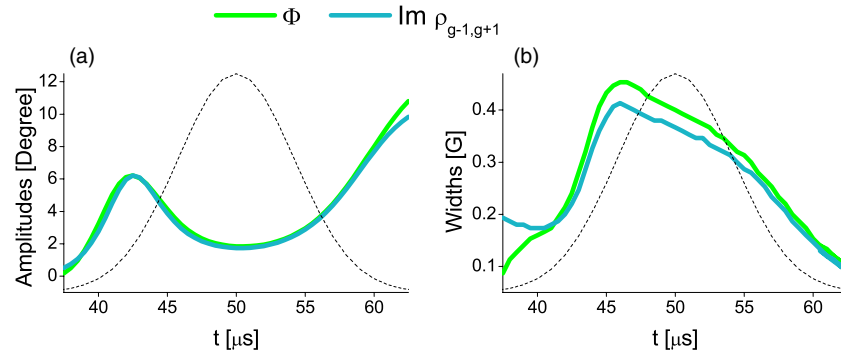


Figure 4. Results for amplitude (a) and width (b) of NMOR (green curves) and imaginary part of the ground-state coherence $\rho_{g-1,g+1}$ (blue curves) during the light pulse passing through the medium. Results for the amplitude of the imaginary part of coherence were multiplied by the constant to coincide with amplitudes of $\phi(B)$. Also presented with black dashed lines are normalized wave-forms of the pulse. Parameters are the same as in figure 3.

The effect of the pulse peak intensity and width on the NMOR has to be related to the light absorbed by the atomic medium since the beginning of the interaction of the atomic ensemble with the light pulses. Dependences of amplitudes with the time of the pulse propagation, presented in figure 5, show their increase when pulse intensity is rising. However, while the magenta curves in both figures 5(a) and (b) constantly increase even when the pulse is leaving the medium, the results for higher pulse peak intensities and larger pulse width show that there are critical moments when the amplitude of the $\phi(B)$ starts to decrease. This results in smaller polarization rotation although the pulse intensity is rising. Exposing the atoms to higher pulse energy, either by the increase of the pulse peak intensity or with wider Δ_W , leads to saturation and even decrease of NMOR amplitudes during high pulse intensities.

This effect is relaxed with the lower intensity when the pulse is leaving the medium, leading to even higher amplitudes than for pulse intensities during the rising side of the pulse. This kind of dependence of the NMOR amplitude with time is characteristic for much larger intensities, as presented in figure 4.

Our analysis shows that a decrease of polarization rotation, while pulse intensity is still increasing, is related to the optical pumping into the dark state. Here we analyse the dark state formed only by the Λ scheme, while the analysis of the other dark state (M -scheme) brings very similar results. In figure 6(a) we present results for the behaviour of the population of the dark state as a function of time for three values of the magnetic fields $B = 0$ (magenta curves), $B = 0.1 \text{ G}$ (green curves) and $B = 0.2 \text{ G}$ (black curves). Presented in figure 6(b) is the imaginary part of the

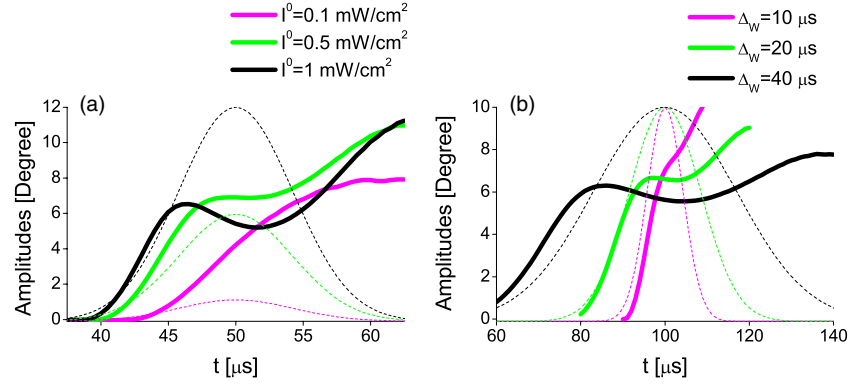


Figure 5. NMOR amplitudes at different times during the light pulse propagation through the medium. In (a) we present results for the pulse with $\Delta_W = 10 \mu\text{s}$, $t_c = 50 \mu\text{s}$ and for three different pulse peak intensities: $I^0 = 0.1 \text{ mW cm}^{-2}$ (magenta curve), $I^0 = 0.5 \text{ mW cm}^{-2}$ (green curve) and $I^0 = 1 \text{ mW cm}^{-2}$ (black curve). In (b) we present results for the pulse with $I^0 = 0.3 \text{ mW cm}^{-2}$, $t_c = 100 \mu\text{s}$ and for three different widths of the pulse: $\Delta_W = 10 \mu\text{s}$ (magenta curve), $\Delta_W = 20 \mu\text{s}$ (green curve) and $\Delta_W = 40 \mu\text{s}$ (black curve). Also presented with dashed lines of matching colours are the wave-forms of the corresponding light pulses.

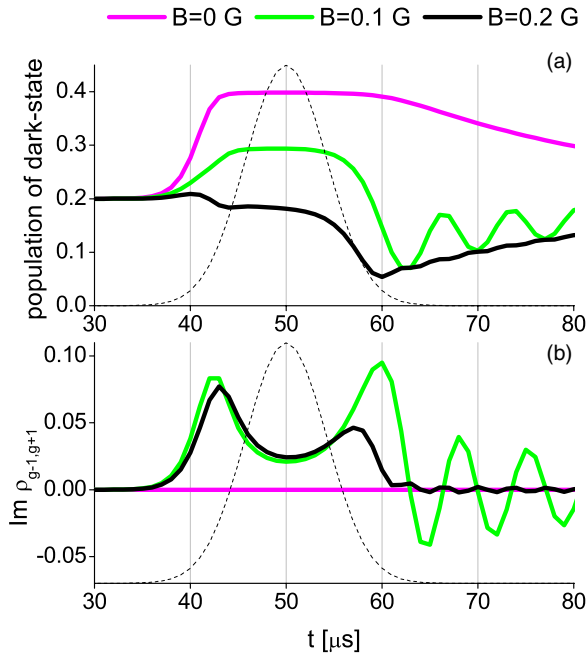


Figure 6. Time-dependence of the population of the Λ -scheme dark state (a) and imaginary part of the ground-state coherence $\rho_{g-1,g+1}$ (b) for three magnetic fields: $B = 0 \text{ G}$ (magenta curves), $B = 0.1 \text{ G}$ (green curves) and $B = 0.2 \text{ G}$ (black curves). Results are for the linearly polarized pulse presented in figure 2: $I^0 = 5 \text{ mW cm}^{-2}$, centred at $t_c = 50 \mu\text{s}$ and $\Delta_W = 10 \mu\text{s}$. Normalized wave-forms of the pulse are presented with black dashed lines.

coherence $\rho_{g-1,g+1}$, which constitutes the dark state from the Λ -scheme. Results are for the linearly polarized pulse presented in figure 2.

For the considered configuration, the condition for the dark state is satisfied only for the zero magnetic field, while for other magnetic fields, inside the EIT resonance, the EIT profile represents the ‘grey zone’ where the absorption is less suppressed. Results in figure 6(a) show that for $B = 0$ the population of the dark state is constantly trapped during most of the time of the pulse propagation, while the non-zero magnetic fields yield a less populated dark state. For non-zero

magnetic fields and times when the population of the dark state shows a flat dependence of maximally trapped atoms in the dark state, the magnitude of the imaginary part of the coherence $\rho_{g-1,g+1}$, decreases during the rising of the pulse intensity, and recovers after the pulse peak intensity. Maximally populated dark states lead to suppressed absorption which in turn leads to depolarization of atoms and less rotation. The decrease of $\phi(B)$ amplitudes during the pulse maximum intensity is the result of optical pumping into the dark states, followed by simultaneous decrease of coherences with time, but also dependent on the value of the magnetic field B .

The subject of many studies is the width of EIT [18, 23–26]. Being both related to the ground-state coherences, EIT and NMOR also depend on the lifetimes of ground-state coherences created between ground-state Zeeman sublevels. In our model, we have taken into account relaxation of all density matrix elements with rate γ , due to the finite time that atoms spend in the laser beam. While the lifetimes of excited state and optical coherences are limited by the spontaneous emission rates, the lifetime of the ground-states is much longer and is determined with γ .

In figure 7 we present dependences of the NMOR amplitude (a) and the NMOR width (b) on the time-dependent intensity of the linearly polarized laser pulse (shown in figure 2) for three values of relaxation rates: $\gamma = 0.0001 \Gamma$ (magenta curve), $\gamma = 0.001 \Gamma$ (green curve) and $\gamma = 0.01 \Gamma$ (black curve). The presented results show that the value of the relaxation rate $\gamma = 0.01 \Gamma$ (black curves in figure 7) yields qualitatively and quantitatively different behaviour of both NMOR amplitude and width, compared to the smaller relaxation rates. During rising of the pulse intensity, while the dark states are not yet populated, the influence of large γ means greater dissipation of the ground-state populations and the coherences and thus slower formation of the dark states. For times when saturation of NMOR is present, the rate of relaxation of the ground-states strongly influences the widths of the rotation angles. The width of $\phi(B)$ for $\gamma = 0.01 \Gamma$ (black curve in figure 7(b)) is significantly larger compared to the results with smaller γ . Also, the black curve in figure 7(a) shows a decrease of the amplitude when the pulse

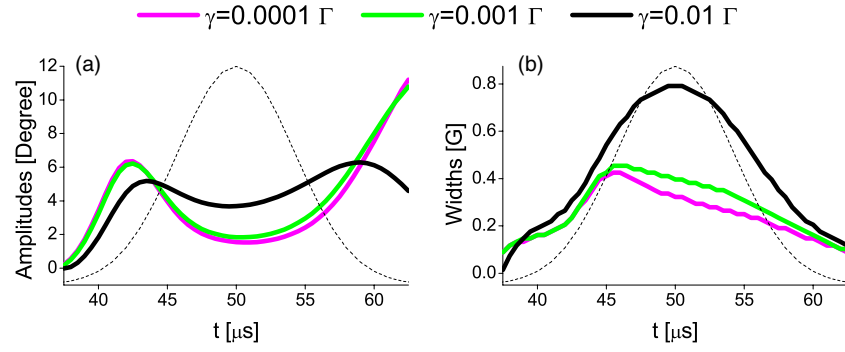


Figure 7. Time-dependence of the amplitude (a) and the width (b) of $\phi(B)$, for the ground-state relaxation rates: $\gamma = 0.0001 \Gamma$ (magenta curve), $\gamma = 0.001 \Gamma$ (green curve) and $\gamma = 0.01 \Gamma$ (black curve). Results are for the linearly polarized pulse and the peak intensity is $I^0 = 5 \text{ mW cm}^{-2}$, centred at $t_c = 50 \mu\text{s}$ and with the $\Delta_W = 10 \mu\text{s}$, presented in figure 2. Normalized wave-forms of the pulse are presented with black dashed lines.

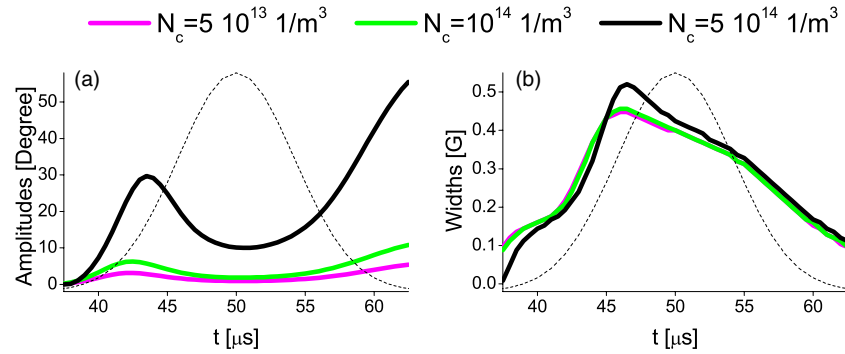


Figure 8. Dependence of the amplitude (a) and the width (b) of the $\phi(B)$ on the time of pulse propagation for three different concentrations of Rb atoms in the medium: $N_c = 5 \times 10^{13} \times 1 \text{ m}^{-3}$ (magenta curves), $N_c = 10^{14} \times 1 \text{ m}^{-3}$ (green curves) and $N_c = 5 \times 10^{14} \times 1 \text{ m}^{-3}$ (black curves). Results are presented for the linearly polarized pulse with the peak intensity $I^0 = 5 \text{ mW cm}^{-2}$, $t_c = 50 \mu\text{s}$ and $\Delta_W = 10 \mu\text{s}$ as shown in figure 2. Normalized pulse wave-forms are presented with black dashed lines.

is leaving the medium. During this period, intensities of the pulse are insufficient to sustain created coherences due to great dissipation with the rate $\gamma = 0.01 \Gamma$. Effect of decoherence on the NMOR was previously studied by Wang *et al* [27]. It was pointed out that an increase of decoherence rate leads to the behaviour typical for a linear Faraday rotator because the EIT effect tends to be eliminated. The shift of the peak of the Faraday rotation angle to higher magnetic fields was observed [27], which can be related to an increased width of $\phi(B)$ in our analysis for the case of pulsed light.

Results presented in figure 8 demonstrate the influence of the optical thickness of the atomic gas on the NMOR. We present results for the amplitude (a) and width (b) of the calculated $\phi(B)$ as a function of time-dependent laser intensity. Results are for the linearly polarized pulse presented in figure 2. Calculations were performed for three values of the atomic density $N_c = 5 \times 10^{13} \times 1 \text{ m}^{-3}$ (magenta curves), $N_c = 10^{14} \times 1 \text{ m}^{-3}$ (green curves) and $N_c = 5 \times 10^{14} \times 1 \text{ m}^{-3}$ (black curves). Results presented in figure 8 show that atomic density does not influence the width of NMOR significantly. Conversely, amplitudes are strongly affected with the change of atomic density yielding approximately an order of magnitude greater rotation when the concentration is changed by an order of magnitude. The effect of the atomic density in our theoretical model is in the macroscopic polarization of atomic medium (see equation (11)), which depends linearly

on the atomic concentration. Atomic concentration determines the number of polarized atoms whose atomic polarization is precessing in the magnetic field, and therefore changes the properties of the optical medium. The change of atomic density also strongly affects polarization of the pulse itself, since components of the atomic polarization are in the right-hand sides of equation (9) and represent source terms of the Maxwell–Bloch equations. The effect of atomic density on the nonlinear Faraday effect with intense linearly polarized light in an optically thick atomic rubidium vapour was previously studied by Hsu *et al* [28] for the CW field. They show that the polarization rotation rate, which is rotation angle per unit magnetic field $d\phi/dB$, in the limit of low field has a maximum value as the density is increased.

4. Conclusions

We analysed NMOR of the linearly polarized Gaussian pulse while propagating through the cold atomic gas. The frequency of the laser pulse is tuned to the $F_g = 2 \rightarrow F_e = 1$ transition in ^{87}Rb , D1 line, and the pulse induces EIT. Transient non-monotonic dependence of the rotation angle is obtained, with enhancement and suppression of magneto-optical rotation during different phases of the pulse propagation. Throughout the pulse propagation, NMOR (EIT) behaves similarly to the imaginary (real) part of the ground-state Zeeman coherences.

NMOR depends on optical pumping into the dark states and on the behaviour of ground-state coherences subjected to CPT. Behaviour of pulse NMOR qualitatively changes for different values of the pulse peak intensity. For the pulse with peak intensity of $I^0 = 5 \text{ mW cm}^{-2}$, the initial increase of the NMOR is followed by the decrease when the pulse intensity increases and nears its peak value. For pulses of much smaller peak intensity, the magnitude of NMOR increases all the time during the pulse propagation. It was shown that the relaxation of the ground-states affects the width of the dispersive-shaped magnetic field dependence of polarization rotation angle—the maximum of NMOR shifts to higher magnetic field as the relaxation increases. Our results have shown the effect of the density of Rb atoms, i.e., for the range of considered parameters, the magnitude of the NMOR scales nearly linearly with the concentration of atoms. Results presented in this paper are of interest in all studies of the propagation of a Gaussian pulse through the media under the conditions of EIT and in the presence of external magnetic field.

Acknowledgment

This work was supported by the Ministry of Education, Science and Technological Development of the Republic of Serbia, under grants number III 45016 and OI 171038.

References

- [1] Budker D, Gawlik W, Kimball D F, Rochester S M, Yashchuk V V and Weis A 2002 *Rev. Mod. Phys.* **74** 1153
- [2] Alexandrov E B, Auzinsh M, Budker D, Kimball D F, Rochester S M and Yashchuk V V 2005 *J. Opt. Soc. Am. B* **22** 7
- [3] Sautenkov V A, Lukin M D, Bednar C J, Novikova I, Mikhailov E, Fleischhauer M, Velichansky V L, Welch G R and Scully M O 2000 *Phys. Rev. A* **62** 023810
- [4] Akhmedzhanov R A and Zelensky I V 2002 *JETP Lett.* **76** 419
- [5] Pandey K, Wasan A and Natarajan V 2008 *J. Phys. B: At. Mol. Opt. Phys.* **41** 225503
- [6] Harris S E 1997 *Phys. Today* **50** 369
- [7] Fleischhauer M, Imamoglu A and Marangos J P 2005 *Rev. Mod. Phys.* **77** 633
- [8] Alzetta G, Gozzini A, Moi L and Orriols G 1976 *Nuovo Cimento B* **36** 5
- [9] Arimondo E 1996 *Prog. Opt.* **35** 257
- [10] Harris S E, Field J E and Kasapi A 1992 *Phys. Rev. A* **46** R29
- [11] Kasapi A, Jain M, Yin G Y and Harris S E 1995 *Phys. Rev. Lett.* **74** 2447
- [12] Lezama A, Akulshin A M, Sidorov A I and Hannafor P 2006 *Phys. Rev. A* **73** 033806
- [13] Wang K, Peng F and Yang G 2003 *J. Opt. B: Quantum Semiclass. Opt.* **5** 44
- [14] Qi Y, Niu Y, Zhou F, Peng Y and Gong S 2011 *J. Phys. B: At. Mol. Opt. Phys.* **44** 085502
- [15] Budker D, Kimball D F, Rochester S M and Yashchuk V V 1999 *Phys. Rev. Lett.* **83** 1767
- [16] Gao H, Rosenberry M, Wang J and Batelaan H 2005 *J. Phys. B: At. Mol. Opt. Phys.* **38** 1857
- [17] Ruseckas J, Juzelinis G, Ohberg P and Barnett S M 2007 *Phys. Rev. A* **76** 053822
- [18] Renzoni F, Maichen W, Windholz L and Arimondo E 1997 *Phys. Rev. A* **55** 3710
- [19] Matsko A B, Novikova I, Zubairy M S and Welch G R 2003 *Phys. Rev. A* **67** 043805
- [20] Drampyan R, Pustelny S and Gawlik W 2009 *Phys. Rev. A* **80** 033815
- [21] Krmpot A J, Ćuk S M, Nikolić S N, Radonjić M, Slavov D G and Jelenković B M 2009 *Opt. Express* **17** 22491
- [22] Ćuk S M, Radonjić M, Krmpot A J, Nikolić S N, Grujić Z D and Jelenković B M 2010 *Phys. Rev. A* **82** 063802
- [23] Ye C Y and Zibrov A S 2002 *Phys. Rev. A* **65** 023806
- [24] Figueroa E, Vewinger F, Appel J and Lvovsky A I 2006 *Opt. Lett.* **31** 2625
- [25] Strekalov D, Matsko A B and Maleki L 2005 *J. Opt. Soc. Am. B* **22** 65
- [26] Pack M V, Camacho R M and Howell J C 2007 *Phys. Rev. A* **76** 013801
- [27] Wang J 2010 *Phys. Rev. A* **81** 033841
- [28] Hsu P S, Patnaik A K and Welch George R 2008 *Phys. Rev. A* **78** 053817

On the efficiency of 1D atom localisation via EIT in a degenerate two-level atomic system

This content has been downloaded from IOPscience. Please scroll down to see the full text.

2016 Laser Phys. Lett. 13 045202

(<http://iopscience.iop.org/1612-202X/13/4/045202>)

View [the table of contents for this issue](#), or go to the [journal homepage](#) for more

Download details:

IP Address: 192.195.94.136

This content was downloaded on 31/03/2016 at 11:04

Please note that [terms and conditions apply](#).

On the efficiency of 1D atom localisation via EIT in a degenerate two-level atomic system

Jelena Dimitrijević, Dušan Arsenović and Branislav M Jelenković

Institute of Physics, University of Belgrade, Pregrevica 118 11080 Belgrade

E-mail: jelenad@ipb.ac.rs

Received 4 September 2015, revised 26 November 2015

Accepted for publication 26 January 2016

Published 4 March 2016



Abstract

We analyse one-dimensional (1D) subwavelength atom localisation in a cold atomic medium under the action of two optical fields, the standing-wave and travelling probe fields, in the presence of a magnetic field. Optical Bloch equations are solved numerically for the hyperfine atomic transition $F_g = 2 \rightarrow F_e = 1$ of the ^{87}Rb D1 line. All Zeeman sublevels are included in the calculations. This atomic scheme allows electromagnetically induced transparency (EIT) if the applied magnetic field is zero or small. The results for the position-dependent probe absorption are presented for two configurations, depending on the orientation of the magnetic field with respect to the optical fields' polarisations. The efficiency of the atom localisation is analysed for a large range of field intensities and applied magnetic fields. The observed behaviour of the probe absorption is analysed through the effects of EIT induced by two fields of various strengths and its dependence on the applied magnetic fields.

Keywords: 1D atom localisation, electromagnetically induced transparency, Zeeman effect

(Some figures may appear in colour only in the online journal)

1. Introduction

During the past two decades there has been considerable attention in developing various techniques for precision position measurements of an atom moving through a standing-wave field [1]. Due to the fact that the dynamics of the atomic systems is position dependent within a standing-wave, by measuring the position-dependent quantities of the system, one can attain information on the position of the atom in the subwavelength domain. Interest in studying the atom localisation effect lies in potential applications for the precise measurement of atom position in laser cooling and trapping of atoms [2, 3], Bose–Einstein condensation [4, 5], atom nanolithography [6–8], the measurement of the centre-of-mass wave function of moving atoms [9, 10] etc.

Early developed methods for atom localisation were based on measurements of the phase shifts of standing waves [11, 12], or atomic dipole [13, 14], resonance imaging methods [15, 16] entanglement between the atom position and its internal state [17], Ramsey interferometry [18] etc. Recent techniques to achieve atom localisation are mainly based on the atomic coherence of internal states and quantum-interference effects.

Considerable interest is in realising atom localisation by coherent population trapping [19] and electromagnetically induced transparency (EIT) [20], also phase-dependent EIT in closed-loop atomic schemes, Autler–Townes microscopy [21], STIRAP (stimulated Raman adiabatic passage) [22] etc. Studies were performed by utilising position-dependent quantities like probe field absorption [23, 24], atom excited state population [25–27], spontaneously emitted photon [21, 28–31] and Raman gain [32, 33].

While early studies on atom localisation were mainly for one-dimensional localisation, recent studies also analyse realisations of two-dimensional localisation [24, 30, 31], since they provide more information on the atom position, better spatial resolution and could potentially find more applications. Moreover, recent studies [34, 35] suggest the realisation of three-dimensional atom localisation. The newly established domain of subwavelength localisation, named sub-half-wavelength localisation, analyses techniques that give information on the atom position within the half wavelength distance [29, 36, 37]. Only a few experimental realisations of the atom localisation effect have been performed [34, 38–40] so far.

In studies of atom localisation, an atom is considered to be localised if narrow structures can be observed in the

localisation pattern, i.e. a position dependence of measurable quantity. The number of narrow structures in one sub-wavelength domain shows the detecting probability, the width shows the localisation precision, while the positions indicate where the atom is localised. Most theoretical studies on atom localisation use simple atomic schemes constituted of several atomic levels. This enables analytical expressions to be obtained from which one can read the choice of parameters (field strengths, detunings, relative phase etc) which yields the most efficient atom localisation.

We perform a numerical study and analyse the efficiency of one-dimensional (1D) atom localisation by using two orthogonal optical fields, the standing-wave and travelling probe fields. Atom localisation studies often use the detuning of the optical field from the resonance for control of localisation. Here, we assume that both fields are on the resonance of $F_g = 2 \rightarrow F_e = 1$ transition, D1 line in ^{87}Rb , while the shift of energy levels from the resonances is done by applying a magnetic field. This atomic scheme is known to support Zeeman EIT, a quantum phenomenon due to the coherent superposition of magnetic sublevels, manifested in the reduced absorption of the optical field if zero or a small magnetic field is applied. The numerical calculations are done by solving Optical Bloch equations for a multiple-level atomic scheme with all the Zeeman sublevels taken into consideration. Two configurations, with different orientations of magnetic field, along the standing-wave or along the probe field polarisation, are analysed. The advantage of numerical analysis is that we can apply arbitrary strengths of optical and magnetic fields. The optical fields' intensities range from 10^{-4} to 10^2 mW cm^{-2} , while magnetic fields range from 0 to 5 G. We analyse the behaviour of the localisation patterns obtained from the probe field absorption, investigating the effects of standing-wave and probe intensities, and also the influence of magnetic fields on the efficiency of 1D atom localisation.

2. 1D atom localisation schemes and theoretical model

We analyse a scheme with two optical fields, standing-wave and travelling probe fields interacting with cold atoms, in the presence of a magnetic field. Both fields are linearly polarised with mutually orthogonal polarisations and propagation directions. We analyse two configurations, i.e. the directions of the standing-wave and probe field polarisation with respect to the applied magnetic field:

- **Configuration A:** The optical standing-wave is linearly polarised along the magnetic field direction and aligned along the y-direction. The probe field is linearly polarised in the y-direction and propagates along the z-axis (see figure 1(a)).
- **Configuration B:** The probe field electric vector is collinear with the magnetic field, while the standing-wave is polarised in the y-direction and aligned along the x-axis (see figure 1(b)).

Steady-state optical Bloch equations (OBE) are solved for the $F_g = 2 \rightarrow F_e = 1$ transition (see figure 2) in ^{87}Rb , D1 line,

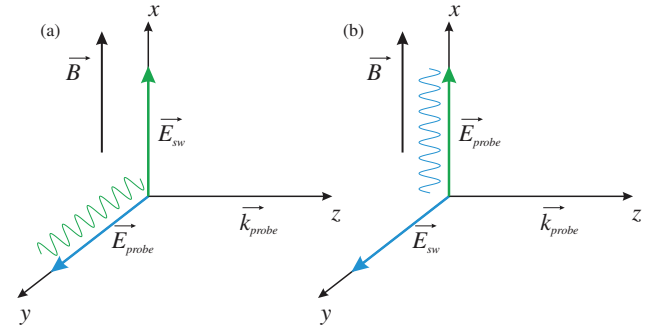


Figure 1. The geometry of the experiment, with applied magnetic field \vec{B} and two linearly polarised, mutually orthogonal optical fields, standing-wave and probe fields with electric vectors $\vec{E}_{\text{sw}}(\vec{r}, t)$ and $\vec{E}_{\text{probe}}(\vec{r}, t)$. \vec{k}_{probe} is the probe field wave-vector. (a) shows the configuration **A**: $\vec{E}_{\text{sw}} \parallel \vec{B} \perp \vec{E}_{\text{probe}}$; (b) is the scheme for configuration **B**: $\vec{E}_{\text{probe}} \parallel \vec{B} \perp \vec{E}_{\text{sw}}$, where we omit the dependence on t and \vec{r} .

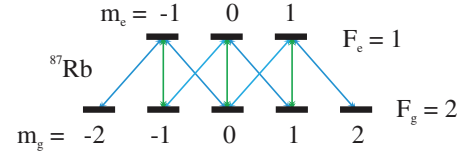


Figure 2. $F_g = 2$ and $F_e = 1$ hyperfine levels, with notation of magnetic sublevels and dipole allowed transitions due to selection rules $\Delta m = 0$ (green lines) and $\Delta m = \pm 1$ (blue lines).

for different applied magnetic fields and magnitudes of optical fields' intensities. From OBE:

$$\frac{i}{\hbar}[\hat{H}_0, \hat{\rho}] + \frac{i}{\hbar}[\hat{H}_I, \hat{\rho}] - \hat{S}\hat{\rho} + \gamma\hat{\rho} = \gamma\hat{\rho}_0, \quad (1)$$

we calculate the elements of density matrix $\hat{\rho}$. The diagonal elements of the density matrix, ρ_{g_i, g_i} and ρ_{e_i, e_i} are the populations, the elements ρ_{g_i, g_j} and ρ_{e_i, e_j} are the Zeeman coherences, and ρ_{g_i, e_j} and ρ_{e_i, g_j} are the optical coherences. Here, indexes g and e stand for the ground and the excited levels, respectively.

In equation (1), \hat{H}_0 is a Hamiltonian describing Rb atoms in magnetic field \vec{B} :

$$\hat{H}_0 = \sum_{i=1}^{2F_g+1} \hbar\omega_{g_i} |g_i\rangle\langle g_i| + \sum_{i=1}^{2F_e+1} \hbar\omega_{e_i} |e_i\rangle\langle e_i|. \quad (2)$$

The magnetic sublevels are split due to the Zeeman effect by $\mathcal{E}_{g_i} = \hbar\omega_{g_i} = \mathcal{E}_{F_g=2} + \mu_B l_{F_g} m_{g_i} B$ for ground-state sublevels and $\mathcal{E}_{e_i} = \hbar\omega_{e_i} = \mathcal{E}_{F_e=1} + \mu_B l_{F_e} m_{e_i} B$ for excited, where $m_{g(e)}$ are the magnetic quantum numbers of the ground and excited levels, μ_B is the Bohr magneton and $l_{F_{g(e)}}$ are Lande the gyromagnetic factors for the hyperfine levels. $\mathcal{E}_{F_g=2}$ and $\mathcal{E}_{F_e=1}$ are the energies of hyperfine levels $F_g = 2$ and $F_e = 1$ of the free atom, respectively.

The interaction of atoms with two optical fields is given with the Hamiltonian:

$$\hat{H}_I = -\hat{\vec{d}} \cdot \vec{E}(\vec{r}, t) = \sum_{i=1}^{2F_g+1} \sum_{j=1}^{2F_e+1} V_{g_i, e_j} |g_i\rangle\langle e_j| + \text{h.c.}, \quad (3)$$

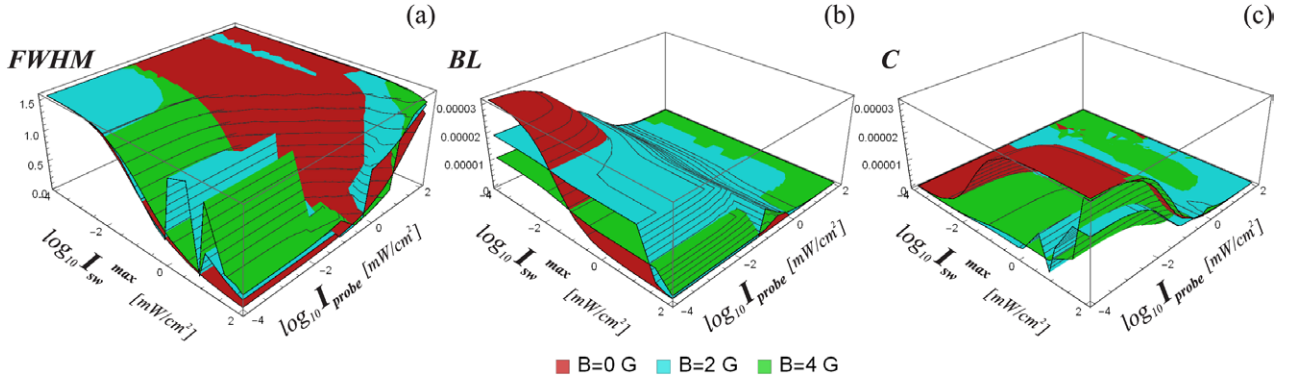


Figure 3. Results for configuration **A**: three-dimensional representation of the FWHM (a), base-level (b) and contrast (c) of the localisation pattern structures obtained from the probe absorption A_{probe} dependence on the normalised position $k_{\text{sw}}y$. The magnitudes of both optical field intensities take values from 10^{-4} to 10^2 mW cm^{-2} and are given on the logarithmic scale. Several surfaces correspond to several values of the magnetic field $B = 0, 2$ and 4 G .

where \hat{d} is the electric dipole operator and $\vec{E}(\vec{r}, t)$ is the total electric field oscillating with angular frequency $\omega_l = \frac{\mathcal{E}_{F_e=1} - \mathcal{E}_{F_g=2}}{\hbar}$, i.e. both fields are on the resonance of $F_g = 2 \rightarrow F_e = 1$ transition, the D1 line in ^{87}Rb . V_{g_i, e_j} are the matrix elements of the electric dipole interaction. $\hat{S}E$ stands for the spontaneous emission operator with rate Γ . We assume relaxation of all the density matrix elements with small rate $\gamma \ll \Gamma$ due to the mechanism like the finite time of flight or collisional decay [41]. The term $\gamma \hat{\rho}_0$ describes the repopulation of the atomic sample at the same rate, where ρ_0 describes atoms in their initial state, equal population of the ground Zeeman sublevels. As we are considering cold atomic sample, the role of Doppler broadening is not discussed.

We apply a Raman–Nath approximation [42], i.e. the centre-of-mass position of an atom along the direction of the standing-wave field is nearly constant and therefore we neglect the atom’s kinetic energy in the Hamiltonian. An electric dipole and rotating-wave approximations were applied. The quantisation axis is taken along magnetic field vector \vec{B} , and equations (1) are solved in the rotated coordinate system for all Zeeman sublevels of the $F_g = 2$ and $F_e = 1$ hyperfine levels.

With the quantisation axis along magnetic field vector, two configurations allow different dipole-allowed transitions between the Zeeman magnetic sublevels in the considered atomic scheme (see figure 2 and the indicated different colours). For the first configuration **A**, the standing-wave field is π -polarised and $\Delta m = 0$ transitions are allowed, while the linearly polarised probe field introduces multiple Λ -schemes with σ^+ and σ^- light components of equal strength. Conversely, for the configuration **B**, for the probe field the selection rule $\Delta m = 0$ stands, while for the standing-wave field the selection rules are $\Delta m = \pm 1$.

We calculate the probe absorption coefficient A_{probe} as an imaginary part of the complex susceptibility tensor diagonal elements. For the configuration **A**, with the probe field along the y-axis, the probe absorption is calculated from:

$$A_{\text{probe}} = \text{Im}(\chi_{\text{probe}}) = \text{Im}\left[\frac{ieRN_c}{6\sqrt{2}\epsilon_0 E_{\text{probe}}}(3\sqrt{2}\rho_{g_{-2}, e_{-1}} + 3\rho_{g_{-1}, e_0} + \sqrt{3}\rho_{g_0, e_{-1}} + \sqrt{3}\rho_{g_0, e_1} + 3\rho_{g_1, e_0} + 3\sqrt{2}\rho_{g_2, e_1})\right] \quad (4)$$

and for the configuration **B** and \vec{E}_{probe} along the x-axis is given as:

$$A_{\text{probe}} = \text{Im}(\chi_{\text{probe}}) = \text{Im}\left[\frac{eRN_c}{6\epsilon_0 E_{\text{probe}}} \times (3\rho_{e_{-1}, g_{-1}} + 2\sqrt{3}\rho_{e_0, g_0} + 3\rho_{e_1, g_1})\right], \quad (5)$$

where N_c is the atom concentration, e is the elementary charge, ϵ_0 is the permittivity of the vacuum and $R = \langle J_g || \vec{r} || J_e \rangle$ is the transition dipole matrix element.

3. Results and discussion

We calculate the localisation patterns, that is, the probe absorption versus the normalised positions ($k_{\text{sw}}x$ or $k_{\text{sw}}y$) within the standing-wave range $\{-\frac{\lambda}{2}, \frac{\lambda}{2}\}$. To calculate the localisation structures we use the same values of parameters for both configurations: the concentration of Rb atoms in the sample is $N_c = 10^{16} \frac{1}{\text{m}^3}$, the relaxation rate is $\gamma = 0.001 \Gamma$ and the spontaneous emission rate is $\Gamma = 2\pi 5.750 06 \text{ MHz}$. The results are analysed for the range of applied standing-wave and probe field intensities (I_{sw} and I_{probe} , respectively) from 10^{-4} to 10^2 mW cm^{-2} . We vary the magnetic field between 0 and 5 G, staying in the vicinity of the EIT resonance.

Besides obtaining narrow structures in the localisation pattern, important for an experimental realisation of atom localisation is the ability to resolve the absorption levels in the localisation pattern. Therefore, we analysed the behaviour of the base-level, contrast and also full width at half maximum (FWHM) of the narrow peaks shown in the localisation patterns. In order to determine the structures in the localisation pattern, we calculated extrema of the A_{probe} versus $k_{\text{sw}}x$ (or $k_{\text{sw}}y$) curve. The structure is defined by one of these extrema, as its middle point, and its two adjacent extrema. The base-level represents the minimal absorption of the structure and the contrast is taken between the central and border extrema, where we take the smaller value if the peak is asymmetric. The FWHM is calculated as the width of the peak at half of the contrast height.

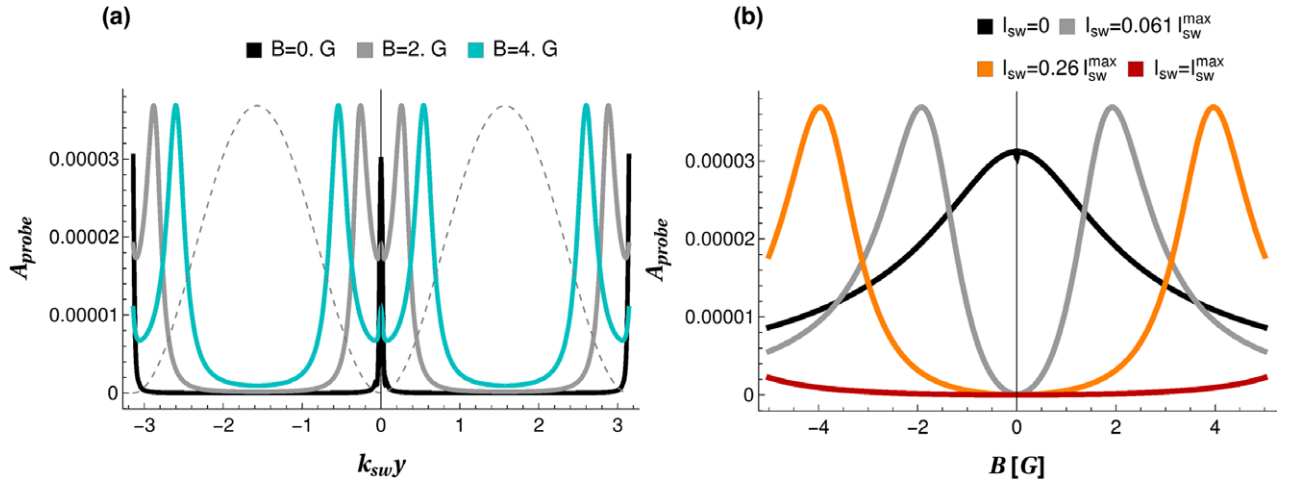


Figure 4. Configuration A: A_{probe} versus $k_{\text{sw}}y$ (a) and A_{probe} versus B (b) for fields' intensities $I_{\text{sw}}^{\text{max}} = 100 \text{ mW cm}^{-2}$ and $I_{\text{probe}} = 10^{-3} \text{ mW cm}^{-2}$. The results in (a) are for magnetic fields $B = 0, 2$ and 4 G and in (b) for standing-wave intensities $I_{\text{sw}} = 0, 0.061, 0.26$ and $1 I_{\text{sw}}^{\text{max}}$. The dashed line in (a) shows normalised standing-wave intensity $I_{\text{sw}} = I_{\text{sw}}^{\text{max}} \sin^2(k_{\text{sw}}y)$. The curves in (b) for $I_{\text{sw}} = 0.061$ and $0.26 I_{\text{sw}}^{\text{max}}$ correspond to the positions of four peaks in (a) for $B = 2$ and 4 G , respectively.

3.1. Configuration A

In configuration A, as shown in figure 1(a), standing-wave electric vector \vec{E}_{sw} is parallel to the magnetic field \vec{B} . In figure 3 we present the results for the FWHM (a), base-level (b) and contrast (c) of the localisation pattern structures for intensities, I_{probe} and $I_{\text{sw}}^{\text{max}}$, from 10^{-4} to 10^2 mW cm^{-2} given on the logarithmic scale. The results presented here are for three values of the magnetic field, $B = 0, 2$ and 4 G , while our analysis includes more values. The results for the widths of the structures show that, for $I_{\text{sw}}^{\text{max}} < 10^{-2} \text{ mW cm}^{-2}$, information on the atom position is available in a very broad region, i.e. the localisation structures have $\text{FWHM} \approx \frac{\lambda}{4}$, which indicates poor localisation precision. With the increase in $I_{\text{sw}}^{\text{max}}$ the widths reduce and for $I_{\text{probe}} < 1 \text{ mW cm}^{-2}$ extremely narrow structures can be obtained. The base level of the structures strongly depends on the probe field intensity and is low for $I_{\text{probe}} > 1 \text{ mW cm}^{-2}$. The contrast of the localisation structures is higher if $I_{\text{sw}}^{\text{max}}$ is large and I_{probe} is small. In the following, we present some results from the previously discussed range of intensities, which show efficient localisation and also the effects of the magnetic field on the atom localisation.

In figure 4 we present the results for the probe absorption versus normalised position (a) and versus magnetic field (b) for fields' intensities $I_{\text{sw}}^{\text{max}} = 100 \text{ mW cm}^{-2}$ and $I_{\text{probe}} = 10^{-3} \text{ mW cm}^{-2}$. The localisation pattern in figure 4(a) for $B = 0$ shows highly efficient localisation with two peaks within one wavelength of the standing-wave, at the nodes of the standing-wave. With the increase in the magnetic field, one peak at the node splits into two overlapped peaks, which reduces the detection probability by half. More importantly, the results for $B \neq 0$ show that for this range of intensities the magnetic field can be used to control the peak positions within the standing-wave, i.e. the increase in magnetic field uniformly shifts the positions of the four peaks from nodes towards the anti-nodes of the standing-wave.

The behaviour of the probe absorption within the standing-wave for different magnetic fields can be understood from the dependence of the Zeeman EIT profile on the applied standing-wave intensities. The results in figure 4(b) show the dependence of probe absorption on the magnetic field at several positions within the standing-wave. The splitting of the localisation peak for $B \neq 0$ (figure 4(a)) is due to two overlapping EIT profiles and higher values of the probe absorption away from the nodes, as shown in figure 4(b). The shift of the localisation peaks towards the anti-nodes, the with increase in magnetic field, can be attributed to EIT broadening. As depicted in figure 4(b), as $k_{\text{sw}}y$ approaches the anti-node, the amplitude of EIT remains nearly constant, while the width of EIT constantly increases with maximal absorption moving towards higher magnetic fields.

The effects of the stronger probe field are given in figure 5 for $I_{\text{sw}}^{\text{max}} = 100 \text{ mW cm}^{-2}$ and $I_{\text{probe}} = 0.5 \text{ mW cm}^{-2}$. In figure 5(a) we present A_{probe} versus $k_{\text{sw}}y$ for magnetic fields $B = 0, 0.04, 0.2$ and 1.8 G . The presented results suggest ways to control the localisation peaks' contrast by small magnetic fields. The localisation peaks are at the nodes of the standing-wave and the peaks' height gradually increases by about five times as the magnetic field changes from $B = 0$ to $B = 0.2 \text{ G}$. The observed increase in contrast is explained by the high-contrast of EIT for $I_{\text{sw}} = 0$ (shown in figure 5(b)). The contrast of the localisation peaks in figure 5(a) increases as long as the magnetic field is 'inside' the EIT transparency window ($B \leq 0.2 \text{ G}$), i.e. the increase of B weakens EIT, which leads to higher absorption at the nodes of the standing-wave.

A further increase in the magnetic field leads to broadening of the localisation peaks in figure 5(a), while the result for $B = 1.8 \text{ G}$ shows the formation of a much narrower peak on top of the wider peak. The results in figure 5(b) for $I_{\text{sw}} > 0$ show a similar effect to the results in figure 4(b), i.e. the EIT amplitudes are at the same level and the width of the EIT peak

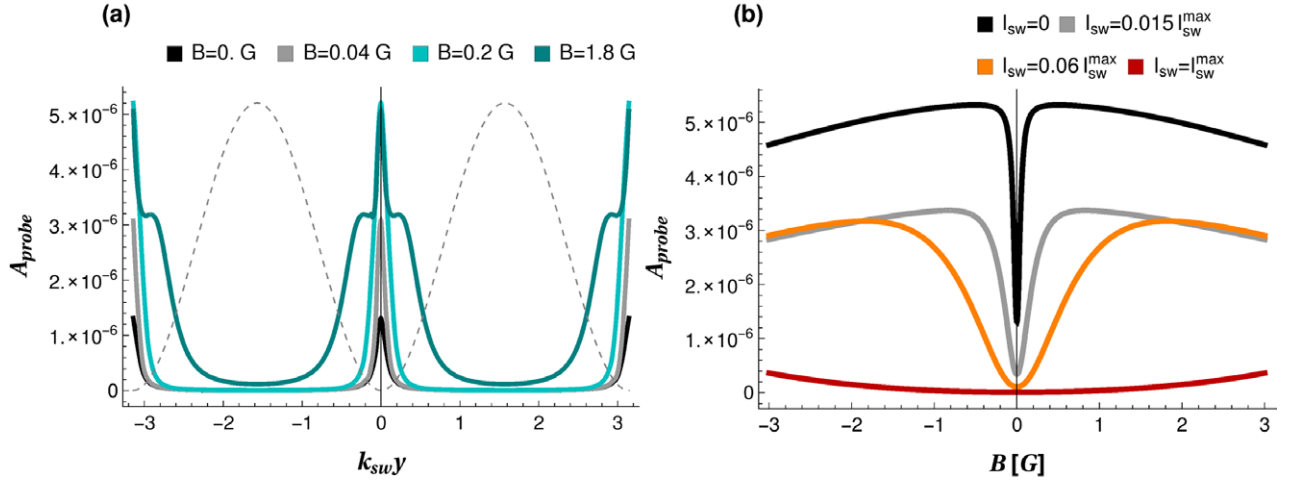


Figure 5. Configuration A: A_{probe} versus $k_{\text{sw}} y$ (a) and A_{probe} versus B (b) for fields' intensities $I_{\text{sw}}^{\text{max}} = 100 \text{ mW cm}^{-2}$ and $I_{\text{probe}} = 0.5 \text{ mW cm}^{-2}$. The results in (a) are for magnetic fields $B = 0, 0.04, 0.2$ and 1.8 G and in (b) for standing-wave intensities $I_{\text{sw}} = 0, 0.015, 0.06$ and $I_{\text{sw}}^{\text{max}}$.

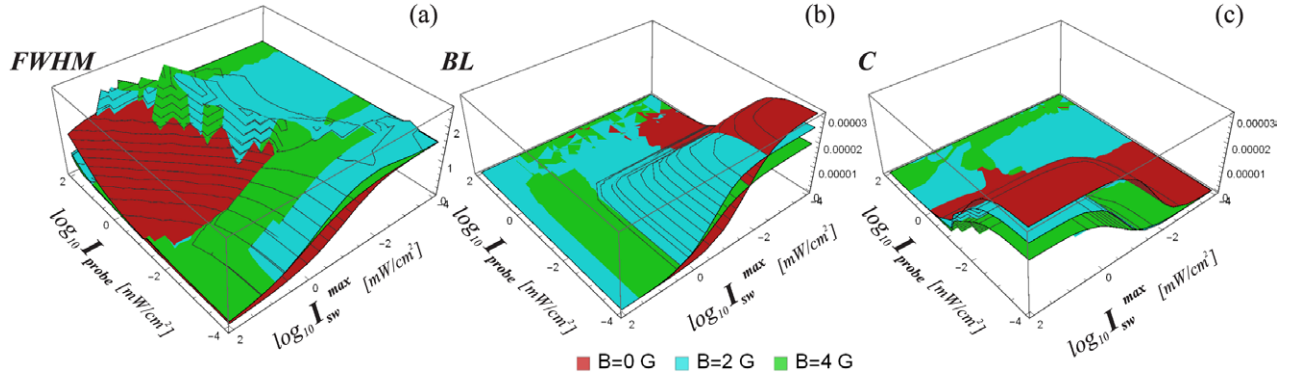


Figure 6. Results for configuration B: FWHM (a), base-level (b) and contrast (c) of the localisation patterns. The surfaces are drawn for 3 values of the magnetic fields $B = 0, 2$ and 4 G, while the maximal standing wave and probe field intensities are from 10^{-4} to 10^2 mW cm^{-2} .

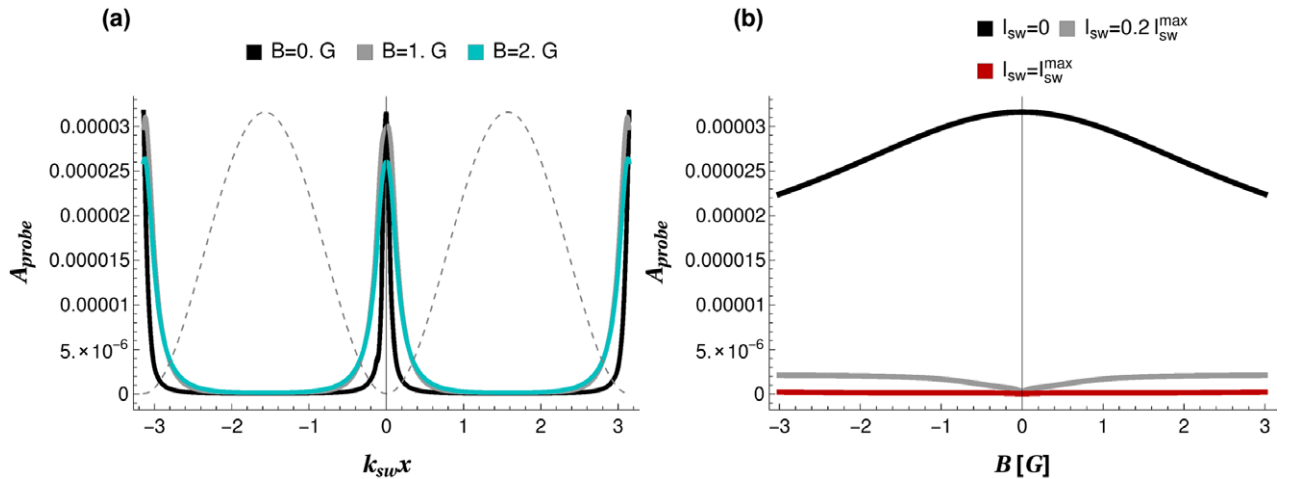


Figure 7. Configuration B: A_{probe} versus $k_{\text{sw}} x$ (a) and A_{probe} versus B (b) for fields' intensities $I_{\text{probe}} = 10^{-4} \text{ mW cm}^{-2}$ and $I_{\text{sw}}^{\text{max}} = 10 \text{ mW cm}^{-2}$. The results in (a) are for magnetic fields $B = 0, 1$ and 2 G and in (b) for standing-wave intensities $I_{\text{sw}} = 0, 0.2$ and $I_{\text{sw}}^{\text{max}}$. The dashed line in (a) shows the normalised standing-wave intensity $I_{\text{sw}} = I_{\text{sw}}^{\text{max}} \sin^2(k_{\text{sw}} x)$.

increases with the standing-wave intensity. For a small range of standing-wave intensities, the dependence of A_{probe} versus B shows overlapping for values of B outside of the EIT

peaks indicating that the standing-wave intensity reached saturation intensity [43], i.e. a further increase in I_{sw} does not lead to higher one-photon absorption. The above explains the

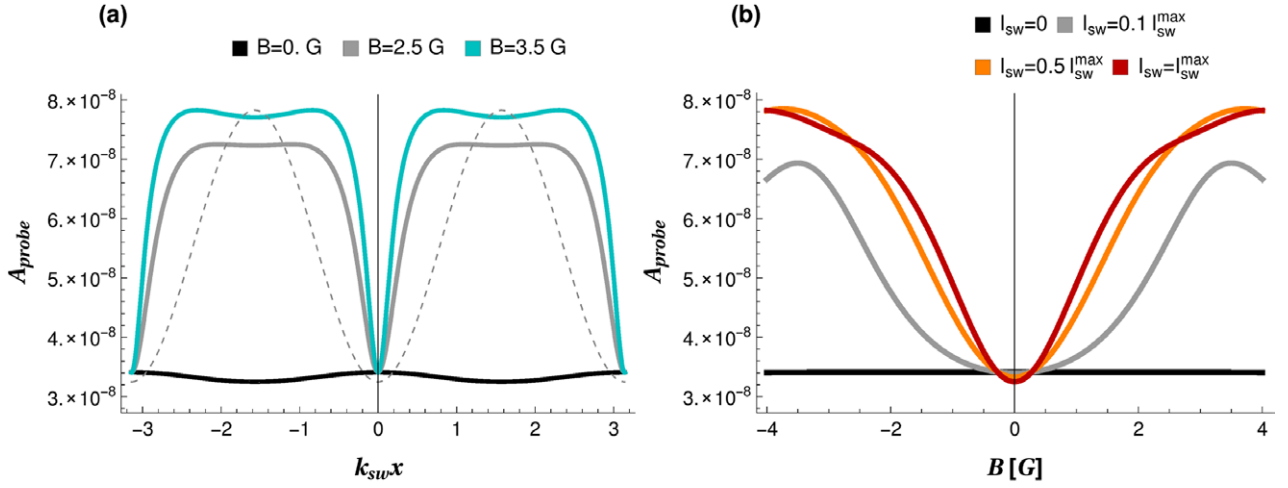


Figure 8. Configuration B: A_{probe} versus $k_{\text{sw}}x$ (a) and A_{probe} versus B (b) for fields' intensities $I_{\text{probe}} = 20 \text{ mW cm}^{-2}$ and $I_{\text{sw}}^{\text{max}} = 1 \text{ mW cm}^{-2}$. The results in (a) are for magnetic fields $B = 0, 2.5$ and 3.5 G and in (b) for standing-wave intensities $I_{\text{sw}} = 0, 0.1, 0.5$ and $1 I_{\text{sw}}^{\text{max}}$.

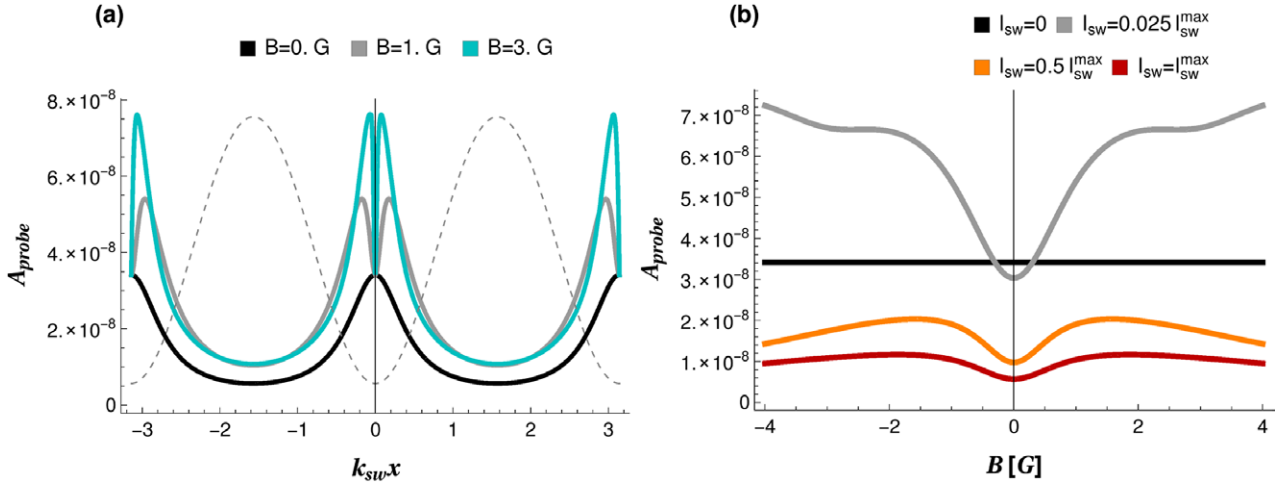


Figure 9. Configuration B: A_{probe} versus $k_{\text{sw}}x$ (a) and A_{probe} versus B (b) for fields' intensities $I_{\text{probe}} = 20 \text{ mW cm}^{-2}$ and $I_{\text{sw}}^{\text{max}} = 100 \text{ mW cm}^{-2}$. Results in (a) are for magnetic fields $B = 0, 1$ and 3 G and in (b) for standing-wave intensities $I_{\text{sw}} = 0, 0.025, 0.5$ and $1 I_{\text{sw}}^{\text{max}}$.

nearly constant probe absorption around the nodes for value $B = 1.8 \text{ G}$ in figure 5(a) and the formation of another narrow peak.

3.2. Configuration B

In configuration B, as presented in figure 1(b), the probe field is oriented along the magnetic field and the quantisation axis. Figure 6 shows the results for the FWHMs (a), base-contrast (b) and contrast (c) of the localisation pattern structures. The results for the structure widths show that the precision for atom localisation increases when intensity $I_{\text{sw}}^{\text{max}} \geq 10^{-2} \text{ mW cm}^{-2}$. The base-level of the localisation structures is low if either the field intensity is larger than 1 mW cm^{-2} . The results for the contrast suggest that the range $I_{\text{probe}} < 1 \text{ mW cm}^{-2}$ and $I_{\text{sw}}^{\text{max}} > 10^{-2} \text{ mW cm}^{-2}$ induces a higher contrast of localisation structures. In short, the results in figure 6 show good localisation with high precision, low base-level and high contrast for small I_{probe} and large $I_{\text{sw}}^{\text{max}}$.

In figure 7(a) we present the localisation patterns for $I_{\text{probe}} = 10^{-4} \text{ mW cm}^{-2}$ and $I_{\text{sw}}^{\text{max}} = 10 \text{ mW cm}^{-2}$ and for three values of the magnetic field $B = 0, 1$ and 2 G . The results show excellent atom localisation at the nodes of the standing-wave. At and around the anti-nodes positions' absorption is completely suppressed due to high standing-wave intensities exceeding the saturation intensity. The wide absorption maximum for $I_{\text{sw}} = 0$ in figure 7(b) corresponds to one-photon absorption since π -polarised light cannot induce EIT [41, 44]. The height of their localisation peaks in figure 7(a) at the nodes decreases slightly with the increase in B due to the shifts of magnetic levels and lower absorption due to detuning from the resonance. The localisation peaks are broadened for small values of I_{sw} or near the nodes, where EIT is weaker for larger B (see figure 7(b)) resulting in a slight reduction in localisation efficiency.

Figure 8 shows the results when the probe field intensity is higher than the standing-wave intensities, i.e. for $I_{\text{probe}} = 20 \text{ mW cm}^{-2}$ and $I_{\text{sw}}^{\text{max}} = 1 \text{ mW cm}^{-2}$. The results in figure 8(a)

show that for $B = 0$ the localisation pattern represents a sinusoidal curve with poor localisation precision. The results presented here and for similar intensities indicate that an increase in magnetic field can improve localisation due to a significant increase in the structure's contrast. At the nodes of the standing-wave, about 80% of the population is optically pumped to the edge levels, g_{-1} and g_{+1} by the π -polarised probe field's. The standing-wave field allows $\Delta m = \pm 1$ transitions too, which causes redistribution among the Zeeman sublevels and allows an increase in absorption at the positions between the nodes.

In figure 9 we present the results for a much stronger standing-wave field, $I_{\text{probe}} = 20 \text{ mW cm}^{-2}$ and $I_{\text{sw}}^{\text{max}} = 100 \text{ mW cm}^{-2}$. As shown in figure 8(a), the peaks in the localisation pattern for $B = 0$ are very wide. The increase in magnetic field also leads to the formation of narrow dips at the nodes' position, but a much stronger standing-wave creates four localisation peaks near the nodes. Compared to the results in figure 8 probe absorption at the anti-nodes' positions is at a lower level (see figure 9(b)) due to a considerably stronger standing-wave field which exceeds saturation intensity. The result when the peak splits if the magnetic field is applied is similar to the results in figure 4(a), although the presence of a magnetic field here significantly improves localisation due to better detection precision and the increase in the peaks' contrast.

4. Conclusion

We studied the efficiency of 1D subwavelength atom localisation via the EIT phenomenon in a degenerate two-level system, by using two orthogonal optical fields and small magnetic fields. The localisation efficiency is analysed for two configurations, when the applied magnetic field is along the standing-wave or along the probe field polarisation. Two configurations enable different transitions between the Zeeman magnetic sublevels, the behaviour of the EIT and consequently the localisation patterns. The properties of the position-dependent probe absorption are studied for a large range of field intensities and different values of magnetic field. The range of intensities giving efficient subwavelength resolution localisation was obtained numerically by calculating the widths and contrasts of the narrow structures shown in the localisation patterns.

Our results show that both configurations can be used for obtaining narrow localisation structures with widths less than 0.5λ . The results for configuration A reveal conditions where one can manipulate both the position and contrast of the localisation peaks by a small magnetic fields. If a strong standing-wave and weak probe field are applied, the results for configuration B show very efficient atom localisation for a large range of applied magnetic fields. The results for configuration B also indicate a range of optical field intensities when a magnetic field can be used to improve localisation. The behaviour of the position-dependent probe absorption is analysed through the mutual effects of the induced EIT, two optical fields of various strengths, below or above saturation, and the dependence on the applied magnetic field.

Acknowledgments

This work was supported by the Ministry of Education, Science and Technological Development of the Republic of Serbia, under grants III 45016 and OI 171038.

References

- [1] Kapale K T 2013 *Progress in Optics* vol 58, ed E Wolf (Amsterdam: Elsevier) chapter 4, p 200
- [2] Metcalf H and Van der straten P 1994 *Phys. Rep.* **244** 203
- [3] Phillips W D 1998 *Rev. Mod. Phys.* **70** 721
- [4] Collins G P 1996 *Phys. Today* **49** 18–21
- [5] Wu Y and Cote R 2002 *Phys. Rev. A* **65** 053603
- [6] Jin L, Sun H, Niu Y, Jin S and Gong S 2009 *J. Mod. Opt.* **56** 805
- [7] Johnson K S, Thywissen J H, Dekker N H, Berggren K K, Chu A P, Younkin R and Prentiss M 1998 *Science* **280** 1583
- [8] Boto A N, Kok P, Abrams D S, Braunstein S L, Williams C P and Dowling J P 2000 *Phys. Rev. Lett.* **85** 2733
- [9] Evers J, Qamar S and Zubairy M S 2007 *Phys. Rev. A* **75** 053809
- [10] Kapale K T, Qamar S and Zubairy M S 2003 *Phys. Rev. A* **67** 023805
- [11] Quadt R, Collett M and Walls D F 1995 *Phys. Rev. Lett.* **74** 351
- [12] Storey P, Collett M and Walls D 1992 *Phys. Rev. Lett.* **68** 472
- [13] Kunze S, Rempe G and Wilkens M 1994 *Europhys. Lett.* **27** 115
- [14] Brune M, Harlache M, Lefevre V, Maimond J M and Zagury N 1990 *Phys. Rev. Lett.* **65** 976
- [15] Thomas J E and Wang L J 1995 *Phys. Rep.* **262** 311
- [16] Rudy P, Eijnisman R and Bigelow N P 1997 *Phys. Rev. Lett.* **78** 4906
- [17] Kunze S, Dieckmann K and Rempe G 1997 *Phys. Rev. Lett.* **78** 2038
- [18] Kien F L, Rempe G, Schleich W P and Zubairy M S 1997 *Phys. Rev. A* **56** 2972
- [19] Arimondo E 1996 *Progress in Optics* vol 35, ed E Wolf (Amsterdam: Elsevier) chapter 5, p 257
- [20] Harris S E 1997 *Phys. Today* **50** 36
- [21] Qamar S, Zhu S Y and Zubairy M S 2000 *Phys. Rev. A* **61** 063806
- [22] Mompert J, Ahufinger V, Birkel G 2009 *Phys. Rev. A* **79** 053638
- [23] Sahrai M, Tajalli H, Kapale K T and Zubairy M S 2005 *Phys. Rev. A* **72** 013820
- [24] Ding C, Li J, Yang X, Zheng D and Xiong H 2011 *Phys. Rev. A* **84** 043840
- [25] Paspalakis E, Terzis A F and Knight P L 2005 *J. Mod. Opt.* **52** 1685
- [26] Liu C P, Gong S Q, Cheng D C, Fan X J and Xu Z Z 2006 *Phys. Rev. A* **73** 025801
- [27] Cheng D C, Niu Y P and Gong S Q 2006 *J. Opt. Soc. Am. B* **23** 2180
- [28] Ghafoor F, Qamar S and Zubairy M S 2002 *Phys. Rev. A* **65** 043819
- [29] Xu J and Hu X M 2007 *Phys. Lett. A* **366** 276
- [30] Wan R G, Kou J, Jiang L, Jiang Y and Gao J Y 2011 *J. Opt. Soc. Am. B* **28** 10
- [31] Wang Z and Yu B 2014 *Laser Phys.* **24** 045203
- [32] Qamar S, Mehmood A and Qamar S 2009 *Phys. Rev. A* **79** 033848
- [33] Rahmatullah, Wahab A and Qamar S 2014 *Laser Phys. Lett.* **11** 045202
- [34] Jendrzejewski F, Bernard A, Miller K, Cheinet P, Josse V, Piraud M, Pezz L, Sanchez-Palencia L, Aspect A and Bouyer P 2012 *Nat. Phys.* **8** 398

- [35] Qi Y, Zhou F, Huang T, Niu Y and Gong S 2012 *J. Mod Opt.* **59** 1092
- [36] Shen W B, Hu X M and Xu J 2008 *J. Phys. B: At. Mol. Opt. Phys.* **41** 185502
- [37] Shui T, Wang Z, Cao Z and Yu B 2014 *Laser Phys.* **24** 055202
- [38] Li H, Sautenkov V A, Kash M M, Sokolov A V, Welch G R, Rostovtsev Y V, Zubairy M S and Scully M O 2008 *Phys. Rev. A* **78** 013803
- [39] Proite N A, Simmons Z J and Yavuz D D 2011 *Phys. Rev. A* **83** 041803
- [40] Miles J A, Simmons Z J and Yavuz D D 2013 *Phys. Rev. X* **3** 031014
- [41] Margalit L, Rosenbluh M and Wilson-Gordon A D 2013 *Phys. Rev. A* **87** 033808
- [42] Meystre P and Sargent M III 1999 *Elements of Quantum Optics* 3rd edn (Berlin: Springer)
- [43] Steck D A 2015 Rubidium 87 D Line Data, available online at <http://steck.us/alkalidata> (revision 2.1.5, 13 January 2015)
- [44] Dimitrijević J, Krmpot A, Mijailović M, Arsenović D, Panić B, Grujić Z and Jelenković B M 2008 *Phys. Rev. A* **77** 013814

PAPER

Conservation laws for optical Bloch equations for the Λ scheme

To cite this article: Jelena Dimitrijevi *et al* 2020 *J. Phys. A: Math. Theor.* **53** 445201

View the [article online](#) for updates and enhancements.



IOP | ebooks™

Bringing together innovative digital publishing with leading authors from the global scientific community.

Start exploring the collection—download the first chapter of every title for free.

Conservation laws for optical Bloch equations for the Λ scheme

Jelena Dimitrijević^{*} , Dušan Arsenović and Branislav M Jelenković

Institute of Physics Belgrade, University of Belgrade, Pregrevica 118, 11080
Belgrade, Serbia

E-mail: jelenad@ipb.ac.rs

Received 29 April 2020, revised 7 August 2020

Accepted for publication 25 August 2020

Published 9 October 2020



Abstract

Results are presented for the conservation laws (CLs) for the optical Bloch equations (OBEs) for the Λ scheme under action of two light fields. The method of multipliers (variational derivative method) is used to obtain CLs which are dependent on the density-matrix elements. Results are classified and discussed by the phenomenological parameters and processes characteristic for OBEs, like the relaxation and decoherence, and the detunings of light fields. CLs for the Liouville von Neumann equation, as a special case of OBEs, without relaxation and decoherence terms, are presented and it is shown that traces, characteristic polynomials and their coefficients, eigen-values and determinants of class of matrices represent CLs. We also presented method, which used CLs obtained by the method of multipliers, to construct another set of CLs, which have the explicit time dependence and are valid for the larger set of parameters, with relaxation due to time of flight and spontaneous emission. Presented results could yield better understanding of the processes in the Λ scheme modeled by the OBEs, and as well have practical applications in various solution methods.

Keywords: conservation laws, optical Bloch equations, method of multipliers

(Some figures may appear in colour only in the online journal)

1. Introduction

Optical Bloch equations (OBEs) [1, 2] are widely used to describe the time evolution of the optically resonant dynamics of an ensemble of discrete-energy systems, those in atoms, molecules, semiconductor hetero-structures, molecular magnets etc. They model semiclassical case of a quantized physical system interacting with a classical optical fields, as given by the density matrix formalism for the mixed state. OBEs are ordinary differential equations over time of the first order. So far, OBEs have shown plentiful of applications in laser physics, spectroscopy, quantum and nonlinear optics.

^{*} Author to whom any correspondence should be addressed.

The Λ scheme represents the light–matter interacting scheme with three levels, two ground levels coupled to same excited level by the excitation fields. It has been exhaustively studied in quantum optics, for studying phenomena like electromagnetically induced transparency [3, 4] and coherent population trapping [5, 6]. Both phenomena can be considered to be the consequence of so called ‘dark-state’, developed as coherent superposition of the ground-state levels, non-interacting with the light fields [7].

Conservation laws (CLs) represent intrinsic properties of differential equations. They are quantities, we indicate as T , satisfying divergence condition $\nabla T \equiv 0$, on the solution of equation or the system of differential equations. CLs may not have physical interpretation, but are important for the practical applications in the mathematical physics and for better understanding processes that are described by the equations. For example, CLs can be used to control numerical errors in the numerical integration of various differential equations [8]. Knowledge of CLs can also be useful as a tool to develop new techniques for the solutions of some differential equations [9]. Various approaches [10, 11] have been developed to obtain CLs, like direct [12], Noether theorem [13], symmetry [14, 15] or multipliers [16].

CLs for the Λ scheme (or arbitrary scheme with N discrete levels) have been studied previously for a special case of OBEs without relaxation and decoherence terms, that is, Liouville von Neumann equation for density matrix. So-called pseudospin vector model enabled Hioe and Eberly [17, 18], Hioe [19] and Gottlieb [20, 21] to identify constants of motion for the scheme with N -levels. General expressions for the CLs for the N -level system, expressed in terms of traces of matrix products of density matrix and Hamiltonian, were given by Hioe [22]. Ravishankar [23] has found even more CLs of this type. Mallesh and Ramachandran [24] have found alternative way to express a set of equivalent CLs and to prove that the number of functionally independent among them equals $N^2 - N + 1$, when interacting with $N - 1$ optical fields.

In this paper, we present results for CLs for the OBEs for the Λ scheme. The first set of results are CLs which depend only on the density matrix elements and obtained by using the variational derivative method of multipliers [10, 25, 26]. We imposed ansatz for the multipliers in the form of quadratic polynomial of the density matrix elements. Obtained results for the non-trivial and functionally independent CLs are classified by the various phenomenological parameters used in OBEs. These results were further used to develop method to obtain another set of CLs. This set of CLs have explicit time-dependence and is valid with the relaxation due to time of flight and/or the spontaneous emission in OBEs.

We show that when frequencies of light fields, coupling two transitions in the Λ scheme, are at the resonance frequencies, Liouville von Neumann equation for density matrix has one more additional CL, compared to the number given by Mallesh and Ramachandran [24]. We represent set of functionally independent CLs for Liouville von Neumann equation for Λ scheme, by using trace of matrix product containing higher derivatives of density matrix. In addition, we analyzed CLs for the Liouville von Neumann equation for arbitrary N -level scheme. We introduced class of matrix quantities given as arbitrary product of density matrix and the interaction Hamiltonian under the rotating-wave approximation, and have shown that traces, determinants, eigen-values, coefficients in the characteristic polynomials of these quantities are all CLs.

2. Optical Bloch equations

We construct CLs of the OBEs for the Λ scheme (see figure 1), consisting of three energy levels, two ground levels, 1 and 2, and one excited level, 3. We consider ensemble of quantum systems interacting with two optical fields, the probe E_p which drives transition $1 \leftrightarrow 3$ and the control field E_c for $2 \leftrightarrow 3$ transition, with light frequencies ω_p and ω_c respectively, and

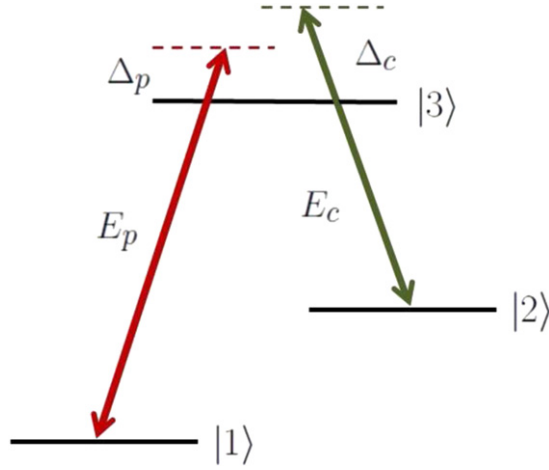


Figure 1. A scheme with three discrete energy levels in the Dirac notation and two light fields E_p and E_c with their detunings from the resonance frequencies, Δ_p and Δ_c .

corresponding detunings of two fields:

$$\begin{aligned}\Delta_p &= \omega_3 - \omega_1 + \omega_p, \\ \Delta_c &= \omega_3 - \omega_2 + \omega_c,\end{aligned}\tag{1}$$

where $\hbar\omega_i$ ($i = 1, 2, 3$) are energies of three levels. The total electric field is given with:

$$E = E_p e^{-i\omega_p t} + E_c e^{-i\omega_c t} + \text{c.c.},\tag{2}$$

where E_p and E_c are time-independent amplitudes of two fields.

OBEs are equations for the solution of the time-dependent density matrix elements $\rho_{ij}(t)$, where $\rho_{ii}(t)$ are populations of the ground ($i = 1, 2$) and excited ($i = 3$) states. $\rho_{ij}(t)$, for $i \neq j$, are ground-state and optical coherences. In the following text, we will write density matrix elements and other time-dependent quantities without explicit time-dependence. Considering various cases of OBEs that can be found in the literature, we present here equations that we used in their explicit form:

$$\begin{aligned}\frac{\partial \rho_{1,1}}{\partial t} &= i\rho_{3,1}\Omega_p^* - i\rho_{1,3}\Omega_p + \Gamma_1\rho_{3,3} + \frac{\gamma}{2} - \gamma\rho_{1,1} \\ \frac{\partial \rho_{1,2}}{\partial t} &= i\rho_{3,2}\Omega_p^* - i\rho_{1,3}\Omega_c + i(\Delta_c - \Delta_p)\rho_{1,2} - \gamma\rho_{1,2} \\ \frac{\partial \rho_{1,3}}{\partial t} &= -i\rho_{1,2}\Omega_c^* - i\rho_{1,1}\Omega_p^* + i\rho_{3,3}\Omega_p^* - i\Delta_p\rho_{1,3} - \frac{1}{2}(\Gamma_1 + \Gamma_2)\rho_{1,3} - \gamma_1\rho_{1,3} - \gamma\rho_{1,3} \\ \rho_{2,1} &= \rho_{1,2}^* \\ \frac{\partial \rho_{2,2}}{\partial t} &= i\rho_{3,2}\Omega_c^* - i\rho_{2,3}\Omega_c + \Gamma_2\rho_{3,3} + \frac{\gamma}{2} - \gamma\rho_{2,2} \\ \frac{\partial \rho_{2,3}}{\partial t} &= -i\rho_{2,2}\Omega_c^* + i\rho_{3,3}\Omega_c^* - i\rho_{2,1}\Omega_p^* - i\Delta_c\rho_{2,3} - \frac{1}{2}(\Gamma_1 + \Gamma_2)\rho_{2,3} - \gamma_2\rho_{2,3} - \gamma\rho_{2,3} \\ \rho_{3,1} &= \rho_{1,3}^*\end{aligned}$$

$$\rho_{3,2} = \rho_{2,3}^*$$

$$\frac{\partial \rho_{3,3}}{\partial t} = -i\rho_{3,2}\Omega_c^* + i\rho_{2,3}\Omega_c - i\rho_{3,1}\Omega_p^* + i\rho_{1,3}\Omega_p - (\Gamma_1 + \Gamma_2)\rho_{3,3} - \gamma\rho_{3,3}. \quad (3)$$

Ω_p and Ω_c are complex Rabi frequencies:

$$\Omega_p = \frac{E_p \mu_{31}}{\hbar},$$

$$\Omega_c = \frac{E_c \mu_{32}}{\hbar}, \quad (4)$$

where μ_{31} and μ_{32} are electric dipole moments for the corresponding transitions. We have assumed complex Rabi frequencies, although it is not necessary for this scheme, like it is for the closed-loop schemes or for the Maxwell–Bloch equations. Note that with purely real Rabi frequencies, we obtained the same number of functionally independent CLs. Results we present in the following, but with complex Rabi frequencies replaced with real ones, represent functionally independent CLs for OBE with real Rabi frequencies.

Equation (3) also comprise relaxation and decoherence mechanisms. Terms with spontaneous emission can be obtained from the master equation [27], while relaxation due to the time of flight [28] and decoherence of optical coherences [29] are commonly added phenomenologically. Γ_1 and Γ_2 are the spontaneous emission rates from states 3 to 1 and 3 to 2, respectively. γ_1 and γ_2 are decay rates of coherences between those two pairs of states, caused by the elastic collisions. γ is rate of relaxation due to the time of flight.

3. Methodology of finding CLs

We search for possible CLs, denoted by T_t and satisfying equation:

$$\frac{dT_t}{dt} = 0 \quad (5)$$

on the solution of equation (3), by using method of multipliers. T_t represent quantities invariant in time, as such determined from the imposed initial condition. System of equation (3) is a system of nine independent equations with nine independent complex variables:

$$r_i = \rho_{11}, \rho_{12}, \dots, \rho_{33}, \quad i = 1, \dots, 9. \quad (6)$$

The procedure [25] of finding CLs starts from equation:

$$\frac{dT_t}{dt} = \sum_{i=1}^9 Q_i(L_i - R_i). \quad (7)$$

Q_i are multipliers, functions of r_i and their derivatives over time, which should be found. L_i and R_i are left and right-hand sides of OBEs (equation (3)). On the solutions of the equation (3), the left-hand side of equation (7) equals zero because T_t is the CL, while right-hand side becomes zero because equation (3) are identities.

We assume that T_t depends only on the density-matrix elements r_i :

$$T_t = T_t(\rho_{11}, \rho_{12}, \rho_{13}, \rho_{21}, \rho_{22}, \rho_{23}, \rho_{31}, \rho_{32}, \rho_{33}), \quad (8)$$

since their time derivatives can be expressed in terms of r_i , from equation (3). With this assumption, left-hand side of equation (7) stands:

$$\frac{dT_t}{dt} = \sum_{i=1}^9 \frac{\partial T_t}{\partial r_i} \frac{dr_i}{dt}. \quad (9)$$

We next introduce ansatz for each Q_i as the sum of density matrix elements and their products:

$$Q_i = \sum_{j=1}^9 c_i^j r_j + \sum_{j=1}^9 \sum_{k \leq j} c_i^{jk} r_j r_k, \quad (10)$$

where c_i^j and c_i^{jk} are arbitrary time-independent coefficients. In order to determine those coefficients we first apply the ansatz for the right-hand side of equation (7):

$$M = \sum_{i=1}^9 Q_i (L_i - R_i) \quad (11)$$

and then take variational derivative of equation (11) over T_t 's independent variables r_i , $i = 1, \dots, 9$. The standard Euler operator (or variational derivative) over function r_i is given with:

$$\frac{\delta}{\delta r_i} = \frac{\partial}{\partial r_i} - D_t \frac{\partial}{\partial r_{i,t}} + D_t^2 \frac{\partial}{\partial r_{i,tt}} - \dots, \quad (12)$$

where D_t is the total derivative operator:

$$D_t = \frac{\partial}{\partial t} + \sum_{i=1}^9 r_{i,t} \frac{\partial}{\partial r_i} + \sum_{i=1}^9 r_{i,tt} \frac{\partial}{\partial r_{i,t}} + \dots \quad (13)$$

and $r_{i,t}$ and $r_{i,tt}$ are first and second derivatives of r_i with respect to t .

Equations which are used to determine multipliers Q_i are obtained by taking variational derivatives of equation (11) over nine variables r_i :

$$\frac{\delta M}{\delta r_i} \equiv 0. \quad (14)$$

These equations must be satisfied identically and not only on the solution of equation (3). In order to determine multipliers Q_i , we equalize coefficients next to different products of r_i and their derivatives to 0. In this way we obtained linear system of equations over coefficients c_i^j and c_i^{jk} . This system is generally underdetermined and solution brings dependence of subset of coefficients, from equation (10), on other coefficients and the OBEs parameters.

We insert the solution for the multipliers Q_i into equation (7) obtaining as the result a lengthy equation. We group terms in equation next to first derivatives of variables r_i as:

$$\sum_{i=1}^9 \frac{dr_i}{dt} \left(\frac{\partial T_t}{\partial r_i} + f_i \right) \equiv 0. \quad (15)$$

f_i are polynomials in variables r_i , where coefficients in polynomials depend on the coefficients from ansatz in equation (10) and on various time-independent parameters from OBEs. From there we obtained system of nine partial differential equations:

$$\frac{\partial T_t}{\partial r_i} + f_i = 0, \quad i = 1, \dots, 9, \quad (16)$$

which we solve and obtain exact solution for T_t . By collecting terms in the solution with the remaining coefficients from equation (10), we obtain separate CLs. We note that T_t could be also obtained after multipliers are determined, by integrating M over time. However M is very lengthy expression containing products of CLs, whose integration represents computationally demanding task. We however have tested and compared both methods and obtained the same results.

4. Results for CLs obtained by the method of multipliers

We analyzed existence of CLs assuming that different phenomenological parameters in OBEs are non-zero. Results will be given for cases with or without relaxation and decoherence terms and for both detunings being either zero or different from zero. In the latter case we consider cases with different or equal detunings.

Since CLs can be combined to yield another CLs, we selected subset of functionally independent, among CLs with short form. Functional dependence of the obtained results was checked by using Jacobian matrix [30]. For a complex CL, both real and imaginary parts are separate CLs, therefore we have chosen purely real CLs in the set of functionally independent. We also present results only for the non-trivial CLs. There are two types of triviality [31]: when trivial CL vanishes for all solutions of the given system and when the divergence condition $\nabla T \equiv 0$ holds identically and not only on the solutions of the equation or system of equations in use.

4.1. CLs when OBEs are without relaxation and decoherence terms

We first consider the absence of relaxation and decoherence i.e. $\Gamma_1 = \Gamma_2 = \gamma_1 = \gamma_2 = \gamma = 0$. There are seven functionally independent CLs with ansatz (equation (10)):

$$T_t^1 = \rho_{1,1} + \rho_{2,2} + \rho_{3,3}, \quad (17)$$

$$T_t^2 = \rho_{1,2}\rho_{2,1} + \rho_{1,3}\rho_{3,1} + \rho_{2,3}\rho_{3,2} - \rho_{1,1}\rho_{2,2} - \rho_{1,1}\rho_{3,3} - \rho_{2,2}\rho_{3,3}, \quad (18)$$

$$T_t^3 = \rho_{1,2}\rho_{2,3}\rho_{3,1} + \rho_{1,3}\rho_{2,1}\rho_{3,2} + \rho_{1,1}\rho_{2,2}\rho_{3,3} \\ - \rho_{1,3}\rho_{2,2}\rho_{3,1} - \rho_{1,1}\rho_{2,3}\rho_{3,2} - \rho_{1,2}\rho_{2,1}\rho_{3,3}, \quad (19)$$

$$T_t^4 = \Omega_p\rho_{1,3} + \rho_{3,1}\Omega_p^* + \Omega_c\rho_{2,3} + \rho_{3,2}\Omega_c^* - \Delta_p\rho_{1,1} - \Delta_c\rho_{2,2},$$

$$T_t^5 = \rho_{1,1} \left(|\Omega_c|^2 + \frac{1}{2}\Delta_p(\Delta_c - \Delta_p) \right) + \rho_{2,2} \left(|\Omega_p|^2 + \frac{1}{2}\Delta_c(\Delta_p - \Delta_c) \right) \\ - \Omega_p\rho_{1,2}\Omega_c^* - \Omega_c\rho_{2,1}\Omega_p^* \\ - \frac{1}{2}(\Delta_c - \Delta_p)(-\rho_{3,2}\Omega_c^* - \Omega_c\rho_{2,3} + \rho_{3,1}\Omega_p^* + \Omega_p\rho_{1,3}), \quad (20)$$

$$T_t^6 = \Omega_p(\rho_{1,2}\rho_{2,3} - \rho_{1,3}\rho_{2,2}) + (\rho_{2,1}\rho_{3,2} - \rho_{2,2}\rho_{3,1})\Omega_p^* + \\ + \Omega_c(\rho_{1,3}\rho_{2,1} - \rho_{1,1}\rho_{2,3}) + (\rho_{1,2}\rho_{3,1} - \rho_{1,1}\rho_{3,2})\Omega_c^* \\ + \Delta_p(\rho_{2,3}\rho_{3,2} - \rho_{2,2}\rho_{3,3}) + \Delta_c(\rho_{1,3}\rho_{3,1} - \rho_{1,1}\rho_{3,3}) \quad (21)$$

and

$$\begin{aligned}
T_t^7 = & \Omega_p (\rho_{1,1}\rho_{3,3} - \rho_{1,3}\rho_{3,1}) \Omega_p^* + \Omega_p (\rho_{1,2}\rho_{3,3} - \rho_{1,3}\rho_{3,2}) \Omega_c^* \\
& + \Omega_c (\rho_{2,1}\rho_{3,3} - \rho_{2,3}\rho_{3,1}) \Omega_p^* + \Omega_c (\rho_{2,2}\rho_{3,3} - \rho_{2,3}\rho_{3,2}) \Omega_c^* \\
& + \frac{1}{2} (\Delta_c - \Delta_p) (\Omega_p (\rho_{1,3}\rho_{2,2} - \rho_{1,2}\rho_{2,3}) + \Omega_c (\rho_{1,3}\rho_{2,1} - \rho_{1,1}\rho_{2,3})) \\
& + (\rho_{2,2}\rho_{3,1} - \rho_{2,1}\rho_{3,2}) \Omega_p^* + (\rho_{1,2}\rho_{3,1} - \rho_{1,1}\rho_{3,2}) \Omega_c^* \\
& + \Delta_p (\rho_{2,2}\rho_{3,3} - \rho_{2,3}\rho_{3,2}) + \Delta_c (\rho_{1,3}\rho_{3,1} - \rho_{1,1}\rho_{3,3}). \quad (22)
\end{aligned}$$

4.2. CLs when relaxation, decoherence and detunings in OBEs are zero

Although one could expect additional symmetry for the case of equal detunings of light fields in the Λ scheme (figure 1), we obtained the same seven CLs, $T_t^1, \dots, T_t^7|_{\Delta_p=\Delta_c}$. However for the case of light fields at the resonance frequencies, besides $T_t^1, \dots, T_t^7|_{\Delta_{p,c}=0}$, we obtained additional CL:

$$T_t^8 = (\Omega_p \rho_{1,2} \Omega_c^* - \Omega_c \rho_{2,1} \Omega_p^*)^2 - |\Omega_c|^2 (\rho_{3,1} \Omega_p^* + \Omega_p \rho_{1,3})^2 - |\Omega_p|^2 (\rho_{3,2} \Omega_c^* + \Omega_c \rho_{2,3})^2. \quad (23)$$

4.3. CLs with relaxation and decoherence terms in OBEs

For any combination of the parameters, $\Gamma_1, \Gamma_2, \gamma_1$ and γ_2 being non-zero, we obtained expected result—conservation of density-matrix trace T_t^1 . For non-zero decoherence rates, $\gamma_1 \neq 0$ and/or $\gamma_2 \neq 0$, and for equal light-fields detunings, $\Delta_p = \Delta_c$, besides T_t^1 we obtained CL:

$$T_t^9 = \rho_{1,1} |\Omega_c|^2 + \rho_{2,2} |\Omega_p|^2 - \Omega_p \rho_{1,2} \Omega_c^* - \Omega_c \rho_{2,1} \Omega_p^*. \quad (24)$$

This CL is the same as T_t^5 for equal detunings. For the case of different detunings and non-zero decoherence rates γ_1 and γ_2 , we obtained only T_t^1 .

5. Discussion of results obtained by the method of multipliers

OBEs without relaxation and decoherence terms are equivalent to the Liouville von Neumann equation for the density matrix:

$$\frac{d\hat{\rho}}{dt} = -\frac{i}{\hbar} [\hat{H}, \hat{\rho}]. \quad (25)$$

CLs, or constants of motion, of the Liouville von Neumann equation have been previously studied in the literature. Highest number of CLs has been determined by Mallesh and Ramachandran [24] who have shown that for the arbitrary scheme with N levels, interacting with $N - 1$ optical fields, there exist in general $N^2 - N + 1$ independent invariants of motion, when the Hamiltonian assumes a time-independent form under a suitable unitary transformation.

As we have presented in the previous Section, our search for CLs gave more than $N^2 - N + 1$ functionally independent CLs when the light fields are resonant, $\Delta_p = \Delta_c = 0$. We have checked, compared and found that our results for CLs, $T_t^1 - T_t^7$ are functionally dependent on the ones obtained by the procedure given in [24] and vice versa. Compared to CLs obtained by their formulas [24], our CLs generally have shorter form (less number of addends)

and our expressions are invariant in respect to exchange of levels 1 and 2 and the corresponding coupling fields (see figure 1).

Mallesh and Ramachandran [24] gave two procedures for obtaining $N^2 - N + 1$ functionally independent CLs, one of which is by using trace of matrix product:

$$\begin{aligned} C_q^p &= \text{Tr}(\hat{\rho} \hat{H}^q)^p, \\ D_q^p &= \text{Tr}(\hat{\rho}^p \hat{H}^q), \\ q &= 0, \quad p = 1, 2, \dots, N, \\ q &= 1, 2, \dots, N-1, \quad p = 1, 2, \dots, N-1. \end{aligned} \quad (26)$$

Either C_q^p or D_q^p can be used to calculate set of functionally independent CLs. \hat{H} is the time-independent Hamiltonian in the interaction picture and under the rotating wave approximation. For the Λ scheme with notation of levels and optical fields given in figure 1, it stands:

$$H = \begin{pmatrix} 0 & 0 & -\hbar\Omega_p^* \\ 0 & \hbar\Delta_c - \hbar\Delta_p & -\hbar\Omega_c^* \\ -\hbar\Omega_p & -\hbar\Omega_c & -\hbar\Delta_p \end{pmatrix}. \quad (27)$$

By further analyzing approach given by Mallesh, we found shorter expressions for CLs, obtained by the products of Hamiltonian and derivatives of density matrix. With the first three CLs same as in Mallesh formula, the following set also forms seven functionally independent CLs of Liouville von Neumann equation for the Λ scheme:

$$\begin{aligned} X_t^i &= \text{Tr} \hat{\rho}^i, \quad i = 1, 2, 3, \\ X_t^{i+4} &= \text{Tr}[(\frac{d^i}{dt^i} \hat{\rho}) \cdot \hat{H} \cdot \hat{\rho}], \quad i = 0, 1, 2, 3. \end{aligned} \quad (28)$$

These expressions are results of products of maximum three matrices, whereas equation (26) represent product of maximum six matrices in C_q^p or four matrices in D_q^p . Another form which can be used, instead of the last four CLs in the previous equation is:

$$X_t^{i,j} = \text{Tr}[(\frac{d^i}{dt^i} \hat{\rho}) \cdot \hat{H} \cdot (\frac{d^j}{dt^j} \hat{\rho})], \quad i, j = 0, 1, 2, \dots \quad (29)$$

among which the set of functionally-independent CLs can be selected.

We also further analyzed properties of matrix products of density matrix and Hamiltonian for arbitrary N -level scheme. We made generalization of equation (26) by introducing the following quantities:

$$\hat{T}_{(a_1, a_2, \dots, a_k)} \equiv \hat{\rho}^{a_1} \hat{H}^{a_2} \hat{\rho}^{a_3} \dots \hat{\rho}^{a_{k-1}} \hat{H}^{a_k}, \quad (30)$$

which represent products of any powers of density matrix $\hat{\rho}$ and interaction Hamiltonian H , regardless of order, since powers a_1, a_2, \dots, a_k can take values of natural numbers including zero. As we show in appendix A it evolves according to Liouville von Neumann equation:

$$\frac{d}{dt} \hat{T}_{(a_1, a_2, \dots, a_k)} = \frac{1}{i\hbar} [\hat{H}, \hat{T}_{(a_1, a_2, \dots, a_k)}]. \quad (31)$$

Due to this property, quantities given with equation (30) yield infinitely many CLs. By taking trace of equation (31) we have:

$$\begin{aligned}\frac{d}{dt}\text{Tr} \hat{T}_{(a_1, a_2, \dots, a_k)} &= \frac{1}{i\hbar} \text{Tr}[\hat{H}, \hat{T}_{(a_1, a_2, \dots, a_k)}] \\ &= \frac{1}{i\hbar} [\text{Tr}(\hat{H} \cdot \hat{T}_{(a_1, a_2, \dots, a_k)}) - \text{Tr}(\hat{T}_{(a_1, a_2, \dots, a_k)} \cdot \hat{H})] = 0,\end{aligned}\quad (32)$$

due to invariance of trace under cyclic permutations of matrices.

Since our analysis is for equations with only one independent variable, any function of CLs also represent CL due to property of a composite function $\frac{dF(T(t))}{dt} = \frac{dT(t)}{dt} \frac{dF(T(t))}{dT(t)}$. We show that as a consequence of equation (32), characteristic polynomials and their coefficients, determinants and eigen-values of matrices $T_{(a_1, a_2, \dots, a_k)}$, are also CLs for Liouville von Neumann equation for arbitrary N -level scheme, not just for Λ .

Coefficients of characteristic polynomial:

$$p(\lambda) \equiv \det(\lambda I_N - A) \equiv \lambda^N + c_{N-1}\lambda^{N-1} + \dots + c_1\lambda + c_0, \quad (33)$$

of arbitrary square matrix A can be calculated from traces of various powers of A [32]. Therefore, each coefficient c_0, c_1, \dots, c_{N-1} in equation (33) represents CL. Consequently, eigenvalues of matrices $\hat{T}_{(a_1, a_2, \dots, a_k)}$, which are the solution for λ when equation (33) equals to zero, are the functions of the coefficients c_0, c_1, \dots, c_{N-1} and represent CLs. It follows that whole characteristic polynomial is CL. Determinant of quantities given with equation (30) is also CL due to the property $\text{Det}(A) = (-1)^N c_0$ or $\text{Det}(A) = \prod_{i=1}^N E_i$ for the arbitrary square matrix A , where E_i are its eigenvalues.

Another quantity which is conserved in time and whose value is determined from the initial condition is von Neumann entropy:

$$S = -\text{Tr}(\hat{\rho} \ln \hat{\rho}) = -\sum_i E_i \ln E_i \quad (34)$$

expressed through the eigen-values of density matrix $\hat{\rho}$.

As we have presented in the previous section, for the case when light fields are at the resonance frequency, $\Delta_p = \Delta_c = 0$, there are total of eight functionally independent CLs, T_t^1, \dots, T_t^8 . Result given with T_t^8 can not be calculated by using methods previously presented in the literature [22, 24]. The presented form depends on the coherences only, and can be expressed through the real and imaginary parts as:

$$T_t^{8(A)} = \Im(\Omega_p \rho_{1,2}(\Omega_c)^*)^2 + |\Omega_c|^2 \Re(\Omega_p \rho_{1,3})^2 + |\Omega_p|^2 \Re(\Omega_c \rho_{2,3})^2. \quad (35)$$

T_t^8 combined with trivial CLs (which are equations from equation (3)) yields CL which depends on the optical coherences and their derivatives only:

$$\begin{aligned}T_t^{8(B)} &= |\Omega_c|^2 (\rho_{3,1}\Omega_p^* + \Omega_p \rho_{1,3})^2 + |\Omega_p|^2 (\rho_{3,2}\Omega_c^* + \Omega_c \rho_{2,3})^2 \\ &\quad + \frac{1}{2} \left(\frac{\partial \rho_{3,1}}{\partial t} \Omega_p^* + \Omega_p \frac{\partial \rho_{1,3}}{\partial t} \right)^2 + \frac{1}{2} \left(\frac{\partial \rho_{3,2}}{\partial t} \Omega_c^* + \Omega_c \frac{\partial \rho_{2,3}}{\partial t} \right)^2.\end{aligned}\quad (36)$$

In addition, we analyzed CLs valid only for pure states, which are subset of all mixed states. The set of functionally independent CLs for pure states can be represented by CLs T_t^1, T_t^4 and T_t^5 , with additional T_t^8 when detunings are zero. It shows that for pure states the

number of functionally independent CLs can also be larger than $N = 3$, as given by Mallesh and Ramachandran [24]. We will investigate existence of additional CLs for the Lioville von Neumann equation for other level-schemes, before bringing any conclusion on the physical interpretation of T_t^8 or the methodology to obtain them, besides the method we used.

Results given with expression T_t^9 is well known in the literature, although it is not referred as CL. It represents population of dark-state [7]. In the dark-state two light fields interfere destructively and the atom (or other interacting media) cannot be excited. Mathematically, dark-state for equal detunings is given as the eigen-vector of the interaction Hamiltonian and the population of dark-state is straightforward calculation. We obtained that the dark-state population is conserved even with decay of optical coherences, $\gamma_1, \gamma_2 \neq 0$, the fact that hasn't been emphasized in the literature.

For $\gamma \neq 0$ we did not obtain that the trace of the density matrix T_t^1 (or total population of the ensemble) is conserved. Equation (3) are given as usual in the literature—total population of particles (atoms, molecules) that leave the interaction region with the rate γ is $\text{Tr } \hat{\rho}$, while total population of particles that enter equals 1, with even population among ground-state sublevels. We did not impose what is also common in the literature, that $\text{Tr } \hat{\rho} = 1$, but instead obtained $\text{Tr } \hat{\rho} \equiv T_t^1$ as the constant of motion when $\gamma = 0$. For values $\gamma \neq 0$, we obtained CL which can be considered analogous, as will be presented in the next section.

6. Obtaining CLs valid with relaxation terms

In this section, we used results obtained by the method of multipliers to develop another set of CLs. These CLs are valid for the larger set of parameters compared to the results obtained by the method multipliers, with relaxation due to time of flight and spontaneous emission.

With the set of all parameters from OBEs, denoted as:

$$\Pi = \{\Gamma_1, \Gamma_2, \gamma_1, \gamma_2, \gamma, \Delta_p, \Delta_c\}, \quad (37)$$

and with P_0 as the subset of parameters considered to be zero, we have the set of k valid CLs:

$$\frac{dT_t^i}{dt}|_{P_0} = 0, \quad i = 1, 2, \dots, k. \quad (38)$$

We analyzed 'breaking' of CLs—the case when some of parameters from P_0 are set to be non-zero. If instead of P_0 , a subset of parameters $P_0^S \subset P_0$ is taken to be zero, equation (38) stands:

$$\frac{dT_t^i}{dt}|_{P_0^S} = R^i, \quad i = 1, 2, \dots, k. \quad (39)$$

Quantities R^i depend on the non-zero parameters $P = \Pi \setminus P_0^S$ and the density matrix elements.

The following steps still have to be fulfilled—condition that R^i can be expressed as a functions of T_t^i :

$$\frac{dT_t^i}{dt}|_{P_0^S} = f_i(T_t^j), \quad i, j = 1, 2, \dots, k, \quad (40)$$

and that previous equation allows general integral and represents solvable system of differential equations. Then it follows:

$$T_t^i|_{P_0^S} = F_i(t, C_j), \quad i, j = 1, 2, \dots, k. \quad (41)$$

Solutions $F_i(t, C_j)$ depend on the constants of integration C_j , which also represent constants of motion and new CLs, valid for larger set of parameters. Solving equation (41) over integration constants C_j leads to:

$$C_j = \tau_j(T_t^j, t), \quad i, j = 1, 2, \dots, k. \quad (42)$$

The functions τ_j are new CLs valid for OBEs with the set of parameters P non-zero.

6.1. Results for CLs valid with relaxation terms

T_t^1 is CL for any values of parameters in OBEs except γ which has to be zero. If we set $\gamma \neq 0$, from the steps described above we obtain:

$$\begin{aligned} \frac{dT_t^1}{dt} &= \gamma(1 - T_t^1), \\ T_t^1 &= 1 + e^{-\gamma t} C_1, \\ \tau_t^1 &= e^{\gamma t}(1 - T_t^1). \end{aligned} \quad (43)$$

τ_t^1 is valid for OBEs with all parameters non-zero, $P = \Pi$. As already discussed, τ_t^1 can be considered analogous to T_t^1 when $\gamma \neq 0$. If the initial condition is $\text{Tr } \hat{\rho} \neq 1$, the trace of the density matrix will tend to unity exponentially with time.

CLs T_t^1, \dots, T_t^7 are CLs for OBEs with parameters $P_0 = \{\Gamma_1, \Gamma_2, \gamma_1, \gamma_2, \gamma\}$ zero. For $\gamma \neq 0$, besides T_t^1 , we obtained two more CLs for which variables R_i can be expressed as the linear combination of CLs, which yields new CLs:

$$\begin{aligned} \tau_t^4 &= -e^{\gamma t} \left(T_t^4 + \frac{1}{2}(\Delta_c + \Delta_p) \right), \\ \tau_t^5 &= e^{\gamma t} \left(-\frac{1}{4}(\Delta_c - \Delta_p)^2 + \frac{1}{2}(|\Omega_c^2| + |\Omega_p^2|) - T_t^5 \right), \end{aligned} \quad (44)$$

valid for OBEs with parameters $P = \{\gamma, \Delta_p, \Delta_c\}$ non-zero.

Without relaxation and decoherence terms and if light electric fields are at the resonance frequencies, $P_0 = \Pi$, set of valid CLs are $T_t^1, \dots, T_t^7|_{P_0}$ and T_t^8 . If $\gamma \neq 0$, besides already obtained τ_t^1 and the special cases of τ_t^4 and τ_t^5 :

$$\begin{aligned} \tau_t^{4(A)} &= \tau_t^4|_{P_0^S} = e^{\gamma t} T_t^4|_{P_0^S}, \\ \tau_t^{5(A)} &= \tau_t^5|_{P_0^S} = -\frac{1}{2}e^{\gamma t}(|\Omega_c^2| + |\Omega_p^2| - 2T_t^5|_{P_0^S}), \end{aligned} \quad (45)$$

then there are two more CLs:

$$\begin{aligned} \tau_t^6 &= \frac{1}{2}e^{\gamma t}((e^{\gamma t} - 1)T_t^4|_{P_0^S} + 2e^{\gamma t}T_t^6|_{P_0^S}), \\ \tau_t^8 &= e^{2\gamma t}T_t^8, \end{aligned} \quad (46)$$

valid for OBEs with parameters $P_0^S = \Pi \setminus \{\gamma\}$ set to zero.

If for the same set of CLs, valid if $P_0 = \Pi$, we take $\Gamma_1 \neq 0, \Gamma_2 \neq 0$ and $\gamma \neq 0$, the CL T_t^4 yields:

$$\tau_t^{4(B)} = e^{\gamma t + \frac{1}{2}(\Gamma_1 + \Gamma_2)t} T_t^4|_{P_0^S}, \quad (47)$$

valid with both relaxation due to time of flight and spontaneous emission, and when light fields are resonant, $P = \{\Gamma_1, \Gamma_2, \gamma\}$.

For the case of equal detunings $\Delta_p = \Delta_c$, the CL T_t^9 holds with $P_0 = \{\Gamma_1, \Gamma_2, \gamma\}$. For $\gamma \neq 0$, we have CL:

$$\tau_t^9 = -\frac{1}{2} e^{\gamma t} (|\Omega_c^2| + |\Omega_p^2| - 2T_t^9), \quad (48)$$

valid for OBEs when the parameters $P = \{\gamma_1, \gamma_2, \gamma\}$ are non-zero and under condition of equal detunings, $\Delta_p = \Delta_c$.

7. Conclusions

We presented CLs for the OBEs for the Λ scheme under action of two optical fields. One set of results was obtained by using the method of multipliers and these CLs depend on the density-matrix only. We searched for CLs assuming the various phenomenological parameters of OBEs are either zero or nonzero. We found additional CLs when light fields are at the resonance frequencies or if detunings of light fields are equal.

Without relaxation and decoherence terms OBEs are equivalent to the Liouville von Neumann equation, the case we analyzed in particular. We have shown that for the case when the excitation fields are at the resonance frequency, Liouville von Neumann equation for the Λ scheme has one more additional functionally independent CL, compared to the previously published results [24]. We introduced quantity which represents class of matrices and a generalization of previous methods [24]—product of density matrix and Hamiltonian, under the rotating wave approximation, but of any powers and any order of two matrices. By calculating evolution of this quantity, we have shown that traces, characteristic polynomials and their coefficients, eigen-values and determinants of these quantities, represent CLs for the Liouville von Neumann equation, for arbitrary N -level scheme. It is also presented that the set of functionally independent CLs for OBEs for the Λ scheme can be obtained from matrix products of Hamiltonian and higher derivatives of density matrix.

CLs obtained by the method of multipliers were used to obtain another set of CLs. We presented method to construct CLs, which are valid for the larger set of OBEs parameters—those we assumed to be zero when constructing CLs by the method of multipliers. These CLs were obtained when the spontaneous emission, relaxation due to the time of flight and decay of optical coherences due to elastic collisions are nonzero in OBEs. Presented results could have practical applications in various solution methods as well fundamental interest through the better understanding of processes modeled by the OBEs for the Λ scheme.

Acknowledgments

The authors acknowledge funding provided by the Institute of Physics Belgrade, through the grant by the Ministry of Education, Science, and Technological Development of the Republic of Serbia. The authors also acknowledge funding by the Photonics Center, Laboratory for Quantum and Atomic Physics of the Institute of Physics Belgrade.

Appendix A. Derivation of equation (31)

Evolution of quantities $\hat{T}_{(a_1, a_2, \dots, a_k)}$, given with equation (30), is as follows:

$$\begin{aligned}
 \frac{d}{dt} \hat{T}_{(a_1, a_2, \dots, a_k)} &= \left(\frac{d}{dt} \hat{\rho}^{a_1} \right) \hat{H}^{a_2} \hat{\rho}^{a_3} \dots \hat{\rho}^{a_{k-1}} \hat{H}^{a_k} + \hat{\rho}^{a_1} \hat{H}^{a_2} \left(\frac{d}{dt} \hat{\rho}^{a_3} \right) \dots \hat{\rho}^{a_{k-1}} \hat{H}^{a_k} \\
 &\quad + \dots + \hat{\rho}^{a_1} \hat{H}^{a_2} \hat{\rho}^{a_3} \dots \left(\frac{d}{dt} \hat{\rho}^{a_{k-1}} \right) \hat{H}^{a_k} \\
 &= \frac{1}{i\hbar} [(\hat{H} \hat{\rho}^{a_1} - \hat{\rho}^{a_1} \hat{H}) \hat{H}^{a_2} \hat{\rho}^{a_3} \dots \hat{\rho}^{a_{k-1}} \hat{H}^{a_k} \\
 &\quad + \hat{\rho}^{a_1} \hat{H}^{a_2} (\hat{H} \hat{\rho}^{a_3} - \hat{\rho}^{a_3} \hat{H}) \dots \hat{\rho}^{a_{k-1}} \hat{H}^{a_k} + \dots + \\
 &\quad + \hat{\rho}^{a_1} \hat{H}^{a_2} \hat{\rho}^{a_3} \dots (\hat{H} \hat{\rho}^{a_{k-1}} - \hat{\rho}^{a_{k-1}} \hat{H}) \hat{H}^{a_k}] \\
 &= \frac{1}{i\hbar} [\hat{H} \hat{T}_{(a_1, a_2, \dots, a_k)} - \hat{T}_{(a_1, a_2+1, \dots, a_k)} + \hat{T}_{(a_1, a_2+1, \dots, a_k)} \\
 &\quad - \hat{T}_{(a_1, a_2, a_3, a_4+1, \dots, a_k)} + \dots + \hat{T}_{(a_1, a_2, \dots, a_{k-2}+1, a_{k-1}, a_k)} - \hat{T}_{(a_1, a_2, \dots, a_k)} \hat{H}] \\
 &= \frac{1}{i\hbar} [\hat{H}, \hat{T}_{(a_1, a_2, \dots, a_k)}], \tag{A.1}
 \end{aligned}$$

where we have used property that arbitrary power of density-matrix also evolves according to the Liouville von Neumann equation:

$$\begin{aligned}
 \frac{d}{dt} \hat{\rho}^a &= \dot{\hat{\rho}} \hat{\rho}^{a-1} + \hat{\rho} \dot{\hat{\rho}} \hat{\rho}^{a-2} + \dots + \hat{\rho}^{a-1} \dot{\hat{\rho}} \\
 &= \frac{1}{i\hbar} ((\hat{H} \hat{\rho} - \hat{\rho} \hat{H}) \hat{\rho}^{a-1} + \hat{\rho} (\hat{H} \hat{\rho} - \hat{\rho} \hat{H}) \hat{\rho}^{a-2} + \dots + \hat{\rho}^{a-1} (\hat{H} \hat{\rho} - \hat{\rho} \hat{H})) \\
 &= \frac{1}{i\hbar} (\hat{H} \hat{\rho}^a - \hat{\rho}^a \hat{H}) = \frac{1}{i\hbar} [\hat{H}, \hat{\rho}^a]. \tag{A.2}
 \end{aligned}$$

This property (equation (A.2)) has been previously presented by Radmore *et al* [33].

ORCID iDs

Jelena Dimitrijević  <https://orcid.org/0000-0002-1392-1058>

References

- [1] Cohen-Tannoudji C, Dupont-Roc J and Grynberg G 1998 *Atom–Photon Interactions* (New York: Wiley)
- [2] Allen L and Eberly J H 1987 *Optical Resonance and Two-Level Atoms* (Dover Books on Physics) (New York: Dover)
- [3] Harris S E 1997 Electromagnetically induced transparency *Phys. Today* **50** 36–42
- [4] Fleischhauer M, Imamoglu A and Marangos J P 2005 Electromagnetically induced transparency: optics in coherent media *Rev. Mod. Phys.* **77** 633–73
- [5] Arimondo E 1996 V coherent population trapping in laser spectroscopy *Progress in Optics* (Amsterdam: Elsevier) pp 257–354
- [6] Vanier J 2005 Atomic clocks based on coherent population trapping: a review *Appl. Phys. B* **81** 421–42

- [7] Cohen-Tannoudji C and Guéry-Odelin D 2011 *Advances in Atomic Physics* (Singapore: World Scientific)
- [8] LeVeque R J 1992 *Numerical Methods for Conservation Laws* (Basel: Birkhäuser)
- [9] Grant T J 2015 Bespoke finite difference schemes that preserve multiple conservation laws *LMS J. Comput. Math.* **18** 372–403
- [10] Naz R, Mahomed F M and Mason D P 2008 Comparison of different approaches to conservation laws for some partial differential equations in fluid mechanics *Appl. Math. Comput.* **205** 212–30
- [11] Wolf T 2002 A comparison of four approaches to the calculation of conservation laws *Eur. J. Appl. Math.* **13** 129–52
- [12] Saberi E and Hejazi S R 2019 A comparison of conservation laws of the Boussinesq system *Kragujevac J. Math.* **43** 173–200
- [13] Noether E 1971 Invariant variation problems *Transp. Theory Stat. Phys.* **1** 186–207
- [14] Kara A H, Razborova P and Biswas A 2015 Solitons and conservation laws of coupled Ostrovsky equation for internal waves *Appl. Math. Comput.* **258** 95–9
- [15] Buhe E, Bluman G W, Alatanjang C and Yulan H 2018 Some approaches to the calculation of conservation laws for a telegraph system and their comparisons *Symmetry* **10** 182
- [16] Kara A H and Mahomed F M 2002 A basis of conservation laws for partial differential equations *J. Nonlinear Math. Phys.* **9** 60–72
- [17] Hioe F T and Eberly J H 1981 n -level coherence vector and higher conservation laws in quantum optics and quantum mechanics *Phys. Rev. Lett.* **47** 838–41
- [18] Hioe F T and Eberly J H 1982 Nonlinear constants of motion for three-level quantum systems *Phys. Rev. A* **25** 2168–71
- [19] Hioe F T 1983 Dynamic symmetries in quantum electronics *Phys. Rev. A* **28** 879–86
- [20] Gottlieb H P W 1982 Linear constants of motion for a three-level atom excited by two modulated electromagnetic waves *Phys. Rev. A* **26** 3713–5
- [21] Gottlieb H P W 1985 Second invariant in an excited three-level system *Phys. Rev. A* **32** 653–4
- [22] Hioe F T 1984 Linear and nonlinear constants of motion for two-photon processes in three-level systems *Phys. Rev. A* **29** 3434–6
- [23] Ravishankar V 1987 Spin 1 and 3/2 systems in quadrupole fields *Mol. Phys.* **62** 1409–18
- [24] Mallesh K S and Ramachandran G 1989 Invariants of motion for an n -level system *J. Phys. B: At. Mol. Opt. Phys.* **22** 2311–8
- [25] Naz R 2010 Conservation laws for a complexly coupled KdV system, coupled Burgers' system and Drinfeld–Sokolov–Wilson system via multiplier approach *Commun. Nonlinear Science Numer. Simul.* **15** 1177–82
- [26] Naz R 2012 Conservation laws for some systems of nonlinear partial differential equations via multiplier approach *J. Appl. Math.* **2012** 1–13
- [27] Carmichael H J 1999 *Statistical Methods in Quantum Optics* vol 1 (Berlin: Springer)
- [28] Patnaik A K, Hsu P S, Agarwal G S, Welch G R and Scully M O 2007 Measurement of ground-state decoherence via interruption of coherent population trapping *Phys. Rev. A* **75** 023807
- [29] Beeker W P 2004 EIT and other optical effects in numerical models and experiments *Master's Thesis* Department of Applied Science, University of Twente, The Netherlands
- [30] Newns W F 1967 Functional dependence *Am. Math. Mon.* **74** 911
- [31] Olver P J 1986 *Applications of Lie Groups to Differential Equations* (Berlin: Springer)
- [32] Reed M and Simon B 1978 *Analysis of Operators (Methods of Modern Mathematical Physics)* (New York: Academic)
- [33] Radmore P M, Barnett S M and Stoneham A M 1990 Conserved quantities for the density matrix and the degree of statistical mixing *Phys. Scr.* **42** 129–32

Comparison of a double- Λ atomic scheme with single- and two-fold coupled transitions

This content has been downloaded from IOPscience. Please scroll down to see the full text.

2012 Phys. Scr. 2012 014008

(<http://iopscience.iop.org/1402-4896/2012/T149/014008>)

View [the table of contents for this issue](#), or go to the [journal homepage](#) for more

Download details:

IP Address: 147.91.1.43

This content was downloaded on 10/11/2016 at 16:25

Please note that [terms and conditions apply](#).

You may also be interested in:

[Simple analytical expressions for the analysis of the phase-dependent electromagnetically induced transparency in a double- atomic scheme](#)

J Dimitrijevi and D Arsenovi

[Phase control of cross-phase modulation with EIT](#)

Hui Sun, Yueping Niu, Shiqi Jin et al.

[Coherent population trapping in three-level systems](#)

Xiang-ming Hu and Jie-Peng Zhang

[A study of the ac Stark effect in doped photonic crystals](#)

I Haque and Mahi R Singh

[Tunable offset locking in a system: an experimental study on the rubidium atom](#)

Md Sabir Ali, Ayan Ray and Alok Chakrabarti

[Control of the spontaneous emission spectrum in a driven N-type atom by dynamically induced quantum interference](#)

Bibhas Kumar Dutta and Prasanta Kumar Mahapatra

Comparison of a double- Λ atomic scheme with single- and two-fold coupled transitions

D Arsenović and J Dimitrijević

Institute of Physics, University of Belgrade, Pregrevica 118, 10080 Belgrade, Serbia

E-mail: jelena.dimitrijevic@ipb.ac.rs

Received 7 September 2011

Accepted for publication 25 November 2011

Published 27 April 2012

Online at stacks.iop.org/PhysScr/T149/014008

Abstract

A four-level double- Λ atomic scheme, i.e. two Λ systems sharing the same two ground levels, that interacts with four laser light fields is studied theoretically. The peculiarity is that each of the two ground states can be coupled to each excited state by two laser light fields. A certain energy difference exists between excited-state levels. We consider this energy small enough so that a laser resonant to either transition can also couple the other transition. We test whether coupling of the more detuned laser is not non-negligible. Multiply connected states were also recently analyzed (and a comparison with experiment was presented), but for the simpler, two- and three-level atomic schemes (Stacey *et al* 2008 *J. Phys. B: At. Mol. Opt. Phys.* **41** 085502). Theoretical treatment of the double- Λ atomic scheme is commonly done by solving optical Bloch equations (OBEs). When the rotating-wave approximation (RWA) is applied, OBEs become, by their form, a set of linear differential equations with constant coefficients. Theoretical treatment of the interaction scheme treated here leads to OBEs with coefficients that are not constant, but oscillate with time, even after RWA is applied. Under certain assumptions, the approximation can be used where the time-dependent coefficients are averaged over their periods. The method yields a new system of equations (similar to standard OBEs), but with more independent variables, and can also be solved in the usual way. The results presented here analyze the validity of this approximation by comparing the results for the double- Λ atomic scheme with single- and two-fold coupled transitions. We test whether in the limit of large-energy splitting between excited-state levels both approaches lead to similar results.

PACS numbers: 42.50.Gy, 42.50.Md, 42.50.Ar

(Some figures may appear in colour only in the online journal)

1. Introduction

Excitations of various atomic schemes by lasers were studied in systems as simple as two level and three level, such as Λ , V or ladder configuration, to complex multilevel systems with or without Zeeman splitting. These interactions have been shown to give rise to interesting effects such as coherent population trapping [2], electromagnetically induced transmission [3] and electromagnetically induced absorption [4]. The double- Λ atomic scheme, i.e. two Λ systems sharing the same two ground levels (see figure 1), has also been shown to be of interest as the basis for many investigations and applications [5, 6]. In this paper, we study a double- Λ atomic

scheme where each of the transitions between two ground and two excited levels is coupled by two lasers (see figure 1(b)). We test whether optical Bloch equations (OBEs) can be solved for this interaction scheme and compare the results with the standard, single-fold coupled double- Λ , i.e. each transition driven by only one laser (figure 1(a)).

2. Theoretical model for the two-fold coupled double- Λ atomic scheme

We solve OBEs:

$$\frac{d\hat{\rho}(t)}{dt} = -\frac{i}{\hbar}[\hat{H}_0, \hat{\rho}(t)] - \frac{i}{\hbar}[\hat{H}_1, \hat{\rho}(t)] - \hat{S}\hat{E}\hat{\rho}(t) - \gamma\hat{\rho}(t) + \gamma\hat{\rho}_0 \quad (1)$$

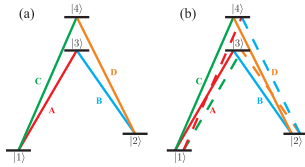


Figure 1. Double- Λ configuration of levels with single-fold (a) and two-fold (b) coupled states. Four lasers A , B , C and D couple atomic states as indicated in the figure, where additional couplings are denoted by dashed lines.

for the double- Λ schemes given in figure 1. In equation (1), \hat{H}_0 is the Hamiltonian of the free, four-level atom and \hat{H}_I is the interaction Hamiltonian of an atom interacting with four laser fields. $\hat{S}E$ represents the operator of spontaneous emission with rate Γ for both excited levels, $\gamma\hat{\rho}$ is the relaxation due to time of flight and $\gamma\hat{\rho}_0$ describes the continuous flux of atoms to the laser beam, with equally populated ground-state levels.

Following the procedure described in [1], we next discuss whether OBEs with constant coefficients can be obtained for the interaction scheme given in figure 1(b). In the following, expressions for coherences ρ_{ij} will be presented, while for ρ_{ji} the corresponding complex conjugates need to be taken. The following substitution is made to optical coherences ρ_{13} , ρ_{14} , ρ_{23} and ρ_{24} :

$$\begin{aligned}\rho_{13} &= \tilde{\rho}_{13}^A e^{i\omega_A t} + \tilde{\rho}_{13}^C e^{i\omega_C t}, & \rho_{14} &= \tilde{\rho}_{14}^C e^{i\omega_C t} + \tilde{\rho}_{14}^A e^{i\omega_A t}, \\ \rho_{23} &= \tilde{\rho}_{23}^B e^{i\omega_B t} + \tilde{\rho}_{23}^D e^{i\omega_D t}, & \rho_{24} &= \tilde{\rho}_{24}^D e^{i\omega_D t} + \tilde{\rho}_{24}^B e^{i\omega_B t},\end{aligned}\quad (2)$$

where ω_K (K is a laser) are lasers' frequencies which satisfy the multi-photon resonance condition:

$$\omega_A - \omega_B = \omega_C - \omega_D. \quad (3)$$

In a closed-loop interaction scheme, such as double- Λ , the steady state can be reached only if this condition is satisfied [6].

The next step is to write explicitly equations for the density matrix elements from the interaction part of Liouville's equation (equation (1)) with substituted optical coherences (equation (2)). This yields the new set equations, where we next analyze equations for coherences ρ_{12} and ρ_{34} . For these coherences there appear three groups of terms on the rhs that oscillate with specific frequency, $e^{i(\omega_A - \omega_B)t}$, $e^{i(\omega_C - \omega_D)t}$, $e^{i(\omega_A - \omega_C)t}$, $e^{i(\omega_B - \omega_D)t}$ for ρ_{12} and $e^{i(\omega_A - \omega_C)t}$, $e^{i(\omega_B - \omega_D)t}$ for ρ_{34} . These oscillatory terms introduce substitutions for coherences ρ_{12} and ρ_{34} as follows:

$$\begin{aligned}\rho_{12} &= \tilde{\rho}_{12}^{AB} e^{i(\omega_A - \omega_B)t} + \tilde{\rho}_{12}^{CD} e^{i(\omega_C - \omega_D)t} + \tilde{\rho}_{12}^{AD} e^{i(\omega_A - \omega_D)t} \\ \rho_{34} &= \tilde{\rho}_{34}^{CA} e^{i(\omega_C - \omega_A)t} + \tilde{\rho}_{34}^{DB} e^{i(\omega_D - \omega_B)t} + \tilde{\rho}_{34}^{AC} e^{i(\omega_A - \omega_C)t}.\end{aligned}\quad (4)$$

New variables, given by equations (2) and (4), are next inserted into equation (1). This yields equations of the form $\sum_k e^{i\omega_k t} c_k^{ij} = 0$ (one for each matrix element ρ_{ij}) or equivalently the new set of differential and algebraic equations, $\dot{c}_k^{ij} = 0$. The approximation we use consists in omitting the algebraic subset, which is the same as the standard rotating-wave approximation for the OBEs with single-fold couplings. The difference is that the latter procedure introduces more approximations, i.e. more terms have to be neglected. The subset of differential equations

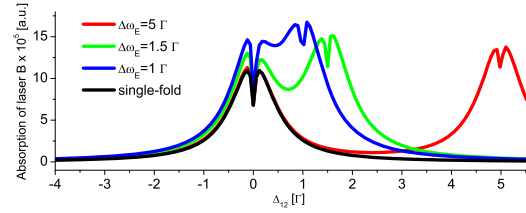


Figure 2. Steady-state absorption of laser B for three different energy splittings between excited levels for the two-fold coupled transitions. Absorption for the single-fold coupled transition is also presented by the black curve. Steady-state equations are normalized to Γ and we take $\Gamma = 1$. We take the relaxation rate $\gamma = 0.03 \Gamma$, detunings $\Delta_{13}^A = \Delta_{14}^C = 0$, $\Delta_{23}^B = \Delta_{24}^D = -\Delta_{12}$ and Rabi frequencies $\Omega_{13}^A = \Omega_{13}^C = 0.05 \Gamma$, $\Omega_{14}^A = \Omega_{14}^C = 0.055 \Gamma$, $\Omega_{23}^B = \Omega_{23}^D = 0.01 \Gamma$, $\Omega_{24}^B = \Omega_{24}^D = 0.011 \Gamma$. We take all lasers' initial phase equal to 0.

yields the new set of modified OBEs which we use to describe the interaction of lasers with a two-fold coupled double- Λ atomic scheme. The explicitly written system of modified OBEs will be published elsewhere.

The system of modified OBEs has 32 equations with 32 unknowns, 16 + 12 from the rhs of equations (2) and (4) (with corresponding complex-conjugates) and four are populations. It also introduces new quantities, modified Rabi frequencies Ω_{ij}^K and detunings Δ_{ij}^K , where i and j refer to levels and K stands for a laser. From figure 1 we see that for lasers $K = A, C$, possible values for (i, j) are $(1, 3)$ or $(1, 4)$, while for the lasers $K = B, D$, one can have $(i, j) = (2, 3)$ or $(2, 4)$. The Rabi frequencies are given by $\Omega_{ij}^K = \mu_{ij} E_K / \hbar$, where μ_{ij} are dipole moments of the $|i\rangle \rightarrow |j\rangle$ transitions and E_K are complex amplitudes of the lasers' K electric fields. One-photon lasers' detunings are defined as $\Delta_{ij}^K = \omega_K + \omega_i - \omega_j$, where $\hbar\omega_1, \dots, \hbar\omega_4$ are energies of the four atomic states. The two-photon ground and excited detunings, which follow from the multi-photon resonance condition given by equation (3), are also introduced:

$$\begin{aligned}\Delta_{12} &\equiv \Delta_{14}^C - \Delta_{24}^D = \Delta_{13}^C - \Delta_{23}^D, \\ \Delta_{34} &\equiv \Delta_{14}^C - \Delta_{13}^A = \Delta_{24}^D - \Delta_{23}^B.\end{aligned}\quad (5)$$

3. Results and discussion

In figure 2, we compare the results for the absorption of laser B for the single- and two-fold coupled double- Λ for different values of the energy difference between excited levels. Results are presented for the steady-state regime. The laser's B absorption is given as a function of the two-photon ground detuning Δ_{12} . For single-fold coupled double- Λ we calculate it as $N \text{Im}(\Omega_B \rho_{23})$ and for two-fold as $N \text{Im}(\rho_{23}^B \Omega_{23}^B + \rho_{24}^B \Omega_{24}^B)$. The constant N stands for the atomic concentration, and is irrelevant in this study, i.e. we take $N = 1$. Absorption of laser B for the two-fold coupled states exhibits two one-photon absorption profiles, one corresponding to the $2 \rightarrow 3$ and another to the $2 \rightarrow 4$ transition. From figure 2 we also see that both of these profiles show superimposed narrow electromagnetically induced transparency resonances.

If the energy splitting between excited levels, $\Delta\omega_E = \omega_4 - \omega_3$, is large enough, laser B cannot drive transitions to both excited states. Under such an assumption solutions of

equations for the two-fold case should downgrade to standard single-connected, for values of Δ_{12} around 0 where the single-coupled laser's B absorption shows. Results presented in figure 2 clearly show that an increase of $\Delta\omega_E$ leads to identical results between single- and two-fold double- Λ OBEs (compare red and black curves in figure 2 for values of Δ_{12} around 0).

Numerically, with an increase of $\Delta\omega_E$, the new set of variables reduces to the density matrix elements of the single-fold coupled double- Λ interaction scheme. Optical coherences connecting states coupled by the more detuned lasers tend to zero, while others tend to their counterparts for the single-connected equations. For example, the influence of the laser B on the transition $2 \rightarrow 4$ cannot be neglected for small enough $\Delta\omega_E$, as is obvious from figure 2 for values of Δ_{12} around 0. As $\Delta\omega_E$ increases, density matrix element $\tilde{\rho}_{24}^B$ tends to zero, $\tilde{\rho}_{24}^B \rightarrow 0$, while $\tilde{\rho}_{23}^B$ approaches the density matrix element of the single-fold coupled double- Λ , $\tilde{\rho}_{23}^B \rightarrow \tilde{\rho}_{23}$.

In conclusion, we studied the interaction of the two-fold coupled double- Λ with four lasers. Our results show that modified OBEs, which we use to treat this interaction scheme,

have the expected properties. The laser's absorption shows two one-photon absorption profiles corresponding to both couplings. Also, numerical solutions of modified OBEs have the correct limit to the solutions with single-fold excitations as the energy difference between excited levels increases.

Acknowledgment

This work was supported by the Ministry of Education and Science of the Republic of Serbia under grant number III 45016.

References

- [1] Stacey D N *et al* 2008 *J. Phys. B: At. Mol. Opt. Phys.* **41** 085502
- [2] Arimondo E 1996 *Prog. Opt.* **35** 257
- [3] Harris S E 1997 *Phys. Today* **50** 36
- [4] Akulshin A M, Barreiro S and Lezama A 1998 *Phys. Rev. A* **57** 2996
- [5] Gorshkov A V, André A, Lukin M and Sørensen S 2007 *Phys. Rev. A* **76** 033805
- [6] Korsunsky E A and Kosachov D V 1999 *Phys. Rev. A* **60** 4996

Simple analytical expressions for the analysis of the phase-dependent electromagnetically induced transparency in a double- Λ atomic scheme

This content has been downloaded from IOPscience. Please scroll down to see the full text.

2012 Phys. Scr. 2012 014007

(<http://iopscience.iop.org/1402-4896/2012/T149/014007>)

View [the table of contents for this issue](#), or go to the [journal homepage](#) for more

Download details:

IP Address: 147.91.1.41

This content was downloaded on 10/11/2016 at 16:27

Please note that [terms and conditions apply](#).

You may also be interested in:

[Comparison of a double- atomic scheme with single- and two-fold coupled transitions](#)

D Arsenovi and J Dimitrijevi

[Coherent processes in electromagnetically induced absorption: a steady and transient study](#)

J Dimitrijevi, D Arsenovi and B M Jelenkovi

[Phase control of cross-phase modulation with EIT](#)

Hui Sun, Yueping Niu, Shiqi Jin et al.

[Effects of laser beam diameter on electromagnetically induced transparency due to Zeeman coherences in Rb vapor](#)

S N Nikoli, A J Krmpot, N M Lui et al.

[Statistical properties of macroscopic laser fields after coherent interaction with an atomic vapour](#)

Carlos L Garrido Alzar, Luciano S da Cruz, José G Aguirre Gómez et al.

[Transparency and spontaneous emission in a densely doped photonic band gap material](#)

Mahi R Singh

[A study of the ac Stark effect in doped photonic crystals](#)

I Haque and Mahi R Singh

Simple analytical expressions for the analysis of the phase-dependent electromagnetically induced transparency in a double- Λ atomic scheme

J Dimitrijević and D Arsenović

Institute of Physics, University of Belgrade, Pregrevica 118, 10080 Belgrade, Serbia

E-mail: jelena.dimitrijevic@ipb.ac.rs

Received 7 September 2011

Accepted for publication 23 November 2011

Published 27 April 2012

Online at stacks.iop.org/PhysScr/T149/014007

Abstract

We study a double- Λ atomic scheme that interacts with four laser light beams so that a closed loop of radiation-induced transitions is formed. When specific relations for field phases, frequencies and amplitudes are satisfied, coherent superpositions (the so-called ‘dark states’) can be formed in a double- Λ , which leads to the well-known effect of electromagnetically induced transparency (EIT). If the interaction scheme in a double- Λ system is such that a closed loop is formed, the relative phase of the laser light fields becomes very important. We analyze here the effect of the lasers’ relative phase on the EIT in double- Λ configuration of levels. The theoretical study of interactions of lasers with a double- Λ atomic scheme is commonly conducted by solving the optical Bloch equations (OBEs). We use here a perturbative method for solving OBEs, where the interaction of lasers with double- Λ is considered a perturbation. An advantage of the perturbative method is that it generally produces simpler solutions, and analytical expressions can be obtained. We present analytical expressions for the lower-order corrections of the EIT signal. Our results show that the EIT by the perturbative method can be approximated by the sum of products of complex Lorentzians. Through these expressions, we see in what way the relative phase affects the overall EIT profile.

PACS numbers: 42.50.Gy, 42.50.Md, 42.50.Ar

(Some figures may appear in colour only in the online journal)

1. Introduction

Coherent effects in various excitation schemes have attracted much attention in recent decades. One of the most widely investigated effect is electromagnetically induced transparency (EIT) [1]. It has been indicated that in a closed-loop interaction scheme both the dynamics and steady state of EIT strongly depend on the lasers’ relative phase [2, 3]. One of the most widely investigated closed-loop interaction schemes is double- Λ (see figure 1). Besides with EIT [4], it has been studied also in the context of phenomena such as four-wave mixing [5], lasers without inversion [6], slow light [7], quantum correlations [8] and so on.

The phase dependence of EIT in a double- Λ was demonstrated experimentally by Korsunsky and Kosachiov and a theoretical analysis was also presented [3]. Transient properties of phase-dependent EIT were studied in [9]. Applications were also achieved, for example, the creation of entanglement [10] and quantum-state transfer [11]. In this paper, we present a theoretical analysis of the phase-dependent EIT in a double- Λ atomic scheme by using the perturbative method.

2. The model

We solve the steady-state optical Bloch equations (OBEs)

$$\frac{i}{\hbar}[\hat{H}_0, \hat{\rho}] + \frac{i}{\hbar}[\hat{H}_1, \hat{\rho}] + \hat{S}E\hat{\rho} + \gamma\hat{\rho} = \gamma\hat{\rho}_0 \quad (1)$$

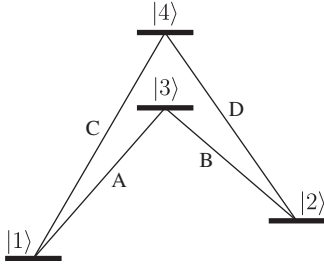


Figure 1. Double- Λ configuration of levels. The four laser light fields A , B , C and D couple states as indicated in the figure.

for the double- Λ interaction scheme given in figure 1. In equation (1), \hat{H}_0 is the Hamiltonian of the free double- Λ atom, \hat{H}_I describes the interaction with lasers and $\hat{S}\hat{E}$ is the abbreviated spontaneous emission operator with the rate Γ for both excited levels. The term $\gamma \hat{\rho}$ describes the relaxation of all density matrix elements due to the atom's finite time of flight through the laser beam and $\gamma \hat{\rho}_0$ describes the flux of atoms to the laser beam, with equal population of two ground-state levels. The detailed system of OBEs for the four-level atom is given in appendix A.

The Rabi frequencies are Ω_K and the lasers' light detunings from the corresponding atomic frequencies are Δ_K , where K stands for a laser A , B , C or D , as shown in figure 1. Detuning between ground levels 1 and 2 is $\Delta_R \equiv \Delta_A - \Delta_B = \Delta_C - \Delta_D$ and between excited levels is $\Delta_E \equiv \Delta_C - \Delta_A = \Delta_D - \Delta_B$. The relative, constant phase between lasers is $\Phi = (\varphi_A - \varphi_B) - (\varphi_C - \varphi_D)$, where φ_K are the lasers' phases.

The details of the perturbative method are described in [12]. We here apply a perturbative method to the system of four lasers interacting with a four-level atom, where the interaction with all four lasers is taken to be a perturbation, i.e. the sum on the rhs of equation (A.1). The solution of the density matrix (elements of which are sorted in a column x) by the perturbative method represents the sum of the unperturbed part x_0 and the series of successive corrections x_n , where n is the iteration number.

3. Results and discussion

The solution obtained by the perturbative method is such that the first appearance of narrow resonances is in the second correction of the density matrix and that only elements which show such behavior are ground-level coherences $\rho_{12}^{x_2}$ and $\rho_{21}^{x_2}$. The analytical expression for $\rho_{21}^{x_2}$ is

$$\rho_{21}^{x_2}(\Delta_R) = -\frac{2(2\gamma + \Gamma - i\Delta_R)}{\gamma - i\Delta_R} \times \left[\frac{e^{-i(\varphi_A - \varphi_B)} \Omega_A \Omega_B}{(2\gamma + \Gamma - 2i\Delta_A)(2\gamma + \Gamma + 2i\Delta_A - 2i\Delta_R)} + \frac{e^{-i(\varphi_C - \varphi_D)} \Omega_C \Omega_D}{(2\gamma + \Gamma - 2i\Delta_C)(2\gamma + \Gamma + 2i\Delta_C - 2i\Delta_R)} \right] \quad (2)$$

and $\rho_{12}^{x_2}$ is the complex conjugate. The rhs of equation (2) represents the sum of products of complex Lorentzians (CL),

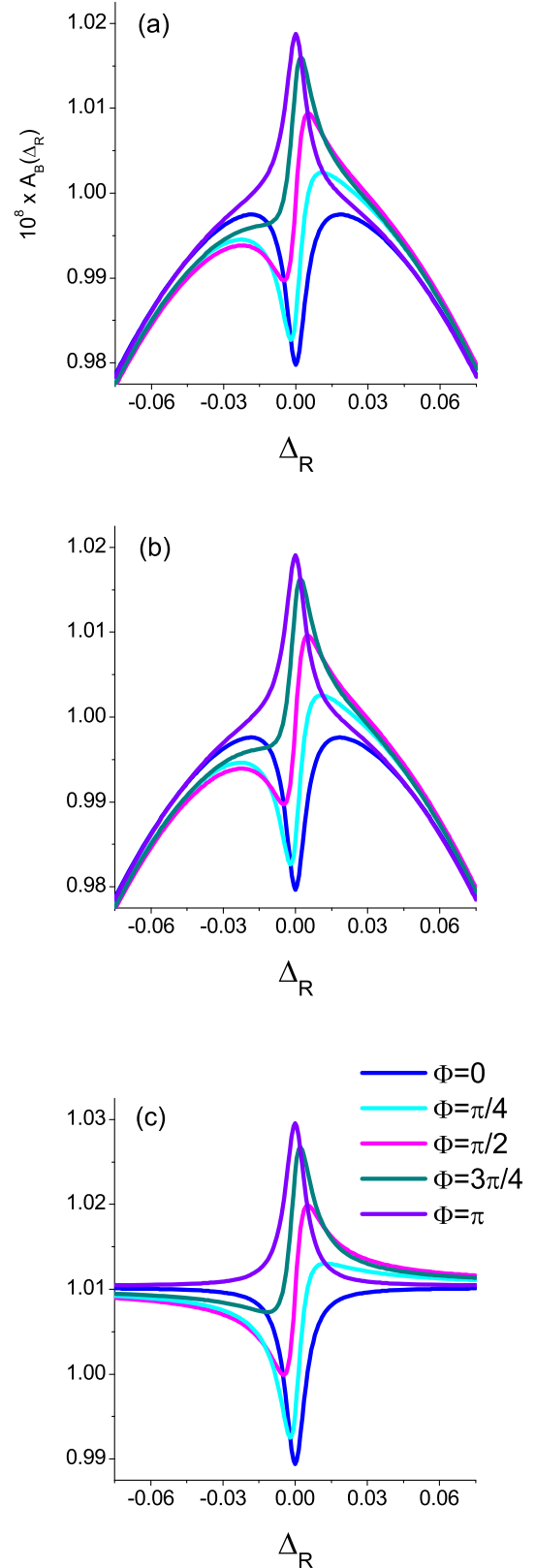


Figure 2. Numerical results for the calculated $A_B(\Delta_R)$ for five different values of the overall phase Φ : (a) the exact solution, (b) the perturbative solution $A_B^{x_1+x_3}(\Delta_R)$ and (c) the approximative expression for $A_B^{x_1+x_3}(\Delta_R)$ given by equation (4). The results are for steady-state OBEs. Equations (parameters) are normalized with Γ , i.e. we take $\Gamma = 1$. We take the relaxation rate $\gamma = 0.005 \Gamma$, the Rabi frequencies $\Omega_A = 0.001 \Gamma$, $\Omega_B = 0.0001 \Gamma$, $\Omega_C = 0.005 \Gamma$ and $\Omega_D = 0.0005 \Gamma$, detunings Δ_A, Δ_C are equal to zero, while we vary $\Delta_R = -\Delta_B = -\Delta_D$ around 0.

where terms within square brackets in equation (2) contain very wide CLs (since $\Gamma \gg \gamma$ and $\Gamma \gg \Delta_{A,B,C,D}$) and each can be approximated with $\frac{1}{\Gamma}$. This yields a simple analytical expression for $\rho_{21}^{x_2}$ in the form of one very narrow CL:

$$\rho_{21}^{x_2}(\Delta_R) \cong n\text{CL}(\Delta_R) = -2 \frac{e^{-i(\varphi_A - \varphi_B)} \Omega_A \Omega_B + e^{-i(\varphi_C - \varphi_D)} \Omega_C \Omega_D}{(\gamma - i\Delta_R)\Gamma}. \quad (3)$$

These two narrow resonances (identified as the real part of $n\text{CL}(\Delta_R)$) are, by the iterative procedure, transferred to all higher-order corrections and lead in the end to the development of EIT.

In figure 2, we present the results for the steady-state, phase-dependent EIT in a double- Λ configuration. As a spectroscopic signal we take the dependence of the laser's B the absorption on the detuning Δ_R . It is calculated as the imaginary part of linear susceptibility, i.e. absorption coefficient, $A_B = N \text{Im}(e^{-i\varphi_B} \Omega_B \rho_{23})$. The constant N stands for the atomic concentration, and is irrelevant in this study, i.e. we take $N = 1$.

The results of the perturbative method show that the narrow EIT resonance appears after including higher-order ($n \geq 3$) corrections of ρ_{23} . From figures 2(a) and (b), we see that already the sum up to the third correction of A_B (or ρ_{23}) shows numerically good agreement with the exact numerical solution obtained by solving OBEs. The analytical expression for the $\rho_{23}^{x_1+x_3}$ is just too long and we do not present it here. Approximating again wide CLs with $\frac{1}{\Gamma}$ yields the following expression for the absorption of laser B :

$$\begin{aligned} A_B^{x_1+x_3}(\Delta_R) \cong & \times \text{Im} \left[-\frac{4i(\Omega_A^2 \Omega_B^2 + \Omega_B^2 \Omega_D^2 + \Omega_B^4 + e^{i\Phi} \Omega_A \Omega_B \Omega_C \Omega_D)}{\Gamma^3} \right. \\ & + \frac{i\Omega_B^2}{\Gamma} - \frac{2i \Omega_B^2 (-\Omega_A^2 + \Omega_B^2 - \Omega_C^2 + \Omega_D^2)}{\gamma \Gamma^2} \\ & \left. - \frac{4i(\Omega_A^2 \Omega_B^2 + e^{i\Phi} \Omega_A \Omega_B \Omega_C \Omega_D)}{\Gamma^2(\gamma - i\Delta_R)} \right], \end{aligned} \quad (4)$$

where only the last term on the rhs of equation (4) depends on Δ_R and others are constant. This term represents the sum of two CLs (up to the constant equal to the narrow resonance given by equation (3)) and can be of opposite sign. One of these CLs is phase independent and the other has $e^{i\Phi}$ as a multiplicative factor. Summing these two resonances yields different profiles, which can, for some values of relative phase Φ , completely change the sign of resonance. For comparison, numerical results for the expression given by equation (4) are shown in figure 2(c).

In conclusion, we have used the perturbative method to analyze phase-dependent EIT in a double- Λ atomic scheme. We have obtained a simple expression for the laser's absorption signal, i.e. the sum of two CLs which can (up to the constant) simulate the variation of EIT with the change of the lasers' relative phase.

Acknowledgment

This work was supported by the Ministry of Education and Science of the Republic of Serbia under grant number III 45016.

Appendix. Optical Bloch equations

OBEs for elements of the density matrix ρ describing the interacting four-level atom can be written as

$$\begin{aligned} \dot{\rho}_{ij} = & i \sum_k (\rho_{ik} R_{kj} - R_{ik} \rho_{kj}) + i D_{ij} \rho_{ij} + G_{ij} \\ & - \gamma \rho_{ij} + \frac{\gamma}{2} \delta_{ij} (\delta_{i1} + \delta_{i2}), \quad i, j = 1, 2, 3, 4. \end{aligned} \quad (A.1)$$

The notation of levels is as in figure 1. Matrices R , D and G describe certain terms of equation (1). Spontaneous emission is given through matrix G :

$$G = \Gamma \begin{pmatrix} \frac{1}{2}(\rho_{33} + \rho_{44}) & 0 & -\frac{1}{2}\rho_{1,3} & -\frac{1}{2}\rho_{1,4} \\ 0 & \frac{1}{2}(\rho_{33} + \rho_{44}) & -\frac{1}{2}\rho_{2,3} & -\frac{1}{2}\rho_{2,4} \\ -\frac{1}{2}\rho_{3,1} & -\frac{1}{2}\rho_{3,2} & -\rho_{3,3} & -\rho_{3,4} \\ -\frac{1}{2}\rho_{4,1} & -\frac{1}{2}\rho_{4,2} & -\rho_{4,3} & -\rho_{4,4} \end{pmatrix},$$

the elements of matrix D are detunings of lasers from the corresponding atomic frequencies:

$$D = \begin{pmatrix} 0 & -\Delta_R & -\Delta_A & -\Delta_C \\ \Delta_R & 0 & -\Delta_B & -\Delta_D \\ \Delta_A & \Delta_B & 0 & -\Delta_E \\ \Delta_C & \Delta_D & \Delta_E & 0 \end{pmatrix}$$

and R is a matrix with Rabi frequencies describing the interaction part of the Liouville equation

$$R = \begin{pmatrix} 0 & 0 & e^{i\varphi_A} \Omega_A & e^{i\varphi_C} \Omega_C \\ 0 & 0 & e^{i\varphi_B} \Omega_B & e^{i\varphi_D} \Omega_D \\ e^{-i\varphi_A} \Omega_A & e^{-i\varphi_B} \Omega_B & 0 & 0 \\ e^{-i\varphi_C} \Omega_C & e^{-i\varphi_D} \Omega_D & 0 & 0 \end{pmatrix}.$$

References

- [1] Harris S E 1997 *Phys. Today* **50** 36
- [2] Korsunsky E A, Leinfellner N, Huss A, Balushev S and Windholz L 1999 *Phys. Rev. A* **59** 2302
- [3] Korsunsky E A and Kosachiov D V 1999 *Phys. Rev. A* **60** 4996
- [4] Shpaisman H, Wilson-Gordon A D and Friedmann H 2005 *Phys. Rev. A* **71** 043812
- [5] Lü B, Burkett W H and Xiao M 1998 *Opt. Lett.* **23** 804
- [6] Kocharovskaya O, Li R-D and Mandel P 1990 *Opt. Commun.* **77** 215
- [7] Boyer V, McCormick C F, Arimondo E and Lett P D 2007 *Phys. Rev. Lett.* **99** 143601
- [8] McCormick C F, Marino A M, Boyer V and Lett P D 2008 *Phys. Rev. A* **78** 043816
- [9] Maichen W, Renzoni F, Mazets I, Korsunsky E and Windholz L 1996 *Phys. Rev. A* **53** 3444
- [10] Wang F, Hu X, Shi W and Zhu Y 2010 *Phys. Rev. A* **81** 033836
- [11] Liu X-J, Jing H, Zhou X-T and Ge M-L 2004 *Phys. Rev. A* **70** 015603
- [12] Dimitrijević J, Arsenović D and Jelenković B M 2011 *New J. Phys.* **13** 033010

Pulse propagation dynamics in the presence of a continuous-wave field

This content has been downloaded from IOPscience. Please scroll down to see the full text.

2013 Phys. Scr. 2013 014011

(<http://iopscience.iop.org/1402-4896/2013/T157/014011>)

View [the table of contents for this issue](#), or go to the [journal homepage](#) for more

Download details:

IP Address: 147.91.1.42

This content was downloaded on 08/07/2014 at 12:17

Please note that [terms and conditions apply](#).

Pulse propagation dynamics in the presence of a continuous-wave field

Jelena Dimitrijević, Dušan Arsenović and Branislav M Jelenković

Institute of Physics, University of Belgrade, Pregrevica 118, 10080 Belgrade, Serbia

E-mail: jelena.dimitrijevic@ipb.ac.rs

Received 20 August 2012

Accepted for publication 18 December 2012

Published 15 November 2013

Online at stacks.iop.org/PhysScr/T157/014011

Abstract

We present theoretical results for the propagation dynamics of an electromagnetic field pulse through rubidium vapor, while another field, a continuous-wave electromagnetic field, is present. The frequencies of both electromagnetic fields are resonant with the transition between the ground and excited state hyperfine levels of Rb, $F_g \rightarrow F_e = F_g \pm 1$. Detuning from resonance is done by the magnetic field oriented along the light propagation direction (Hanle configuration). When both the electromagnetic fields are simultaneously interacting with Rb atoms, either electromagnetically induced transparency or absorption is induced. Propagation dynamics was obtained solving the set of Maxwell–Bloch equations for the interacting atoms with two electromagnetic fields. Motivated by recent results (Brazhnikov *et al* 2011 *Eur. Phys. J. D* **63** 315–25; Brazhnikov *et al* 2010 *JETP Lett.* **91** 625–9; Kou *et al* 2011 *Phys. Rev. A* **84** 063807), we have analyzed the influence of experimental parameters, laser polarization, and mutual phases between lasers, which can lead to optical switching, i.e. the transformation from electromagnetically induced absorption to transparency and vice versa.

PACS numbers: 42.50.Gy, 42.50.Nn

(Some figures may appear in color only in the online journal)

1. Introduction

Laser–atom interactions, which can develop coherent phenomena in atoms, electromagnetically induced transmission (EIT) [1] and absorption (EIA) [2] in alkali atoms, have attracted a great deal of interest in recent decades because of the important applications of both the phenomena. For such coherences to develop, lasers have to couple the long-lived ground state hyperfine level(s) with the excited hyperfine level(s) of alkali atoms. Narrow EIT and EIA resonances and steep dispersion in the narrow spectral bandwidth of the resonances are the unique properties of atomic systems in which the propagation of laser pulses can be considerably slowed or completely blocked [6–8]. Studying the dynamics of laser pulses in coherent media is of interest for all optical switchings [9, 10], squeezed light [11], quantum information science, etc.

Different atomic schemes can be applied in order to induce EIT or EIA. This can be the pump–probe configuration when two lasers couple two hyperfine (or two Zeeman) levels with the common excited hyperfine level in either Λ (two

levels belong to the ground state) or V (levels belong to the excited state) atomic schemes. In the Hanle configuration, a single laser couples Zeeman sublevels of hyperfine levels of alkali atoms. Raman detuning in the latter case is done by applying a proper magnetic field.

In this paper, we analyze the mutual effects of two laser fields on their propagation, when both the laser fields induce simultaneously either EIT or EIA in the Rb vapor. The specific case when one laser is continuous wave (CW) and the other is pulsed is analyzed. We show how lasers' coherent interactions can be manipulated by appropriately changing the mutual orientation of their polarization vectors and their relative phases. So far, very little has been done to investigate the mutual effects of propagation of a laser pulse in a coherently prepared medium when a CW laser, which makes the preparation, is present.

2. Theoretical model

We solve the set of Maxwell–Bloch equations (MBEs) for the interaction of two lasers, one of which is pulsed and

the other is CW, with Rb atoms. The frequencies of both lasers are adjusted to either $F_g = 2 \rightarrow F_e = 3$ or $F_g = 2 \rightarrow F_e = 1$ transition, where we solve MBEs for the full atomic systems of both transitions, i.e. for all Zeeman sublevels. The parameters for the transitions in Rb, used in calculations, were taken from [12, 13]. The evolution of the density matrix $\hat{\rho}$ is calculated from the optical Bloch equations

$$\frac{d\hat{\rho}(t)}{dt} = -\frac{i}{\hbar}[\hat{H}_0, \hat{\rho}(t)] - \frac{i}{\hbar}[\hat{H}_1, \hat{\rho}(t)] - \hat{S}\hat{E}\hat{\rho}(t) - \gamma\hat{\rho}(t) + \gamma\hat{\rho}_0. \quad (1)$$

Diagonal elements of $\hat{\rho}$, ρ_{g_i, g_i} and ρ_{e_i, e_i} are populations, ρ_{g_i, g_j} and ρ_{e_i, e_j} are Zeeman coherences and ρ_{g_i, e_j} and ρ_{e_i, g_j} are optical coherences, where indices g and e stand for the ground and excited sublevels.

We solve MBEs for different values of the magnetic field B_s , as described by the Hamiltonian \hat{H}_0 . The quantization axis is chosen parallel to the direction of the magnetic field \mathbf{B}_s , which is also the direction along which the lasers propagate. The energies due to the Zeeman splitting are given by $E_{g(e)} = \mu_B l_{F_{g(e)}} m_{g(e)} B_s$, where $m_{g(e)}$ are the magnetic quantum numbers of the ground and excited sublevels, μ_B is the Bohr magneton and $l_{F_{g(e)}}$ is the Landé gyromagnetic factor for two hyperfine levels. $\hat{S}\hat{E}$ stands for the abbreviated spontaneous emission operator with the rate Γ . The relaxation of all density matrix elements, due to the finite time for an atom to cross the laser beam, is given by the term $\gamma\hat{\rho}$, while $\gamma\hat{\rho}_0$ takes into account the continuous flux of atoms entering laser beams with equal population of the ground Zeeman sublevels. The role of laser detuning (and Doppler broadening) is not discussed here.

\hat{H}_1 is the interaction Hamiltonian describing the coherent interaction of the laser fields with atoms. The electric field vector represents the sum of two electric fields:

$$\vec{E}(t, z) = \sum_l [E_x^l \cos(\omega^l t - k^l z + \varphi_x^l) \vec{e}_x + E_y^l \cos(\omega^l t - k^l z + \varphi_y^l) \vec{e}_y], \quad (2)$$

where $l = 1, 2$ stands for the pulsed and CW lasers. E^l are the amplitudes of two fields, ω^l are their angular frequencies, $\omega^l = \pm c k^l$, and c is the speed of light. k^l are lasers' wave vectors, where we take $k^l > 0$ for the propagation along the positive direction of the z -axis. In equation (2), E_x^l, E_y^l are the real Descartes components of the amplitude of the electric field and φ_x^l, φ_y^l are the associated phases, also real quantities. The electric field vector can further be written as

$$\vec{E}(t, z) = \sum_l [e^{i(\omega^l t - k^l z)} \vec{u}_{+1} E_{++}^l + e^{i(\omega^l t - k^l z)} \vec{u}_{-1} E_{--}^l + e^{-i(\omega^l t - k^l z)} \vec{u}_{+1} E_{+-}^l + e^{-i(\omega^l t - k^l z)} \vec{u}_{-1} E_{-+}^l], \quad (3)$$

where the following substitution has been introduced:

$$E_{++}^l = \frac{-E_x^l e^{+i\varphi_x^l} + iE_y^l e^{+i\varphi_y^l}}{2\sqrt{2}}, \quad E_{+-}^l = \frac{-E_x^l e^{-i\varphi_x^l} + iE_y^l e^{-i\varphi_y^l}}{2\sqrt{2}}, \\ E_{-+}^l = \frac{E_x^l e^{+i\varphi_x^l} + iE_y^l e^{+i\varphi_y^l}}{2\sqrt{2}}, \quad E_{--}^l = \frac{E_x^l e^{-i\varphi_x^l} + iE_y^l e^{-i\varphi_y^l}}{2\sqrt{2}}. \quad (4)$$

In equation (4), $E_{++}^l, E_{+-}^l, E_{-+}^l, E_{--}^l$ are the complex amplitudes of the fields and the relation $(E_{++}^l)^* = -E_{--}^l, (E_{+-}^l)^* = -E_{-+}^l$ stands.

The usual substitution for the optical coherences

$$\rho_{g_i, e_j} = \sum_l e^{i(\omega^l t - k^l z)} \tilde{\rho}_{g_i, e_j}^l, \quad \rho_{e_i, g_j} = \sum_l e^{-i(\omega^l t - k^l z)} \tilde{\rho}_{e_i, g_j}^l \quad (5)$$

has been introduced, where the sum is taken over lasers that couple states g_i and e_j . This substitution means that we are working in line with the multi-mode Floquet theory [14] for the case of counter-propagating lasers, or with the single-mode one for the case of lasers with the same frequency. We use the approximation with the zeroth-order harmonics for the ground-state and the excited-state density matrix elements and up to the first-order harmonics for the optical coherences.

The propagation dynamics of the electric-field amplitudes, for the propagation along the positive direction of the z -axis, is given by MBEs:

$$\left(\frac{\partial}{\partial z} + \frac{1}{c} \frac{\partial}{\partial t}\right) E_{\pm+}^l = -i \frac{k^l N_c}{2\varepsilon_0} P_{\pm+}^l, \\ \left(\frac{\partial}{\partial z} + \frac{1}{c} \frac{\partial}{\partial t}\right) E_{\pm-}^l = +i \frac{k^l N_c}{2\varepsilon_0} P_{\pm-}^l \quad (6)$$

and for the propagation along the negative direction of the z -axis, MBEs stand:

$$\left(-\frac{\partial}{\partial z} + \frac{1}{c} \frac{\partial}{\partial t}\right) E_{\pm+}^l = -i \frac{k^l N_c}{2\varepsilon_0} P_{\pm+}^l, \\ \left(-\frac{\partial}{\partial z} + \frac{1}{c} \frac{\partial}{\partial t}\right) E_{\pm-}^l = +i \frac{k^l N_c}{2\varepsilon_0} P_{\pm-}^l. \quad (7)$$

In equations (6) and (7), new quantities were introduced which are calculated as

$$P_{++}^l = \sum_{g_i \leftrightarrow e_j} \tilde{\rho}_{g_i, e_j}^l \mu_{g_i, e_j, +1}, \quad P_{+-}^l = \sum_{e_i \leftrightarrow g_j} \tilde{\rho}_{e_i, g_j}^l \mu_{g_i, e_j, +1}, \\ P_{-+}^l = \sum_{g_i \leftrightarrow e_j} \tilde{\rho}_{g_i, e_j}^l \mu_{g_i, e_j, -1}, \quad P_{--}^l = \sum_{e_i \leftrightarrow g_j} \tilde{\rho}_{e_i, g_j}^l \mu_{g_i, e_j, -1}, \quad (8)$$

where the sum is taken over the dipole-allowed transitions induced by lasers. These four variables appear in the components of macroscopic polarization of the atomic medium which is calculated as $\vec{P}(t, z) = N_c e \text{Tr}[\hat{\rho} \hat{\vec{r}}]$ or

$$\vec{P}(t, z) = N_c \sum_l [e^{i(\omega^l t - k^l z)} (\vec{u}_{+1} P_{++}^l + \vec{u}_{-1} P_{-+}^l) + e^{-i(\omega^l t - k^l z)} (\vec{u}_{+1} P_{+-}^l + \vec{u}_{-1} P_{--}^l)]. \quad (9)$$

3. Results and discussion

3.1. Effect of the polarization of two laser fields

We present the results for the propagation dynamics of two lasers propagating through the Rb vapor. One is the CW laser, another is the pulsed laser and both couple the same Rb transition. Recent results [3, 4] showed that, for the two counter-propagating CW fields, it is possible to reverse

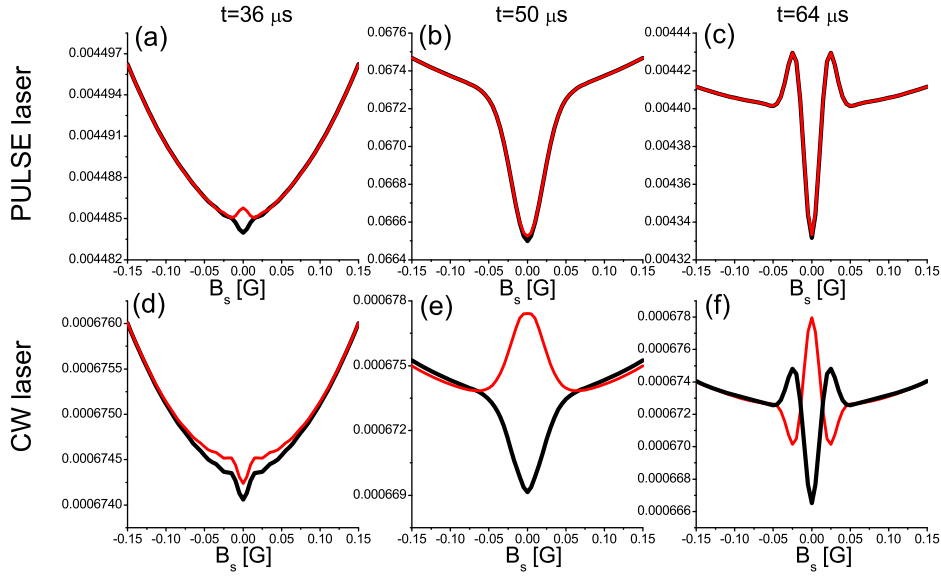


Figure 1. Transmission of the pulse (top row) and the CW laser (bottom row) for three different moments: $t = 36 \mu\text{s}$ (a, d), $t = 50 \mu\text{s}$ (b, e) and $t = 64 \mu\text{s}$ (c, f). Black curves show the results when the polarization vectors of both lasers are parallel, $\theta_{\text{CW}} = 0$, and red curves show transmissions when the polarization vector of the CW field is rotated, $\theta_{\text{CW}} = \frac{\pi}{2}$.

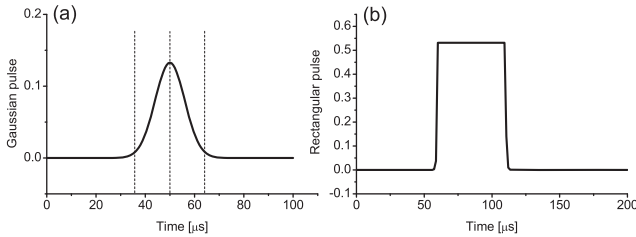


Figure 2. Waveforms of laser pulses used in the calculations: a Gaussian pulse (a) and a rectangular pulse (b). Dashed vertical lines in panel (a) indicate moments for which we present the results in figure 1.

the sign of the resonance by a purely polarization method. They performed numerical and analytical calculations for the simple three-level schemes. Both lasers couple the $F_g = 2 \rightarrow F_e = 3$ transition in ^{87}Rb , and each can independently induce EIA in the vapor. We analyze how the counter-propagating pulse affects the properties of a CW laser, and the other way around, how the existence of the CW laser changes the properties of the propagating laser pulse. Transmissions of lasers are calculated for values of the external magnetic field near zero, i.e. around the EIA resonance. Calculations were performed by solving the set of MBEs (see section 2) for the same transition. Both lasers are linearly polarized, and we study the effects of different angles between their polarization vectors on the propagation of both lasers.

In figure 1, we present the transmissions of both lasers for two different values of the angle of rotation of the CW laser polarization vector (θ_{CW}). The temporal shape of the pulse is Gaussian $I_{\text{pulse}}^0 e^{-\frac{(t-t_0)^2}{\sigma^2}}$ (see figure 2(a)), where $\sigma = 10 \mu\text{s}/\sqrt{2 \ln 2}$. The intensity of the laser pulse, at the peak of the amplitude, $t_0 = 50 \mu\text{s}$, is $I_{\text{pulse}}^0 = 1.327 21 \times 10^{-2} \text{ mW cm}^{-2}$. The intensity of the CW laser at the entrance of the cell is $I_{\text{CW}}^0 = 10^{-2} I_{\text{pulse}}^0$. We take the relaxation due to the time of flight to be $\gamma = 0.001 \Gamma$, where $\Gamma = 2\pi \cdot 6.066 62 \times 10^6 \text{ Hz}$ is the spontaneous emission rate. The density of Rb

atoms in the cell is $N_c = 10^{14} \text{ m}^{-3}$ and the length of the cell is 0.1 m . The results in figure 1 are given for three moments of time: when the pulse is entering the cell, $t = 36 \mu\text{s}$, when its peak intensity is in the cell, $t = 50 \mu\text{s}$, and when it is leaving the cell, $t = 64 \mu\text{s}$. The positions of these three moments with respect to the pulse are indicated in figure 2(a) with vertical dashed lines.

When the polarizations of both lasers are parallel, $\theta_{\text{CW}} = 0$ (black curves in figure 1), the transmissions of both lasers show EIA resonances at all instants, as expected for the lasers locked to the $F_g = 2 \rightarrow F_e = 3$ transition. Rotation of the polarization vector of the CW laser by $\pi/2$ yields different transmission profiles of the CW laser. At the time moment $t = 36 \mu\text{s}$, when the pulse starts entering the cell, the transmission of the CW laser is not influenced by the pulse's presence in the cell and shows small EIA for both values of θ_{CW} (see figure 1(d)). As the pulse's intensity increases, the atomic ensemble gets affected by both lasers' fields. Results in figure 1(e) show that at time $t = 50 \mu\text{s}$, due to the rotated polarization of the CW field, the transmission of the CW laser completely changes the sign of resonance from EIA (black curve, $\theta_{\text{CW}} = 0$) to EIT (red curve, $\theta_{\text{CW}} = \frac{\pi}{2}$). Under the simultaneous action of both lasers, depending on the mutual angle between their linear polarizations, the CW laser can change the sign of resonance, allowing our system to act as an optical switch for the CW laser. Specific profiles of the transmissions of both lasers at the time moment $t = 64 \mu\text{s}$ (figures 1(c) and (e)) are due to residual, long-lived coherences, after the pulse's passing through the cell.

The transmission of the pulse laser does not change with θ_{CW} during most of the pulse's passage through the cell (see figures 1(a)–(c)), since with our choice of parameters the pulse's intensity is much larger than that of the CW field, $I_{\text{pulse}}^0 = 10^2 I_{\text{CW}}^0$. The sign reversal in figure 1(a) happens since, at that time instant, the lasers are nearly at the same magnitude of intensity. Results where we present the optical switching of the pulse's transmission will be published elsewhere.

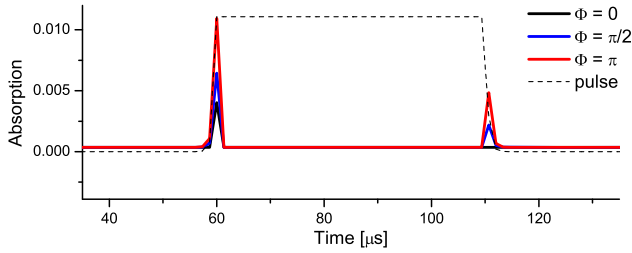


Figure 3. Total absorption of both lasers for three different values of the initial phase of the σ^- component of the pulse laser. The phases of the other three σ components are 0. Given by the dashed line is the waveform of the pulse laser, normalized to the maximum value of absorptions.

3.2. Effect of the relative phase between laser fields

We have analyzed the effects of different initial phases of the two lasers. In the recent analysis by Kou *et al* [5], similar effects were studied, except that they used two pulsed lasers (or four σ components) and MBEs were solved for the simple three-level scheme. In our analysis, we analyze the mutual effects of a linearly polarized pulse and a CW laser. Here we assume that the lasers are co-propagating and are locked to the $F_g = 2 \rightarrow F_e = 1$ transition, thus inducing the dark state and EIT. We solve MBEs for this transition, assuming a single mode for the substitution, given by equation (5), since all σ components have the same frequency. The absorption of the two lasers is calculated as a function of different initial phases of the lasers' σ waves.

We solve MBEs for the CW and the pulse laser assuming a near-rectangular pulse for the pulsed laser (see figure 2(b)). The edges of the pulse are approximated by the exponential rise and fall slopes in order to introduce a more realistic situation:

$$\text{pulse} = \begin{cases} I_{\text{pulse}}^0 e^{-s(t-t_2)}, & t > t_2, \\ e^{s(t-t_1)}, & t > t_1, \\ 1, & t_1 \leq t \leq t_2, \end{cases} \quad (10)$$

where the slope is given by $s = 2 \times 10^6$ Hz, the intensity of the pulse's σ component is $I_{\text{pulse}}^{\sigma 0} = 0.053\,088\,4\text{ mW cm}^{-2}$, and the beginning and the end of the pulse are $t_1 = 60\text{ }\mu\text{s}$ and $t_2 = 110\text{ }\mu\text{s}$, respectively. Relaxation due to the time of flight is taken as $\gamma = 10^{-6}\text{ }\Gamma$, where $\Gamma = 2\pi \times 5.750\,06 \times 10^6$ Hz is the spontaneous emission rate. The concentration of atoms in the cell is $N_c = 10^{14}\text{ m}^{-3}$ and the cell's length is 0.1 m. The intensity of the CW laser's σ components is $I_{\text{CW}}^{\sigma 0} = 10^2 I_{\text{pulse}}^{\sigma 0}$. The results presented here are given for the magnetic field $B = 0$.

In figure 3 we present the total absorption of all four σ components from both lasers, from the time when the pulse laser is applied until the end of the pulse. Results are given for three different values of the initial phase of the σ^- component of the pulse laser (Φ), while the initial phases of other σ components are kept constant. From figure 3, we see that the rapid change of absorptions is happening only during the transient regime when the pulse laser is turned on and off.

In this configuration, the CW laser plays the role of a pumping laser, preparing the atoms into the dark state. Before the pulse laser is turned on, the absorption of the CW laser is nearly zero, due to the EIT. When the pulse laser is

turned on, a new dark state is formed. This leads to a quick change in absorption of laser fields, until a new superposition of atomic levels, this time under the action of both lasers, generates a new dark state for both electromagnetic fields, and consequently the new EIT and minimal absorption. The reverse situation happens when the pulse laser is turned off. The results in figure 3 show that the absorption of two lasers strongly depends on their initial phases. Similarly to Kou *et al* [5], we have shown the considerable phase dependence for the case of a combined pulse and CW laser field.

4. Conclusions

We have theoretically analyzed the propagation dynamics of two laser fields: when the pulse laser enters the Rb cell while another, the CW laser, is present. Both lasers couple the same two hyperfine levels, of the ground and excited states of Rb. We studied the case when both can induce either dark or bright resonances, leading to EIT or EIA. We have shown that, with an appropriate choice of parameters (polarization direction and mutual phases) and geometry (counter and co-propagating lasers), both fields affect each other's behavior while propagating through the Rb vapor. This type of coherent manipulation of atoms can lead to magneto-optical switching techniques or optical-storage devices. Our numerical analysis is applied to the realistic system, that is, the Rb atom, and as such indicates that these phenomena can be observable in realistic experiments by using the alkali-metal atoms.

Acknowledgments

This work was supported by the Ministry of Education, Science and Technological Development of the Republic of Serbia under grant number III 45016.

References

- [1] Arimondo E 1996 *Prog. Opt.* **35** 257–354
- [2] Akulshin A M, Barreiro S and Lezama A 1998 *Phys. Rev. A* **57** 2996
- [3] Brazhnikov D V, Taichenachev A V and Yudin V I 2011 *Eur. Phys. J. D* **63** 315–25
- [4] Brazhnikov D V, Taichenachev A V, Tumaikin A M, Yudin V I, Ryabtsev I I and Entin V M 2010 *JETP Lett.* **91** 625–9
- [5] Kou J, Wan R G, Kang Z H, Jiang L, Wang L, Jiang Y and Gao J Y 2011 *Phys. Rev. A* **84** 063807
- [6] Novikova I, Phillips D F and Walsworth R L 2007 *Phys. Rev. Lett.* **99** 173604
- [7] Okuma J, Hayashi N, Fujisawa A and Mitsunaga M 2009 *Opt. Lett.* **34** 1654–6
- [8] Boyer V, McCormick C F, Arimondo E and Lett P D 2007 *Phys. Rev. Lett.* **99** 143601
- [9] Li J, Yu R, Si L and Yang X 2010 *J. Phys. B: At. Mol. Opt. Phys.* **43** 065502
- [10] Qi Y, Niu Y, Zhou F, Peng Y and Gong S 2011 *J. Phys. B: At. Mol. Opt. Phys.* **44** 085502
- [11] Imad H Agha, Christina Giarmatzis, Quentin Glorieux, Thomas Coudreau, Philippe Grangier and Gaétan Messin 2011 *New J. Phys.* **13** 043030
- [12] Steck D A 2010 Rubidium 85 D, Line Data (<http://steckus/alkalidata>) (revision 2.1.4, 23 December 2010)
- [13] Steck D A 2010 Rubidium 87 D, Line Data (<http://steckus/alkalidata>) (revision 2.1.4, 23 December 2010)
- [14] Chu S I and Telnov D A 2004 *Phys. Rep.* **390** 1–131

Autoresonant Three-Wave-Mixing in Non-Uniform Second-Order Nonlinear Bulk Crystals

Anna Mazhorova, Andrey Markov, Oded Yaakobi,
Matteo Clerici, Daniele Modotto, Ottavia Jedrkiewicz,
Paolo di Trapani, Arkady Major, François Vidal,
and Roberto Morandotti

*Institut national de la recherche scientifique (INRS)
1650 Boulevard Lionel-Boulet J3X 1S2 Varennes, Québec, CANADA
E-mail: anna.mazhorova@gmail.com*

Three-wave-mixing (TWM) in second-order nonlinearity optical crystals, mainly exploited for optical parametric amplification, is a powerful technique to produce widely tunable and high energy ultra-short pulses. TWM inside nonlinear crystals enables conversion to wavelength regions that are not covered by standard laser systems. In order to produce ultra-short pulses, ultra-broad spectral bandwidth generation has been essential. However, the output pulse duration from parametric processes is limited by the spectral acceptance of the phase-matching condition. We demonstrate > 60 % efficient autoresonant three-wave-mixing in non-uniform bulk optical crystals by introducing temperature gradient phase-matching. This novel approach enabled generation of high-energy pulses with > 50 % conversion efficiency over a ~ 150 nm bandwidth.

Atom Localization via Zeeman Coherences in Degenerate Two-Level System

Jelena Dimitrijević, Dušan Arsenović
and Branislav M. Jelenković

*University of Belgrade, Institute of Physics
118 Pregrevica 11080 Belgrade, SERBIA*

E-mail: jelenad@ipb.ac.rs

Results have been presented for the efficient atom subwavelength localization by utilizing coherent phenomena being electromagnetically induced transparency (EIT) and absorption (EIA). The phenomena have been realized by applying external magnetic field on cold atoms and two optical fields, standing-wave and probe field, both resonant with the hyperfine transition in Rb. Different configurations have been analyzed depending on the orientation of magnetic field with respect to the applied optical fields. Numerical results have been obtained by solving Optical Bloch

electroencephalogram in the following regimes has been analyzed: background, syncope, paroxysm, presence of electromagnetic noise radiation. Self-similarity exponent is a quantitative parameter of these influences. To estimate the correctness of application of self-similarity exponent as a EEG characteristic parameter, simultaneously with self-similarity exponent a spectral power density of alpha-, beta-, theta-rhythms for all regimes have been analyzed. A correlation of the spectral power density and the self-similarity exponent has been noticed. The spectral power densities of beta- and theta- rhythms of electroencephalograms in O1-A1 and O2-A2 leadings have been determined. The spectral power densities of alpha-, beta-, theta-rhythms in electroencephalograms in T3-A1 leading have been increased, but in the electroencephalograms in T4-A2 leading have been decreased in the case of electromagnetic noise radiation action. This result may be as consequence of decrease of beta-rhythm and theta-rhythm coherence between the left and right temporal parts of brain. In turn, the decrease of the coherence can be due to consequence of a hidden depression. The increasing of the alpha-rhythm spectral power density of electroencephalograms in O1-A1 and O2-A2 leadings have been noted in the paroxysm and syncope states. This fact, it can possible, signify decreasing of the visual activity in brain. The maximum of theta-rhythm spectral power density indicates on the syncope state. This fact can be a consequence of a deep relaxation.

Frequency Conversion in Nanostructured Lithium Niobate

Frank Setzpfandt

*Friedrich-Schiller-Universität Jena
6 Albert-Einstein-Str. 07745 Jena, GERMANY
E-mail: f.setzpfandt@uni-jena.de*

Due to its strong nonlinearity and large transparency window, lithium niobate is one of the most useful materials for integrated optics. Its favorable properties can be further enhanced by nanostructuring. In this talk I will discuss some of our recent results on parametric frequency-conversion processes in nanostructured lithium niobate waveguides, including second-harmonic generation and spontaneous parametric down-conversion.

equation for multilevel atomic schemes. It has been shown that method enables narrow localization structures with widths less than $0.5\% \lambda$ in the probe field absorption localization pattern. Conditions where one can manipulate both the position and contrast of the localization peaks by applying small magnetic fields have been analyzed. Observed behavior of the probe field absorption has been analyzed through the mutual effects of two optical fields of various strengths, saturation effect and the EIT/EIA dependence on the applied magnetic field.

Stability of CW Solutions in One Model of Semiconductor Laser with Large Delay

Alexandra Kashchenko

*P. G. Demidov Yaroslavl State University,
14 Sovetskaya Str. 150003 Yaroslavl, RUSSIA*

E-mail: sa-ahr@gandax.ru

The problem of existence and stability of CW solutions in one semiconductor laser model (Lang-Kobayashi model with large delay) has been studied. The condition of existence of a family with large number of CW solutions is that "main parts" of solutions must be located on a special set I (depending on all parameters of the model). Sufficient conditions of stability and unstableness of these solutions are found. In the case of a zero linewidth enhancement factor the necessary and sufficient conditions of stability have been found. Location of the stability regions on the sets I has been studied. It has been proved that in the case of the zero line width enhancement factor the number of the stability regions on the set I is less than two.

Optically Induced Channel Waveguides and Diffraction Gratings in Photorefractive Surface Layers of Lithium Niobate with Light Leakage

A. Bezpaly, A. Verkhoturov, and Vladimir Shandarov

*Tomsk State University of Control Systems and Radioelectronics
40 Lenin av. 634050 Tomsk, RUSSIA*

E-mail: ShandarovVM@svch.rk.tusur.ru

Surface doping of dielectric and semiconductor materials allows significant variations of their properties within thin surface layer. It has been studied both, the waveguide and diffraction characteristics of optically induced channel waveguides and planar diffraction gratings within surface

layers of lithium niobate samples doped with photorefractive impurities Fe, and Cu. The channel waveguide structures have been formed by step-by-step exposure of stripe-like areas of the crystal sample Y-surface with focused laser beam. One-dimensional planar diffraction gratings have been induced within doped surface layer using parallel exposure procedure that uses amplitude masks. The laser radiation with wavelengths 450 and 532 nm has been applied to induce these elements. The characteristics of induced elements have been studied with light diffraction methods. The features of light diffraction at its total internal reflection from Y-surface with induced structures have been studied for waveguide and diffraction elements oriented along directions with angles $40 - 50$ degrees with respect to the crystal optical axis. The effect of light leakage brings significant features to the light diffraction characteristics in this configuration.

Second Harmonic Generation in Non-Centrosymmetric Composite Media Doped with Nanocrystals with Large Permanent Dipole Moment

Oleg Khasanov, O. Fedotova, V. Gayvoronsky and I. Pritula

*Scientific-Practical Material Research Centre,
National Academy of Sciences of Belarus
19 Brovki str. 220072 Minsk, BELARUS*

E-mail: olkhas@mail.ru

Second harmonic generation (SHG) in KDP crystals doped with ZnO nanocrystals taking into account large permanent dipole moment of nanoparticles and local field effect depending on their sizes has been analyzed. We consider one- and two-quantum transitions in nanoparticles, electron-hole, exciton-exciton and exciton-plasmon interactions. SHG efficiency as a function of nanoparticle concentration has been estimated.

Output Characteristics of Mixed Transmission Holograms in $\text{Bi}_{12}\text{TiO}_{20}$ Crystal. Theory and Experiment

Vasily V. Shepelevich, A. V. Makarevich and S. M. Shandarov

*Mozyr State Pedagogical University,
Theoretical Physics and Applied Informatics Department
28 Studencheskaya Str. 247760 Mozyr, BELARUS*

E-mail: vasshep@inbox.ru

The analytical solution of the system of differential equations which describes a reconstitution of the subject light wave by a mixed transmission

Evolution of 1D Airy beam propagating through a Zeeman EIT atomic medium

Dušan Arsenović, Jelena Dimitrijević and Branislav M. Jelenković
Institute of Physics, University of Belgrade,
Pregrevica 118, 11080 Belgrade, Serbia
email: arsenovic@ipb.ac.rs

We study propagation of the one-dimensional Airy beam [1] through the atomic medium with electromagnetically induced transparency (EIT) [2]. Maxwell-Bloch equations are solved numerically assuming single continuous-wave laser field resonant to the $F_g=1 \rightarrow F_e=0$ hyperfine atomic transition of the ^{87}Rb D2 line. Presence of the external magnetic field removes the degeneracy of the Zeeman magnetic sublevels, bringing tripod-like atomic scheme. Characteristics of the Airy beam propagation through the EIT medium, slow-light Airy wave-packets and bullets, modulation and deflection of Airy beam, have been recently studied analytically and numerically [3, 4].

Our study analyzes how the response of the atomic medium, with induced Zeeman EIT coherences, influences evolution of the Airy beam propagation for different magnetic fields, inside or out of the EIT transparency window. Results are presented for the Airy beam intensity profile during temporal evolution and also for the deflection of the Airy beam for various propagation distances. Modulation and deformation of the Airy beam, different levels of absorption of the Airy beam lobes, while propagating through the EIT medium, are analyzed through the formation and behavior of the dark-states. Presented results suggest ways of magneto-optical control of the Airy beam and also possible applications in optical design, optical switching, optical information processing etc.

REFERENCES

- [1] Y. Hu, G. A. Siviloglou, P. Zhang, N. K. Efremidis, D. N. Christodoulides, and Z. Chen, in *Nonlinear Photonics and Novel Optical Phenomena*, pp. 1, ed. Z. Chen, R. Morandotti, Springer (2013).
- [2] E. Arimondo, in *Progress in Optics*, vol. 35, pp. 257, ed. E. Wolf, Elsevier (1996).
- [3] C. Hang and G. Huang, *Phys. Rev. A* **88** 013825 (2013).
- [4] F. Zhuang, J. Shen, X. Du, D. Zhao, *Opt. Lett.* **37**(15) 3054 (2012).

One-dimensional sub-wavelength atom localization via Zeeman EIT in a degenerate two-level system

Jelena Dimitrijević, Dušan Arsenović and Branislav M. Jelenković

Institute of Physics, University of Belgrade,

Pregrevica 118, 11080 Belgrade, Serbia

email: jelenad@ipb.ac.rs

We analyze influence of the magnetic field on the 1D atom localization [1] in an atomic medium under the action of two optical fields, standing-wave and traveling-wave, probe field. Optical Bloch equations are solved numerically for the Zeeman sublevels of the hyperfine atomic transition $F_g=2 \rightarrow F_e=1$ of the ^{87}Rb D1 line. For small values of the applied magnetic field, electromagnetically induced transparency (EIT) [2] can be observed. Both fields are linearly polarized, with mutually orthogonal polarizations and wave-vectors. Two configurations are considered, depending whether applied magnetic field is in the direction of the standing-wave or the probe field polarization. Information on the atom position can be achieved both from the probe field absorption and the excited state population of the atomic system i.e. overall lasers fluorescence.

Two presented configurations enable different transitions between Zeeman magnetic sublevels, thus different formation of dark-states and localization patterns i.e. atom position probability distributions within wavelength distance. Depending on the laser fields' intensity magnitudes and on the applied magnetic field, presented localization schemes provide variety of results. We analyze width and contrast of the calculated localization narrow patterns for the range of laser field intensities, both being important parameters for the experimental realization of the localization effect. It is shown that, for the choice of parameters, magnetic field can bring substantial changes on the behavior of the position-dependent atom-field interaction, dark-state population, EIT and consequently localization effect. 2D localization effect via coherent magnetic field has been recently analyzed [3] by utilizing magnetic dipole allowed transition in a triangle atomic scheme.

REFERENCES

- [1] K. T. Kapale, in *Progress in Optics*, vol. 58, pp. 200, ed. E. Wolf, Elsevier (2013).
- [2] S. E. Harris, *Physics Today* **50** 36 (1997).
- [3] T. Shui, Z. Wang, B. Yu, *Quantum Inf. Process* **14**(3) 929 (2015).

On the conservation laws of Optical Bloch equations for Λ scheme

Jelena Dimitrijević, Dušan Arsenović, Branislav M. Jelenković

Institute of Physics Belgrade, Pregrevica 118 11080, Serbia

Contact: J. Dimitrijević (jelenad@ipb.ac.rs)

Abstract. We present results for the conservation laws, or quantities conserved in time, of the optical Bloch equations for the 3-level Λ scheme. Method of multipliers (variational derivative method) is used to construct non-trivial and functionally independent conservation laws which depend on the density-matrix elements. Results are classified by the different sets of phenomenological parameters characteristic for the optical Bloch equations - relaxation and decoherence terms, and the detunings of laser fields.

Results for the conservation laws obtained by the method of multipliers were used to construct another set of conservation laws. These conservation laws have explicit time-dependence and stand for the larger set of parameters - with relaxation via spontaneous emission or/and time-of-flight. Besides practical applications for the solutions methods, knowledge of the conservation laws for the optical Bloch equations could yield better understanding of the various processes they model.

Title of the publication

Nanoscale Quantum Optics

Kick-Off Workshop

ABTRACTS OF GUEST AND INVITED LECTURES AND CONTRIBUTED PAPERS

Editors

Jelena Dimitrijević, Branislav Jelenković and Mario Agio

Publisher

Institute of Physics, University of Belgrade, Pregrevica 118, 11080 Belgrade, Serbia

Printed by

COPY PLANET D.O.O.

Carice Milice 7, 11000 Belgrade, Serbia

Number of copies

20

ISBN 978-86-82441-42-7

CIP – Каталогизација у публикацији
Народна библиотека Србије, Београд

530.145:535.1(048)
66.017/.018(048)

NANOSCALE Quantum Optics Kick-off Workshop (2015 ; Beograd)
Abstracts of Guest and Invited Lectures and Contributed Papers /
Nanoscale Quantum Optics Kick-off Workshop, 9-10 April 2015
Belgrade, Serbia ; editors Jelena Dimitrijević, Branislav Jelenković
and Mario Agio.
- Belgrade : Institute of Physics, 2015 (Belgrade : Copy planet). -
XIV, 98 str. : ilustr. ; 25 cm

Tiraž 20. - Str. I: Preface / Mario Agio, Branislav Jelenković.

ISBN 978-86-82441-42-7

a) Квантна оптика – Апстракти b) Нанотехнологија – Апстракти
COBISS.SR-ID 214335756

Proposal for efficient atom localization scheme using Zeeman coherences in degenerate two-level atomic system

Jelena Dimitrijević, Dušan Arsenović and Branislav M. Jelenković

Institute of Physics, University of Belgrade, Pregrevica 118, 11080 Belgrade, Serbia

Contact: J. Dimitrijević (jelenad@ipb.ac.rs)

Abstract. Results are presented for the efficient atom localization scheme on the subwavelength range, by utilizing coherence phenomena - electromagnetically induced transparency (EIT) and absorption (EIA). We analyze configurations with cold atoms in the presence of two optical fields, standing-wave and probe field, both resonant with the hyperfine transition in Rb, and the applied external magnetic field. Numerical results are obtained by solving Optical Bloch equations for multilevel atomic schemes.

Method enables obtaining narrow atom excitation localization structures on the subwavelength range, with widths less than 0.5λ in the probe field absorption localization pattern. More, we analyze conditions where one can manipulate the position and contrast of the localization peaks by applying small magnetic fields. Behavior of the probe field absorption is analyzed through the mutual effects of two optical fields of various strengths, saturation effect and the EIT/EIA dependence on the applied magnetic field.